

Design and Evaluation of a Ship and Data Model for Digital Twin Applications

Auteur : p243634

Promoteur(s) : Rigo, Philippe

Faculté : Faculté des Sciences appliquées

Diplôme : Master : ingénieur civil mécanicien, à finalité spécialisée en "Advanced Ship Design"

Année académique : 2022-2023

URI/URL : <http://hdl.handle.net/2268.2/18139>

Avertissement à l'attention des usagers :

Tous les documents placés en accès ouvert sur le site le site MatheO sont protégés par le droit d'auteur. Conformément aux principes énoncés par la "Budapest Open Access Initiative"(BOAI, 2002), l'utilisateur du site peut lire, télécharger, copier, transmettre, imprimer, chercher ou faire un lien vers le texte intégral de ces documents, les disséquer pour les indexer, s'en servir de données pour un logiciel, ou s'en servir à toute autre fin légale (ou prévue par la réglementation relative au droit d'auteur). Toute utilisation du document à des fins commerciales est strictement interdite.

Par ailleurs, l'utilisateur s'engage à respecter les droits moraux de l'auteur, principalement le droit à l'intégrité de l'oeuvre et le droit de paternité et ce dans toute utilisation que l'utilisateur entreprend. Ainsi, à titre d'exemple, lorsqu'il reproduira un document par extrait ou dans son intégralité, l'utilisateur citera de manière complète les sources telles que mentionnées ci-dessus. Toute utilisation non explicitement autorisée ci-avant (telle que par exemple, la modification du document ou son résumé) nécessite l'autorisation préalable et expresse des auteurs ou de leurs ayants droit.



With the support of the
Erasmus+ Programme
of the European Union



Institute of
Maritime Energy Systems

Design and Evaluation of a Ship and Data Model for Digital Twin Applications

Master Thesis

Submitted on August 18, 2023

by Mahmoud Reda ELSHERIF

42523 Port Fuad, Port Said, Egypt

mahmoud.elsherif@uni-rostock.de

Student ID No.: 222202276

Reviewer

Dr.-Ing. Florian SPRENGER

florian.sprenger@uni-rostock.de

University of Rostock

Albert-Einstein-Str 2, 18059 Rostock,

Germany

Reviewer

M.Sc. Jan-Erik GIERING

jan-erik.giering@dlr.de

DLR - German Aerospace Centre

Max-Planck-Str 2, 21502 Geesthacht,

Germany

EMSHIP+ PROGRAM

ADVANCED DESIGN OF SHIPS AND OFFSHORE STRUCTURES

ACADEMIC YEAR 2022-2023

Design and Evaluation of a Ship and Data Model for Digital Twin Applications

© Mahmoud Elsherif, 2023

All rights reserved, text, pictures, and graphics are protected material.

The work in this thesis was carried out in:



Deutsches Zentrum für Luft- und Raumfahrt (DLR)
Institut für Maritime Energiesysteme
Geesthacht, Germany

Faculty Supervisor: Dr.-Ing. Florian Sprenger (University of Rostock, Germany)

M.Sc. Iven Sponholz (University of Rostock, Germany)

Direct Supervisor: M.Sc. Jan-Erik Giering (DLR, Germany)

Declaration of Authorship

I declare that this thesis and the work presented in it are my own and have been generated by me as the result of my own original research. Where I have consulted the published work of others, this is always clearly attributed. Where I have quoted from the work of others, the source is always given. With the exception of such quotations, this thesis is entirely my own work. I have acknowledged all main sources of help. Where the thesis is based on work done by myself jointly with others, I have made clear exactly what was done by others and what I have contributed myself. This thesis contains no material that has been submitted previously, in whole or in part, for the award of any other academic degree or diploma. I cede the copyright of the thesis in favor of the University of Rostock.

Geesthacht, August 19, 2023



Mahmoud Elsherif

This page intentionally left blank.

Acknowledgement

First and foremost, I would like to express my deepest gratitude to the Almighty god for bestowing upon me the guidance and strength to walk this challenging path and reach this significant milestone. Every challenge faced and every lesson learned was a testament to His boundless blessings and unwavering support.

To my dear wife, Sara, words fail to express the depth of my appreciation for your unyielding support, understanding, and encouragement throughout this journey. Your belief in my capabilities and your constant reminders of my potential propelled me forward during moments of doubt.

To my beloved children, Larien and Malika, you both have been rays of sunshine in my life. Your innocence, laughter, and unwavering faith in me have been my anchor. The drive to be better, to learn more, and to leave a legacy for you both motivated me through the toughest of times. This accomplishment is a testament to the joy and inspiration you bring into my life every single day.

I am profoundly thankful for the unwavering love and support of my family. This achievement is as much yours as it is mine.

This page intentionally left blank.

Abstract

The digital twin concept has emerged as a promising technology in various industries, including maritime applications. This thesis is focused on the design and evaluation of a ship and data model for a digital twin application. The primary thesis objective revolves around the detailed design of a functional remote-controlled ship model equipped with various sensors to gather real operational data which later will be utilized in creating a decision-support framework with a focus on hybrid energy systems. Following this, to effectively manage and analyze the generated data, the development of appropriate technology becomes imperative. In pursuit of this objective, a data modeling approach capable of proficiently storing, organizing, and retrieving data was proposed. Additionally, a data preprocessing algorithm was developed and tested on the collected data, aiming to enhance the data quality.

To achieve these objectives, an electro-mechanical system integrated with multiple sensors able to capture real operational data was designed for a scaled-down ship model. Although the use of a scaled model posed challenges in acquiring suitable components, it proved cost-effective, low-risk, and straightforward to design. The collected operational data effectively represented a single operation scenario, demonstrating the potential to expand to multiple scenarios for more extensive data analysis.

The research also emphasized that no one-size-fits-all data pre-processing technique exists, and finding the most suitable algorithms requires experimentation and comparative analysis. Various data pre-processing algorithms were explored, such as filtering outliers, noise reduction, data synchronization, and imputing missing data. These explorations aimed to elevate the quality of the data.

The outcomes of this research provide substantial insights into the utilization of scaled-down models to advance the development of digital twins, while also underscoring the various challenges associated with this implementation. This approach not only minimizes risks but also highlights the potential to establish a cost-effective testbed for decision-making support platforms. Additionally, the results underscore the significance of utilizing a variety of data pre-processing techniques to proficiently manage distinct data types and scenarios.

Ultimately, this study contributes to the advancement of digital twin applications in the maritime domain, opening new opportunities for harnessing the advantages of scaled-down models in creating and testing digital replicas. The data gathered from such models can significantly contribute to providing crucial decision support for ship operations with minimal risk compared to full-scale implementations.

Keywords: Digital twin, Data modeling, Data analysis, RC ship model

This page intentionally left blank.

Table of Content

List of Figures	v
List of Tables	ix
List of Abbreviations	xi
1 Introduction	1
1.1 Background	1
1.2 Problem statement	2
1.3 Research Objective	2
2 State of the art	3
3 Ship model characterization and evaluation	7
3.1 Main particulars	7
3.2 Manufacture of the hull	8
3.3 Weight and center of gravity	8
3.4 Resistance calculation	9
4 Requirement for the demonstrator	13
4.1 Control and communication system	13
4.2 Energy generation module	13
4.3 Parameters to measure	13
5 Component selection and sizing	17
5.1 Permanent component	17
5.2 Interchangeable component	25
5.3 Component interconnection	27
5.4 Miscellaneous component	31
5.5 Model assembly planning	31
5.6 Components weight list and price	35
6 Energy management system	37
7 Data model development	41
7.1 Data management system architecture	43
8 Data processing	45
8.1 Data Synchronising	46
8.2 Data compilation	48
8.3 Data cleaning	48
8.4 Missing data	56
8.5 Data down-sampling	59
8.6 Cross-verification of data	59
8.7 Data processing pipeline	60
9 Results	63
9.1 Final Equipping and Configuration of the Ship Model	63
9.2 Model static thrust or bollard pull test	65
9.3 Model self-propulsion test	83

10 Conclusion and Outlook	91
Bibliography	95
A Inclining test procedure	105
B Model empirical resistance calculation	113
C Towing test	117
D Propulsion Motor Calculations	123
E Model Photos	125

List of Figures

3.1	Actual model dimensions, in mm	8
3.2	Empirical and experimental speed - resistance graphs for the ship model	11
4.1	Internal parameters for evaluating the powering system performance	14
5.1	Ship model rudder dimensions , in mm	20
5.2	Simplified brushless motor diagram (Tang, 2021)	21
5.3	A correlation matrix of components illustrates the interconnection among individual components as well as the measuring parameters	29
5.4	Overall diagrammatic representation of the onboard components	30
5.5	3D-Printed parts (Dimension in mm)	31
5.6	Arrangement of components in a two-dimensional layout, with dimensions specified in millimeters.	32
5.7	Arrangement of components in a two-dimensional layout	32
5.8	Arrangement of components in 3D perspective views	33
5.9	Proposed design of the interchangeable plate intended to enclose the EGM components, with dimension specific in millimeters	34
5.10	A 3D illustration of interchangeability feature for the EGM components	34
6.1	The diagrammatic representation of energy generation module based on a combustion engine	37
6.2	The proposed energy management system flow chart	39
7.1	Overall data models ERM proposed diagram	42
7.2	The proposed data management system architecture	44
8.1	Demonstration of Dynamic Time Warping (DTW) cost matrix initialization (on left) and graphical representation of warping path (on right)	47
8.2	Summarized Kalman filter principle and formation (Becker, 2023)	50
8.3	Box plot example graph illustrating different component of the plot (Azevedo, 2022)	52
8.4	Exemplary comparison between the outliers visualization methods (scatter plot, box plot, and kernel density plot)	53
8.5	Chauvenet’s criterion graphical representation	55
8.6	Comparison between listwise and pairwise deletion methods	57
8.7	Graphical representation of the proposed data pre-processing pipeline	61
9.1	Simplified diagram for the onboard components in the final model state	64
9.2	Additional solid weights layout for maintaining models draft of 9.0 cm during the model trials, with dimensions specified in millimeters	64
9.3	Time series graph for the parameters involved in the static thrust test (thrust force, battery drawn energy, battery power, and throttle percentage)	66

9.4	DTW data points aligning visualization	67
9.5	A graphical representation of the throttle and thrust force signals before and after synchronizing using DTW algorithm	68
9.6	A graphical representation of the synchronizing process results with different signal downsampling rates for the thrust force signal	70
9.7	A comparison between the unsynchronized and synchronized result using cross-correlation method	71
9.8	Comparison of the correlation matrices among the parameters (throttle, battery power, and thrust force) using three different correlation methods (Pearson, Spearman’s rank, and Distance correlation) before and after synchronization, employing a heat map visualization technique	72
9.9	A comparison of thrust and power signals within a time window before and after the implementation of the Kalman filter.	73
9.10	Thrust and power signal comparison before and after applying the low-pass filter	74
9.11	Univariate (box plots) versus multivariate (scatter plot) outlier visualization for both battery power and thrust signal recorded during the static thrust test	77
9.12	A graphical representation of the results of univariate outliers detection methods applied on battery power signal with different time series block sizes	78
9.13	A comparison between the dataset before and after outliers removal and data imputation method using modified Z-score and kNN respectively with 20 blocks	80
9.14	Comparison of the correlation matrices among the parameters (throttle, battery power, and thrust force) using three different correlation methods (Pearson, Spearman’s rank, and Distance correlation) before and after outliers removal and imputation using modified Z score, kNN with 20 equal time series blocks, employing a heat map visualization technique	81
9.15	Second order curve fitting representing the correlation between the thrust force and battery power at zero speed condition	82
9.16	Overall insight into the three parameters of interest for the speed runs	84
9.17	A heatmap depicting the correlation coefficients among the parameters (throttle, battery power, and model speed) using three distinct correlation methods (Pearson, Spearman’s rank, and Distance correlation) during the speed test	84
9.18	Speed and power signal comparison before and after applying the low-pass filter	85
9.19	Univariate (box plots) versus multivariate (scatter plot) outlier visualization for both model speed and battery power signals recorded during the model self-propulsion test	86
9.20	Speed and battery power parameters plotted against the throttle value	87
9.21	Univariate (box plots) versus multivariate (scatter plot) outlier visualization for both model speed and battery power signals recorded during the model self-propulsion test after averaging	88
9.22	Speed and battery power parameters linear regression in log-log space	89
A.1	Ship inclined by weight	105
A.2	Solid weights layout during the inclining experiment	107
A.3	Weight shift 0 to 2nd	108
A.4	Weight shift 3rd to 5th	108
A.5	Weight shift 6th to 8th	109

B.1	Ship model speed - total resistance graph according to empirical calculations	114
C.1	Measured resistance 5 seconds before clamp closure	118
C.2	Recorded data at speed 0.63ms	119
C.3	Ship model speed - total resistance graph according to towing test	120
C.4	Weights arrangement in the model	121
C.5	Prepared Model	122
C.6	The model attached to the towing cartage	122
E.1	Model hull	125
E.2	Model internal components	126
E.3	Prepared Model	127
E.4	Model during the bollard pull test	128
E.5	Prepared model for runs	129

This page intentionally left blank.

List of Tables

3.1	Reference ship / Model ship parameters	7
3.2	Bare hull weight and COG	8
3.3	Reference and model ship empirical resistance values at maximum speed	10
4.1	Parameter of interest for each component	15
5.1	Rudder force and torque calculation	19
5.2	Rudder servo specifications	19
5.3	Electric motor required parameters	21
5.4	The proposed electrical motor specification	21
5.5	Alternative employed electric motor specifications.	22
5.6	Battery sizing calculation summary	23
5.7	The chosen battery specification	24
5.8	The proposed dynamo parameters	26
5.9	The proposed combustion engine parameters	26
5.10	The proposed fuel pump specification	27
5.11	List of major components	33
5.12	List of major component weight and cost	36
9.1	The list of the final components installed in the model	63
9.2	Model final weight and COG	64
9.3	Static thrust test captured parameters with their attributes	65
9.4	Correlation coefficients between throttle and thrust force signals before and after synchronizing using dynamic time warping method using (Pearson, Spearman's rank and Distance correlation)	69
9.5	DTW results comparison before and after data downsampling (from 50 Hz to 10 Hz)	69
9.6	Correlation coefficients (Pearson, Spearman's rank, and Distance correlation) between the throttle and thrust force signals before and after synchronization using the cross-correlation method.	70
9.7	Synchronizing methods computational efforts comparison	72
9.8	Signal-to-noise values for different signal-denoising approaches	75
9.9	Comparison between different correlation coefficients between the denoised signals and the throttle reference signal	76
9.10	Univariate outlier detection methods results applied on battery power and thrust force signals	77
9.11	Speed test captured parameters	83
9.12	Signal-to-noise values for speed and power signals before and after denoising using LPF	85
A.1	Inclining test General information	106

- A.2 Weight breakdown during the inclining experiment 107
- A.3 Measured drafts 109
- A.4 Inclining experiment weight shifts and angle reading 110
- A.5 Hydrostatics parameters for actual and 3D model 111
- A.6 Model weight and COG as inclined 111
- A.7 Bare hull weight and COG 112

- B.1 Model total resistance calculation 115

- C.1 Towing test model weight breakdown 117
- C.2 The recorded model total resistance 120

- D.1 Powering calculation parameters 124

List of Abbreviations

Abbreviation	Meaning
AC	Alternating Current
BLDC	Brushless DC electric Motor
CE	Combustion Engine
COG	Center of Gravity
DC	Direct Current
DLR	Deutsches Zentrum für Luft- und Raumfahrt
DT	Digital Twin
DTW	Dynamic Time Warping
EGM	Energy Generating Module
EMS	Energy Management System
ERM	Entity-Relationship Model
ESC	Electronic Speed Controller
FFT	Fast Fourier transform
GPIO	General Purpose Input/Output
HSVA	Hamburgische Schiffbau-Versuchsanstalt
IMO	International Maritime Organization
IMU	Inertia Measurement Unit
IQR	Interquartile Range
GFRP	Glass Fiber Reinforced Plastic
LPF	Low-pass filter
MDF	Medium-density fibreboard
ML	Machine Learning
PCB	Printed Circuit Board
PDB	Power Distribution Board
PWM	Pulse Width Modulation
RC	Remort Control
SFC	Specific Fuel Consumption
SNR	Signal-to-noise ratio
SMA	Simple Moving Average

Abbreviation	Meaning
SOC	State of Charge
SWS	Sliding Window Size
SQL DDL	Structured Query Language Data Definition Language
TUHH	Technische Universität Hamburg
UAV	Unmanned Aerial Vehicle

1

Introduction

1.1 Background

The maritime industry had a steady increase in world trade share over the last century. Serving around 90% of global trade, the maritime industry remains the backbone of international trade (Hasanspahić et al., 2020). Marine transportation plays a crucial role in the global economy, facilitating the movement of goods valued in billions of dollars on a daily basis. In 2015, the estimated volume of seaborne trade exceeded 10 billion tons. However, it is important to recognize that the enormous volume of global marine transportation also brings negative environmental impacts on the marine ecosystem (Walker et al., 2019).

Global tendencies and political pressures for decarbonization have also affected the maritime industry. International Maritime Organization (IMO) regulations are becoming stricter to reduce ship emissions by the year 2100 (Jabary et al., 2023a). These regulations have driven the industry to find more environmentally friendly power systems (Inal et al., 2022). It also pushed the industry to harness new innovative technologies such as Digital Twin (DT) to fulfil the decarbonization demand (Wei et al., 2023).

Currently, we are witnessing the new Industry 4.0 revolution, where the DT technology is the cornerstone of it (Pang et al., 2021). This is reflected in the global ubiquitous trend toward digitization, and DT implementation in various domains such as manufacturing (Negri et al., 2017), aerospace (Ríos et al., 2015), production science (Kritzinger et al., 2018), production systems (Guerra-Zubiaga et al., 2021), and other general domains. This trend has long reached the maritime industry as well (Giering and Dyck, 2021).

In the recent past, DT technology has emerged as a transformative force in various industries. By creating a virtual replicate of physical ships or ships systems, DT provide a comprehensive and real-time understanding of ship performance, providing more capability for efficient and effective decision-making through the ship's life-cycle (Chen et al., 2021).

These DT applications have the potential to benefit shipbuilders, naval architects, ship operators, maintenance service providers, regulatory bodies, classification societies, researchers, and innovators. Thanks to the ongoing development and DT implementation in the maritime sector (Mauro and Kana, 2023). These stakeholders gained many advantages such as design improvement, optimized operation, and enhanced operational efficiency (Chen et al., 2021).

Furthermore, Hybrid vessels that is being powered by various types of energy sources are considered reliable power sources for different ship operation conditions. Having multi-energy sources onboard will compensate for the disadvantage of having a single power supply (Yuan et al., 2020). This will significantly increase the complexity level of the onboard powering system. With this increasing complexity, an appropriate energy management system is required to safely and efficiently leverage these multi-energy sources onboard (Yuan et al.,

2020; Inal et al., 2022). This is a result of the increase in the number of parameters that need to be controlled and monitored for each power source as well as the need to have a good balance between them for each operation mode.

1.2 Problem statement

With these convoluted processes concerning hybrid vessels' energy management, several strategies developed and are presently in practice. However, (Yuan et al., 2020) highlighted the current energy management strategies are mainly to ensure the expected response of the hybrid power system. He further appended that this is not enough since other requirements should be taken into consideration such as ship operating conditions, engine emissions requirements, the life of the energy storage system, reliability, cost of components, and ship safety.

Considering these factors alongside the inherent complexity of the hybrid system, the integration of these elements will generate a substantial volume of input data representing various parameters. Efficient analysis of this extensive data is essential to derive a meaningful evaluation of such an intricate system. For this, the application of DT is considered a potential solution since it can provide real-time monitoring for crucial parameters and eventually accurate evaluation for the whole system.

The research institute of Maritime Energy Systems, as part of the German Aerospace Center (Deutsches Zentrum für Luft- und Raumfahrt (DLR)) adopted the initiative to provide the stakeholders with innovative solutions to monitor and evaluate complex hybrid energy systems based on alternative fuel based on modern DT application. DLR aims also to provide a foundation for an open source software that can utilize the captured data and provide decision-making support that can help to monitor and evaluate the performance of modern hybrid energy systems that might be used onboard.

Given the challenges discussed regarding the formulation of an energy management system for a complex hybrid powering system that includes various requirements, it is also essential to consider the hazardous nature of certain alternative fuels (Yuan et al., 2020). Additionally, the high cost associated with such systems further adds to the complexity. Consequently, developing a virtual replica (Digital Twin) of such a complex hybrid energy system that can reliably provide decision-making support services to stakeholders is a highly challenging task, especially for a full-scale vessel in operation.

1.3 Research Objective

- The first objective of this thesis is to provide and implement a system design for a scaled-down ship model driven by a simple interchangeable hybrid system equipped with various sensors that provide meaningful operational real data to be utilized in future work to develop open-source software that provides services such as decision-support for hybrid energy systems.
- The second objective of this thesis is to develop a coherent data model that offers a structured representation of operating characteristics and the relationships between various information objects. Additionally, To develop a data management system for efficient processing and analysis of different sensors' captured data.

2

State of the art

Gelernter (1993) provided an early anticipation of the DT concept in his book *Mirror Worlds*. He represented the concept of *Mirror Worlds* as a virtual world that mirrors the physical world, in which data from the physical world is continuously updated in real-time to provide a more comprehensive and detailed view of reality. In this virtual world, users can interact with digital representations of physical objects, places, and events, and explore and analyze data in new ways.

In the early 2000s, Michael Grieves introduced the concept of the DT in a University of Michigan presentation to the industry with a focus on Product Life-cycle Management (PLM) (Liu et al., 2021). He defined the three main elements of the DT: real space, virtual space, and the link for data flow between both spaces.

In this era, the DT concept was missing the supportive auxiliary informative technologies for its complete implementation (Liu et al., 2021). However, almost a decade after (in 2012), the concept was extended to the manufacturing industry derived by technological advancement in fields such as cloud computing, the Internet of Things (IoT), and big data. Hence, the DT became the primary derivation of the revolutionary development in the Industry 4.0 era (Sharma et al., 2022).

Throughout all of these development stages and implementation, the definition of the DT has been evolving also. The most modern definition of the DT is mentioned by Mauro and Kana (2023) as follows:

“The DT is a virtual representation of a physical entity or process, potentially during its entire life-cycle. The virtual entity is capable of representing the actual status of the physical entity including a relevant recording of historically collected data. Additionally, the DT can evaluate the future behavior of the physical entity, modifying some control actions up to optimizing a complete operation”

Coraddu et al. (2019) introduced The first ship operation decision support with a focus on condition monitoring and calibrating numerical simulations with respect to real operational data where a data-driven DT was used to estimate the speed loss caused by marine fouling. Also in 2019, the DT is used to estimate the cumulative damage that the ship would encounter Schirmann et al. (2018) by utilizing the DT to monitor the ship’s motion and potential structure fatigue due to wave response.

Mauro and Kana (2023) published a review paper focusing on digital twins for the ship life cycle and mentioned that the number of publications per year that include "digital twin" in title or keywords between 2012 to August 2023 increased from 7 to 2083 publications according

to the Scopus database. In 2022, 40 publications were focused on DT in the maritime field. The research also discussed the DT collocation across the ship life cycle which is divided into four main phases (Design, Production, Operation, and Retire), one of their findings is 38 out of 58 studied publications are concerning about the operation phase with an expectation for this number to grow constantly due to the main focus of the shipping industry in this area specifically on power systems performance prediction.

These applications primarily remain confined to particular use cases. Therefore, there is still a lack of generalized conceptualizations or definitions that enable broader interoperability across different contexts Låg and Brathagen (2017).

A comprehensive Maritime Digital Twin Architecture concept, capable of offering complete life cycle support for ships, was introduced by (Giering and Dyck, 2021). The proposed concept aims to encompass all phases of a ship's life cycle, starting with conceptual design until decommissioning.

Moreover, utilizing the ship-scaled models in naval architecture has proven applications. The first implementation of the ship-scaled model to predict the ship's total resistance was by (Froude, 1872). Model ships have also been employed to study the behavior of full-scale ships in other domains such as maneuvering (Skjetne et al., 2005), dynamic positioning (Alfheim et al., 2018), and sea keeping (Maury et al., 2003).

Working on a scaled-down model offers various advantages such as cost-effectiveness, lower risk, a more controlled environment and conditions, as well as a significantly smaller amount of data to be analyzed and a simpler system to handle. However, utilizing a scaled-down ship model as a physical asset in the context of the digital twin is still in its infancy, and there are very few cases that can be used as references.

By combining both aspects of using a scaled-down ship model and DT, Fonseca and Gaspar (2020) applied the fundamental of a DT on a plastic floating toy, the physical experiment consisted of a small aquarium and a plastic floating toy. The toy movement (surge, heave, and pitch) was captured by a webcam then the captured video will be streamed to a client. The client could then execute digital twin simulations in real-time using a web browser. The system was coupled with automated reasoning based on the tracked parameters, enabling the digital twin to emit a warning if the toy motion crosses the user-defined threshold. They also used this as a simple example to present the elements of DT concepts and how they interact with each other.

Fonseca and Gaspar (2020) introduced a more complex case in the same paper, another digital twin aims to monitor and control a ship scale model which navigates in a wave basin. The ship model was equipped with dynamic positioning (DP) system consisting of two azimuth propellers and a bow thruster. The digital twin visualization mirrored the scale model behavior and monitored its motion response in 6-DOF. Additionally, the propulsion system operation and waves incident were also monitored.

Zhang et al. (2022) presented the importance of data in the context of DT. He emphasized how data is playing a vital role in the creation of digital assets, establishing digital-physical connections, and enabling intelligent operations. He also added that the success of DT pri-

marily hinges on the accessibility and availability of high-quality data sources. The reliability and richness of the data influence the accuracy and effectiveness of the Digital Twin, making data acquisition and management crucial aspects in achieving desired outcomes. Assani et al. (2022) highlighted the potential challenges in data analysis since the gathered data is required to undergo pre-processes such as filtering outliers, filtering noise, interpolation, and synchronizing. To efficiently achieve such a task Rathore et al. (2021) pointed out the positive influence of integrating big data analytics and artificial intelligence/machine learning (AI-ML) techniques into the DT. This will enhance the DT potentials and help to maximize its benefits. These fields were the main reason for evolving the DT applications in the first place.

For DT application on ships, several methods are available for pre-processing the raw data. ISO19030 (2016) has introduced guidelines for data acquisition, compilation, filtering, and validation with the main focus on evaluating the hull and propeller performance.

The first objective of the presented thesis will be based on merging the classical concept of utilizing a scaled-down ship model with the concept of DT with a main focus on studying maritime hybrid energy systems. This will require providing a specialized design tailored to this application. Unlike the standard models that are usually used in ship model tests, this model is essentially a fully operational scaled-down vessel with self-propulsion and maneuvering capabilities. The model also features a high degree of controllability with the potential for autonomous functionality. The model is powered by a hybrid interchangeable power module, enabling it to operate under various power configurations. Additionally, an array of sensors is integrated throughout the model system to acquire operational metrics.

Subsequently, it was necessary to conceptualize a solution that can handle the data harvested by these sensors. For this purpose, an architecture for the data management system was proposed. This system can be utilized to efficiently organize, store and retrieve the data. Moreover, a data pre-processing system was developed to increase the quality of the harvested data by mitigating its inherent potential flaws such as signal lag, noise, data outliers, and missing data points.

This will provide access to a simplified use case of a scaled-down ship hybrid system that will be employed to implement, evaluate and improve the first prototype of DT software intended by DLR. Additionally, to provide a testbed for potential future services that can leverage the DT.

After the software is tested and proven to provide reliable satisfactory outcomes, it will be utilized for a full-scale vessel and be available for the stakeholders.

This page intentionally left blank.

3

Ship model characterization and evaluation

Characterizing the provided model was essential in order to obtain all the relevant information required for sizing the propulsion system and the onboard powering system. Furthermore, this characterization process serves as a valuable source of reference data for the DT application.

3.1 Main particulars

The model employed for digital twin demonstration is a scaled-down model derived from a reference ship Ludwig Prandtl II (LPII). LPII is a twin-screw vessel where each propeller is powered by one main diesel engine with 360 kW power. Each propeller has a diameter of 1.1 m and has five blades. This research vessel is currently in the design stage.

The preliminary design of the scaled model was conceptualized in a thesis published by the University of Duisburg-Essen (Husemann, 2022). The model was scaled down from the reference ship based on Froude Number (F_n) similarity rule. In the mentioned thesis, one of the focal points is the selection of the proper value of the scaling factor (λ) which achieves a good compromise between power demand and the resulting hull weight since both parameters are highly affected by the model length which must not exceed 2 meters. The value chosen for the scaling factor (λ) was 16.61. Then, the theoretical model dimensions are driven from the reference ship. Table 3.1 shows a comparative overview of the main particulars of both the reference and the model ship.

Table 3.1: Reference ship / Model ship parameters

Parameter	Symbol	Reference ship Value	Ship Model Value	Unit
Length overall	LOA	29.9	1.8	m
Length waterline	LWL	29.9	1.8	m
Length between perpendiculars	LBP	29.2	1.76	m
Breadth	B	8	0.48	m
Design draft	T	1.5	0.09	m
Volume of displacement	∇	230.7	0.0503	m^3
Displacement	Δ	236.5	0.0516	t
Block coefficient	C_B		0.639	--
Speed	v	12	2.94	kn
Froude Number	F_n		0.36	--

In contrast to the theoretically estimated dimensions given in the table above, the dimensions of the physical model are slightly different due to some manufacturing deviations. This is an indication of potential discrepancies between the characterizations of the actual and theoretical models. The dimension of the actual model is represented in Figure 3.1. Additionally, the figure also shows the principal axis orientation that will be used for any afterward distance measuring.

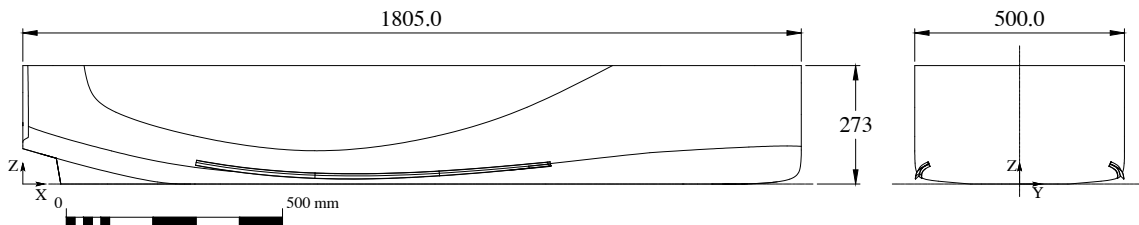


Figure 3.1: Actual model dimensions, in mm

3.2 Manufacture of the hull

The model hull was fabricated of 2 mm thickness Glass Fiber Reinforced Plastic (GFRP). Using the GFRP material gave the model bare hull a lightweight advantage allowing for an adequate margin of weight for internal components needed to fulfil the demonstrator mission. Moreover, working with GFRP facilitated operations such as drilling and adhesive bonding of other components into the hull.

3.3 Weight and center of gravity

It was necessary to measure the model bare hull weight and identify the three-dimensional location of the center of gravity. This will help to have an appropriate distribution of internal components throughout the hull. Additionally, it will help to precisely determine the location of necessary additional weights to minimize the model trim and maintain the desired draft.

The bare hull weight was directly measured using a digital scale, while the location of the center of gravity was determined by conducting an inclining experiment. Table 3.2 shows the experiment results. The detailed inclining procedure is mentioned in Appendix A.

Having the bare hull Center of Gravity (COG) will also facilitate predicting the model behavior by simulating potential loading conditions using any available naval architecture software package (e.g., MAXSURF).

Table 3.2: Bare hull weight and COG

Parameter	Value	unit
Lightweight	10.68	kg
Longitudinal center of gravity (LCG)	81.8	Centimeters from AFT
Transverse center of gravity (TCG)	0.00	Centimeters from CL
Vertical center of gravity (VCG/KG)	6.02	Centimeters from Baseline

3.4 Resistance calculation

To precisely determine the size of the propulsion system component, it is necessary to calculate the power needed to propel the model up to a certain speed which requires calculating the model's total resistance through the water with range of operational speeds

Resistance calculations have been done first empirically and then experimentally by conducting a towing test. In both cases, the model resistance was calculated for model speed up to 2.94 *knots* (1.51 *m/s*) at a draft value of 9 *cm* which are corresponding to 12 *knots* speed and a 1.5 m draft of the reference ship.

3.4.1 Empirical Method (Holtrop and Mennen)

The proposed approach involves using a proven empirical method to predict the total resistance (R_{TS}) of the reference ship, which is subsequently decomposed into ship residual resistance (R_{RS}) and ship friction resistance (R_{FS}). The reference ship residual resistance is then scaled down to the model level to get model residual resistance (R_{RM}) (Using the scale factor (λ^3)) while the model friction resistance (R_{FM}) is calculated separately. Then, the model total resistance (R_{TM}) is simply the summation of both model friction and residual resistance.

This approach is similar to the method employed in scaling up the model's total resistance to the reference ship, albeit in a reverse way. These calculations are governed by Equation (3.1) (Carlton, 2007).

$$R_{TS} = [R_{TM} - R_{FM}(1 + k)] \lambda^3 \left(\frac{\rho_S}{\rho_M} \right) + R_{FS}(1 + k) \quad (3.1)$$

(Holtrop and Mennen, 1982) method was found to be the nearest suitable method that can be utilized since the ship particulars and form coefficients are near to the range of application on this method. This method is also available in MAXSURF software package (Resistance Module) which facilitates its employment on the provided 3D model of LP11. The model total resistance is then calculated following the following procedure:

1. Calculate the total resistance for the mother ship (R_{TS}) using Holtrop & Mennen method.
2. Calculate the friction resistance of the mother ship (R_{FS}).
3. Calculate the residual resistance of the mother ship ($R_{WS} = R_{TS} - R_{FS}$).
4. Calculate the model residual resistance ($R_{WM} = R_{WS}/\lambda^3$).
5. Calculate the model friction resistance (R_{FM}).
6. Calculate the model total resistance ($R_{TM} = R_{WM} + R_{FM}$).

As a result of applying the previously described approach, the reference ship and the model resistance values at maximum speed and design draft are shown in Table 3.3. The detailed calculations and results table are shown in Appendix B.

Table 3.3: Reference and model ship empirical resistance values at maximum speed

Parameter	Symbol	Reference ship value	Model ship value	Unit
Speed	v	12	2.94	kn
Total Resistance	R_{TS} / R_{TM}	32025.02	9.20	N
Friction Resistance	R_{FS} / R_{FM}	11219.73	4.13	N
Residual Resistance	R_{WS} / R_{WM}	20805.29	4.54	N

It is worth mentioning that the purpose of using an empirical equation for resistance calculation was to gain a preliminary understanding of the power range required for the model prior to conducting the towing test. This allows for an early insight into the available commercial solutions that can fulfill the mission before executing the towing tank test.

3.4.2 Experimental Method (Towing test)

The previous method provided a first glance at the potential power demand to propel the model. However, towing test was conducted to provide more solid results for the model resistance at the same range of speeds. These values will be used later as reference data while evaluating the propulsion system performance. The towing test was done by Technische Universität Hamburg (TUHH) in Hamburgische Schiffbau-Versuchsanstalt (HSVA). The recorded total resistance at the model speed of 1.51 m/s is 10.29 N which is corresponding to a speed of 12 knots for the reference ship.

A dynamic draft (parallel sinkage) was also observed during the model test, the recorded values were 12 and 16 mm corresponding to speeds of 1.51 and 1.63 m/s respectively. The detailed towing test procedure is described in detail in [Appendix C](#).

3.4.3 Resistance results comparison

The summary results of both approaches are shown in [Figure 3.2](#). A good correlation can be observed between both empirical and experimental results. However, at a certain point, the experimental results showed higher values. For instance, the model maximum speed of 1.51 m/s , the experimental resistance value was 10.29 N which is almost 12% higher than the empirical one (9.2 N). The rationale for this lies in the following factors:

- The chosen empirical equation was the nearest match but not a perfect match to research the vessel type. As Holtrop & Mennen was basically developed for vessels with L/B ratio between 3.9 to 9.5 and a B/T ratio between 2.1 to 4 ([Hasan, 2014](#)). The current vessel has an L/B ratio of 3.73 and a B/T ratio of 5.3.
- The empirical equations used to drive the model resistance was applied on the provided 3D model of LPII and the actual model showed some deviations with respect to the scaled-down model size of LPII.
- The experimental methods are more reliable since they capture the actual underwater shape including any potential manufacturing deviation. While the regression analysis-based empirical methods can not handle uncommon vessel types and hull forms ([Bekhit and Obreja, 2020](#)).

- Another reason is the presence of two mistakenly oversized bilge keels that are not existing in the reference ship which surely has impacted the model's resistance.

Nevertheless, this deviation in the resistance value does not pose any challenge since the difference can be easily covered with the chosen propulsion motors.

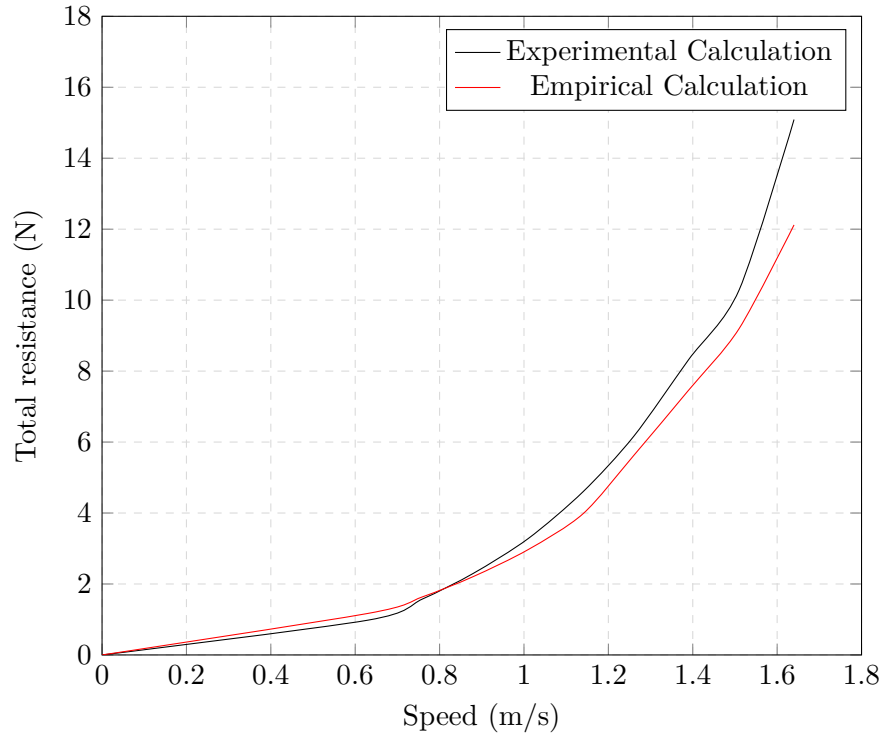


Figure 3.2: Empirical and experimental speed - resistance graphs for the ship model

This page intentionally left blank.

4

Requirement for the demonstrator

In this chapter, the desired requirements for the model are discussed, including the control system, powering requirement, and the required parameters for measurement during the operation.

4.1 Control and communication system

The model is required to be remotely controlled by an onshore control station through distance. Additionally, all measured parameters are required to be stored onboard the model with the capability to be transmitted to an onshore receiver for further analysis.

4.2 Energy generation module

The model is planned to be powered by one of two proposed different interchangeable Energy Generating Module (EGM). The proposed EGMs is either powered by a Combustion Engine (CE) or a fuel cell. Due to the time constraint of the thesis, the main focus will be on the EGM based on the CE. This EGM consists of a CE driving a dynamo that will, in turn, convert the rotation mechanical energy to electrical energy. This electrical energy will be distributed to power all internal model components and charge the buffer battery. The EGM should be designed in a way that facilitates any potential future developments or changes to the other proposed EGM when required.

4.3 Parameters to measure

The goal of this project is to use the generated data to create reliable decision-support software for complex hybrid energy systems. Bal Beşikçi et al. (2016) specified the crucial parameters needed to build a decision-support system for energy-efficient ship operation. These parameters are ship speed, RPM, mean draft, trim, cargo quantity, wind effect, and Sea condition. In a ship model scale, with a controlled environment, these parameters are shortened into ship speed, RPM, mean draft, and trim only. However, since the intended energy system for the model is a hybrid system, these parameters are extended to also include other parameters related to the hybrid power train individual components. This will facilitate the comprehensive capture of the overall system's performance.

As discussed before, the propulsion system train has three energy conversion processes. these processes are from chemical to mechanical energy in the CE, from mechanical to electrical energy through the dynamo, and from electrical energy back to mechanical energy

through the electrical motor. This will not only lead to energy losses but also it will increase the number of parameters to measure to efficiently compute the overall system efficiency. This will also lead to an increase in the number of equipped sensors.

Consequently, for the purpose of organization, the parameters of interest have been categorized into two main groups: internal parameters and external parameters.

4.3.1 Internal parameters

The internal parameters are those parameters that are directly tied to the input and output measurement of the power train's individual components. These parameters are directly utilized to measure each component's efficiency and eventually to assess the entire system's efficiency. These parameters, along with their interrelationships, their correlations to one another, and their associated components, are illustrated in Figure 4.1.

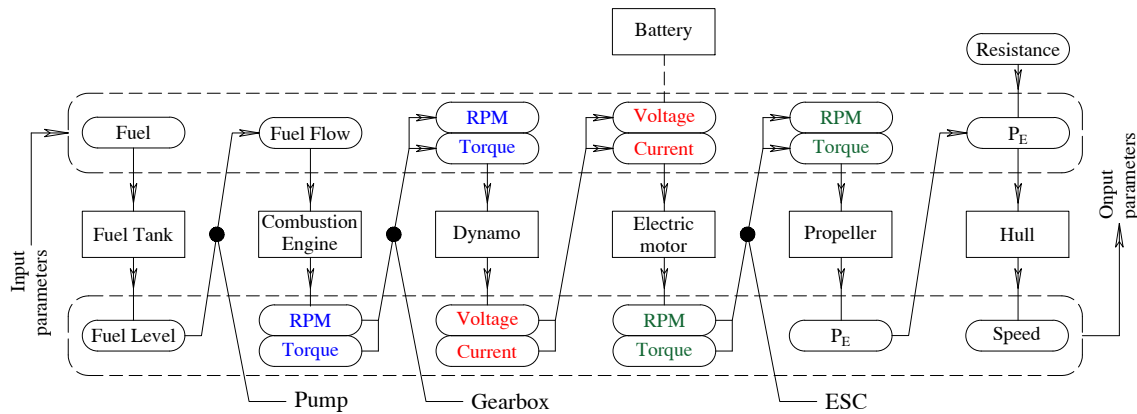


Figure 4.1: Internal parameters for evaluating the powering system performance

Starting from the fuel tank, measuring the tank fill percentage is needed since it can be compared afterward with the accumulated fuel flow sensor readings. Tracking these readings from two different sources will provide a quick evaluation of both sensors' efficiency. Moreover, it will also give a pre-alarm when the tank reaches a low level.

The fuel flow sensor also serves to measure the fuel input to the CE, these readings will be used (together with the fuel energy content) to calculate the engine input power.

Multiple torque sensors that measure both torque and RPM are necessary to derive the engine's, dynamo's, and electrical motors' output power.

Concerning the backup energy system, it is essential to monitor and record several parameters. These parameters are battery State of charge (SOC) which helps to ensure that sufficient energy is available if needed and determine the start/end of the onboard charging process. The voltage, drawn current, and eventually output power are playing a similar role to the dynamo output power in determining the input power to the motors. These parameters collectively are to be utilized to monitor and evaluate the efficiency of the backup system.

As observed from the parameters described earlier, a consistent pattern exists in their selection. This pattern revolves around capturing the input and output power of individual power train components. This approach is essential to derive the efficiency of each component

separately and ultimately the whole power train efficiency.

The last component of the illustrated power train is the model speed. The speed parameters nature is quite different from other parameters that are mainly power components. However, hull speed together with the ship resistance corresponding to that speed is representing the effective power needed to drive the model. The power needed to propel the ship at a certain speed is always representing the biggest share of the total power demand (almost 62% in the current case). On top of that, the temperature has a huge impact on the EGM efficiency and performance. For that reason, multiple heat sensors are to be fitted to monitor equipment temperature during operation, except only for some equipment that can inherently have its own built-in temperature monitor system.

4.3.2 External parameters

As explained before, the biggest share of power demand is reserved by propulsion power which in turn is highly influenced by the model resistance through water. The external parameters are those that have a direct influence on hull resistance. These parameters are ship hydrostatics and water temperature. Therefore, these parameters are required to be captured during the operation. Especially when comparing different loading conditions in different environments.

The rudder angle is also a crucial parameter to measure. During the model tests, the model will be required to perform some necessary maneuverings. In evaluating the system's performance, it would be necessary to differentiate between free-running and maneuvering cases. This is because of the obvious difference in the hydrodynamics of the model in both cases. The summarized list of these parameters is shown in Table 4.1.

Table 4.1: Parameter of interest for each component

Component	Parameters of interest
Hull	Position relative to a reference point to be defined in 2D plane
	Speed, Acceleration, DOF
	Mean draft, Trim
CE	Throttle servo signal
	RPM/Torque
	Fuel consumption (Fuel flow rate)
Dynamo	Operation duration
	RPM
	Electrical Energy output (Voltage/Current)
Battery	SOC
	Start/End of onboard charging operation
	Energy output (Voltage/Current/Power)
Electrical	RPM / Torque
Propulsion motors	Energy Consumption (Voltage/Current)
Fuel Tank	Percentage filled
Rudders	Rudder angle

This page intentionally left blank.

5

Component selection and sizing

The model is planned to be powered by one of two different EGM. Therefore the components are categorized into two main groups. The permanent component group contains components that are independent of EGM change. The interchangeable component group consists of the EGM components with their auxiliary attachments. This will facilitate the EGM exchanging process since the interchangeable components will be encapsulated together. In the following sections, these components will be described in more detail.

5.1 Permanent component

The components that are not influenced by changing the EGM either the CE or the fuel cell are described under this section.

5.1.1 Control component

The model was intended to be remote-controlled through a distance where the operator would fully control all model functions while sailing through the water. This can be achieved by using a remote control transmitter that is wirelessly connected via a radio signal to a receiver. The latter is placed in the model.

The ground remote control chosen is Taranis x20s (MHM-Modellbau.de, a) which has an operation range of up to 100km with only 4 ms of latency. It provides a decent display screen that can be utilized to monitor parameters during operation. It also offers up to 24 channels that can be utilized to execute different commands to the model.

On the contrary part, A receiver is to be fitted in the model that will telemetry the Remote control (RC) operator commands from the controller to the rest of the model. The selected receiver is FrSky Archer (MHM-Modellbau.de, b) which is compatible to the previously selected controller.

5.1.2 Autopilot

Within this subsection, a brief description is provided for both the autopilot software and hardware components.

5.1.2.1 Autopilot Software

The software utilized for the current application is called ArduPilot. ArduPilot is a versatile and trusted open-source autopilot system that supports various vehicle types, including

multi-copters, helicopters, fixed-wing aircraft, boats, submarines, and rovers. ArduPilot applications are extended to the creation of reliable and autonomous unmanned vehicle systems for peaceful purposes, offering a comprehensive suite of tools suitable for almost any vehicle and application. Its firmware is compatible with a wide range of various control hardware. With its advanced data logging and analysis capabilities, as well as reliable simulation tools, ArduPilot remains at the forefront of technological development. Being open-source, it enjoys widespread adoption by numerous companies, research institutions, and corporations such as NASA and Intel (Luo et al., 2019), (ArduPilot.org, 2023).

5.1.2.2 Autopilot Hardware

Pixhawk 6 autopilot was selected as autopilot hardware for the current application. It is open-source hardware that provides high-performance autopilots that have been used in fields like hobby remote vehicle design, industrial-grade autopilot applications, and academia. It has onboard Inertia Measurement Unit (IMU) that can measure parameters such as model DOF. The Pixhawk serves as a central hub that receives data from other sensors and controllers and sends control signals to Electronic speed controller (ESC), and servos (Luo et al., 2019), (PIXHawk.org, 2023).

5.1.3 Raspberry PI

A Raspberry PI is a single board computer that acts as the technological brain of the ship model. Generally, the Raspberry PI, like any other computer, is not limited to a single way of use as stated by Richardson and Wallace (2012). It offers more capabilities than autopilot (Pixhawk 6) in terms of data logging and data analysis. It also provides a high degree of autopilot system customization.

The Raspberry PI features General Purpose Input/Output (GPIO) pins and USB 3.0 interface, which enable connectivity with external devices and components. These pins can be used to interface with sensors, servos, motors, and other electronic components commonly found in RC models (RaspberryPi.com, 2023). It also provides an extension in storage space that can be utilized to store more log files, if needed.

The Raspberry Pi has built-in support for wireless communication protocols such as WiFi. This capability enables the Raspberry Pi to establish wireless connections with other devices, including telemetry modules allowing data transmission between the RC model and external devices.

Because of the resemblance between the Raspberry Pi and the Autopilot in terms of flight control functionality. Therefore, having both components onboard the model will add a degree of redundancy to the system since the Raspberry Pi can perform some of the Autopilot functions in case of Autopilot failure.

5.1.4 Rudder and rudder control

Following the same scaling concept, the model rudder dimensions were derived from the reference ship's rudder. Then, the nearest commercially available rudder was selected (MHM-

Modellbau.de, c).

Rudder's rotation is controlled by a servo which is an electro-mechanical device that receives a signal from the autopilot depending on the operator's commands, and by turn will rotate its internal motor to the desired position.

The required torque for the servo was calculated to counter the potential lateral force acting on the rudder center of pressure (the same concept used for full-scale ships). For this, the formula from Lloyd register rules (Register, 2023). The force acting on the rudder and the torque required to rotate the rudder are calculated using Equation (5.1) and Equation (5.2) respectively. Rudder dimensions and configuration is shown in Figure 5.1.

$$C_R = 132 \cdot K_1 \cdot K_2 \cdot K_3 \cdot A \cdot v^2 \quad (5.1)$$

$$Q_R = C_R \cdot r \quad (5.2)$$

Table 5.1: Rudder force and torque calculation

Parameter	Note	Value	Unit
Rudder span (h_R)	Rudder geometry Figure 5.1	0.067	m
Rudder area (A)	From rudder geometry	0.00246	m^2
λ	h_R^2/A_t	1.83	
k_1	$(\lambda+2)/3$	1.28	
k_2	Coefficient (rudder profile)	1	
k_3	Coefficient (rudder location)	1	
v	$(v_{ahead}+20)/3$	7.752	Knots
Rudder force (C_R)	$132 \cdot K_1 \cdot K_2 \cdot K_3 \cdot A \cdot v^2$	18.6	N
c	Rudder geometry Figure 5.1	0.037	
α [1]		0.33	
k_1 [2]	A_f/A	0.20	
A_f	Area forward rudder stock	6.4×10^{-4}	m^2
r [3]	$c(\alpha - k_1)$	0.00259	m
Rudder Torque	$C_R \cdot r$	0.06	N.m
Minimum required servo torque (Q_R)		0.755	Kg.m

[1] Relative center of pressure along the chord length

[2] Ratio of the rudder blade area forward of the rudder stock centreline

[3] Distance from the center of pressure to the centreline of the rudder stock

Two servos (MHM-Modellbau.de, d) were selected (one per rudder). The specifications of the selected servos are shown in Table 5.2.

Table 5.2: Rudder servo specifications

Parameter	Value	Unit	Parameter	Value	Unit
Manufacture	Torcster		Weight	20.0	g
Technology	Digital		Min. operating voltage [V]:	4.8	V
Length	28.2	mm	Max. operating voltage [V]:	6.0	V
Width	12.8	mm	Operating time at 4.8V (4 cells) [sec/60°]	0.14	
Height	26.9	mm	Torque at 4.8V (4 cells)	2.5	Kg/cm

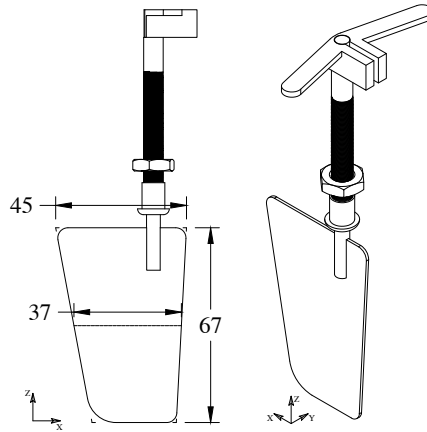


Figure 5.1: Ship model rudder dimensions , in mm

5.1.5 Telemetry module

The telemetry module is an essential component within RC models, allowing the RC operator to monitor various real-time operating parameters captured by the sensors through a computer screen. The telemetry model onboard the ship model will transmit the data to the stationery telemetry module onshore.

5.1.6 Propellers

The reference ship has twin-screw propellers with five blades. Following the scaling factor of 16.61, the model propeller's diameter is 65 mm. Obtaining a calibrated propeller with this diameter was not feasible within the time frame of the thesis. Therefore, it was decided to opt for the commercially available propellers that align with the required diameter and number of blades.

The propeller open water characteristics curves, either obtained experimentally (open water test) or numerically (CFD), will serve as a validation tool to ensure the quality of the obtained operational data. The measured propeller torque and RPM can be used to derive the torque coefficient with the help of the relative rotation efficiency and wake fraction. Then the obtained coefficient with its corresponding advance coefficient (J) is to be plotted on the open water characteristics curves to show how it correlates to the reference curve.

5.1.7 Propulsion electrical motors

The electrical motors used for the propulsion system are Brushless DC electric motor (BLDC). The BLDC motors have been used widely in building Unmanned aerial vehicle (UAV)s (Gong et al., 2018). Contrary to brushed motors, brushless motors have the rotor as a permanent magnet and stator where the coils are arranged as illustrated in Figure 5.2. This configuration will allow the winding of opposite coils as a single coil to generate opposite poles to magnet poles which in turn will double the attraction force. Additionally, this configuration also allows synchronizing the coil powering in a way that some of the rotor magnets will be attracted and some magnets will be repelled (Yedamale, 2003). This will increase the brushless

motor efficiency and degree of control, and since that, there are no brushes or commutator to be worn and replaced - as in brushed motors - the BLDC lifetime is longer (Millet, 2022).

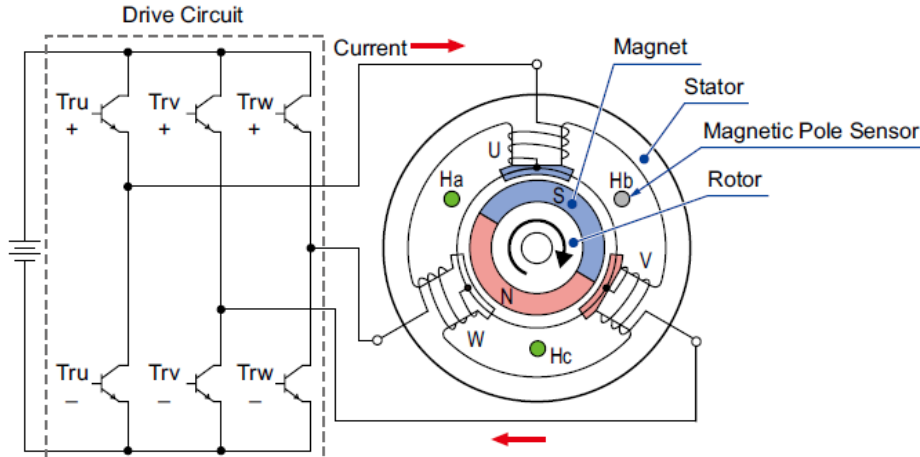


Figure 5.2: Simplified brushless motor diagram (Tang, 2021)

Electric motors were sized based on the resistance experimental results corresponding to the maximum model speed. Since the available propellers were not provided with the corresponding thrust coefficient (K_T), torque coefficient K_Q , and the open water efficiency (η_o) curves. Therefore, some efficiencies were conservatively assumed for the motor sizing. The required motor characteristics are concluded in Table 5.3 and the detailed calculations are shown in Appendix D.

Table 5.3: Electric motor required parameters

Parameter	Value	Unit
Power	14.43	Watt
Revolutions per minute	1185-1975	RPM
Motor torque	0.111-0.137	Nm

The suitable commercially available motor from *Faulhaber* motor manufacturer which provides calibrated electric motors in this scale. The chosen model is (Model No.4490H024B) (Faulhaber.com). Specifications are shown in Table 5.4.

Table 5.4: The proposed electrical motor specification

Parameter	Value	Unit	Parameter	Value	Unit
Nominal voltage	24	V	Rotor inductance	73	μH
Terminal resistance	220	$m\Omega$	Slope of n-M curve	3,6	min^{-1}/mNm
Torque constant	24,2	mNm/A	Rotor inertia	130	gcm^2
No load speed	9.700	min^{-1}	Mechanical time constant	4,9	ms
Stall torque	2,64	Nm	RTH2 Reduction	30	%
Speed constant	395	RPM/V	Efficiency max.	87	%

Due to the long delivery time expected from the motor supplier, it was decided to use

another motor that has less delivery time to comply with the thesis time constraint. The selected motor model is MAX Marine P359 (MHM-Modellbau.de, e). Full specifications are shown in Table 5.5.

Table 5.5: Alternative employed electric motor specifications.

Parameter	Value	Unit
Voltage range	6 - 14.4	V
kV	350	RPM/V
Motor rated speed	5040	RPM
Case dimensions	35 x 36	mm
Shaft diameter	5	mm
Required ESC for 4S battery	120	A

5.1.8 Electronic speed controller

The ESC is a widely used device for electric vehicles, it holds the electric motor speed constant in case of varying loads without any interface of the vehicle operator (Follmer, 1974; Gong and Verstraete, 2017). Another application where ESC is utilized is UAVs which share some similarity with this current application in term of employing an ESC and a link between the power source and BLDC (Gong et al., 2018).

The ESC receives an input signal (generally from the autopilot) and converts it electronically to a Pulse width modulation (PWM) signal which in turn regulates the motor speed and output power. Additionally, the PWM signal can reverse or stop the motor (Follmer, 1974; Gong and Verstraete, 2017).

The ESC is sized with respect to the electric motor peak amperage. The compatible ESC for the originally selected motor is (Faulhaber.com) with a current rating of up to 16 Amps. However the provided ESC is (MHM-Modellbau.de, f) with a current rating of up to 120 Amps which is compatible with the alternative motor provided.

5.1.9 Buffer battery

A buffer battery is used onboard the model as a backup solution in case of failure of the EGM. Battery sizing was based on the total required power demand within the model for a pre-defined period of time. It was sized to keep the whole system running for 15 minutes (Sailing mode) and to keep auxiliary components (eg. the other components except the motors) for an additional 0.75 hours (Harbour mode). The reason behind allocating extra operating time for auxiliary components, such as the control and telemetry module, is to ensure their continued operation after each run for tasks such as system checks and data transfer. By allowing additional time, these components can perform their intended functions without interruption or time constraints, to maintain seamless communication and data management processes.

After summing up the maximum power demand from all components, the battery energy (in Wh) and charge capacity (in mAh) are calculated using Equation (5.3) and Equation (5.4) respectively.

$$\text{Battery energy, in Wh} = \text{Total power demand, in watts} \times \text{Operating time, in hours} \quad (5.3)$$

$$\text{Battery capacity, in mAh} = \frac{1000 \times \text{Battery energy, in Wh}}{\text{Battery voltage, in V}} \quad (5.4)$$

The summary of the battery sizing calculation is shown in Table 5.6.

Table 5.6: Battery sizing calculation summary

Component	Power demand, in watts	
	Sailing mode	Harbour mode
Raspberry PI	15.3	15.3
Receiver	0.273	0.273
Autopilot	9	9
GPS module	0.75	0.75
Telemetry Module	0.5	0.5
2 X Speed controller	5.4	5.4
2 X Propulsion motor	50	
Sum	81.225	31.225
Operation time, in hr	0.25	0.75
Battery energy, in Wh	20.31	23.42
Total required battery energy, Wh		43.73
Total required battery energy + 15% margin, Wh ^[1]		50.28
LiPo 4S battery voltage		14.8
75% Required capacity, in mAh ^[2]		3397.55
100% Battery capacity, in mAh		4246.94

[1] 15% margin was added to compensate for any uncertainty in load calculation

[2] The total required capacity was increased by 20% to keep battery depth of charge at 80% to increase battery life

Lithium polymer (LiPo) batteries are commonly used in RC vehicles. It features several advantages such as lightweight, high energy density, and small size (Mehendale, 2021). Considering the current application power demand and other equipment operation range, a 4S battery was chosen which has a voltage range of up to 14.8 volts. For redundancy, two batteries with (Y) connection were installed on board. This type of connection increases the total capacity with the same voltage. Table 5.7 shows the chosen battery specifications (MHM-Modellbau.de, g).

Table 5.7: The chosen battery specification

Parameter	Value	Parameter	Value
Voltage [V]	14.8	Discharge rate [C]	30
Number of cells	4	Discharge current [A]	150
Capacity [mAh]	5000	Charge rate [C]	4
Energy [Wh]	74	Charging current [A]	20
Length [mm]	163	Balancer connector	XH
Width [mm]	46	Connector	XT90
Height [mm]	30	Manufacture	SLS
Weight [g]	468		

Power distribution through the various model component is achieved by the Power distribution board (PDB) which serves as a centralized hub for distributing electrical power from the model’s battery to various subsystems, minimizing the complexity of wiring and providing a clean and organized power supply.

5.1.10 Battery charger

Batteries are planned to be charged onboard by the dynamo only when required. Therefore, the dynamo should alter its output power to prevent overcharging the batteries while powering up the other component onboard. Also, the electricity generated from the dynamo should be properly distributed between the battery and other loads.

This will increase the complexity level of the required charging system since the battery charging process needs to be regulated. Additionally, the dynamo output voltage is required to match the battery charging voltage. Information such as charging time, input and output voltage as well as current, and battery SOC are required to be recorded as operational data.

On top of that, all these operations are required to be done autonomously with no manual interference from the RC operator. This means that the system should decide what to do according to the battery SOC and total required power.

A proposed solution that can achieve these requirements is to build a Printed circuit board (PCB) that can be customized to achieve this task.

PCB is a cornerstone component in almost all electronic products (LaDou, 2006). It is a board that can be used to assemble microelectronic components such as microcontrollers, microprocessors, and programmable logic devices and provide an electrical interconnection among them. The reason behind its widespread utilization is its advantages features such as low cost and weight. Additionally, it provides a high degree of customization for specific applications (Montrose et al., 1996).

In the current applications, the PCB will also play a central role in the Energy Management System (EMS) which will be discussed in detail in Chapter 6.

5.1.11 Permanent components parameters and measuring devices

The following list is showing how some parameters which are related to permanent components will be recorded during the operation

- **Battery voltage, and current drawn** parameters are measured using the Pixhawk 6 autopilot or the PCB.
- **Acceleration, Gyro, and DOF** parameters are measured by the internal IMU in the Pixhawk 6 autopilot.
- **Speed and location** parameters are measured using the Holybro M9N GPS module attached to the Autopilot.
- **RPM and torque** parameters for the electrical motors are planned to be measured using a torque sensor with a measurement rating of 0.5 Nm and 7000 RPM ([Futek.com, a](#)).
- **Rudder angle** can also be captured through the servo signal recorded in the autopilot, but it requires a prior calibration between the servo input and the rudder angle.
- **Draft** usually does not significantly change during the runs. However, during the towing test, a dynamic draft was noted at high speeds. This will acquire to measure the draft continuously during operation. This can be achieved by using two static pressure sensors at FORE, AFT, and midship locations at the outer surface of the bottom. By this configuration, a real-time reading of the mean draft and trim will be provided continuously. The proposed solution is ([Conrad.de, a](#)) which is compatible with both the Raspberry PI and the Autopilot (Pixhawk 6).

5.2 Interchangeable component

Interchangeable components group encapsulate the EGM components that will be required to be exchanged with other module in future development.

5.2.1 Dynamo

The dynamo ([Amazon.de](#)) sizing was determined by considering the aggregate power requirements outlined in [Table 5.6](#). The total power demand including a 15% safety margin is 50.28 watts. The nearest commercially available dynamo has a power rating of 100 watts. However, a dynamo with a capacity of 300 watts was chosen to ensure compatibility with the nearest available fuel cell module. While the fuel cell module is not intended for utilization within the scope of this thesis, it was selected with an equivalent capacity to facilitate meaningful comparison between the two modules in the future. The dynamo parameters are mentioned in [Table 5.8](#).

Table 5.8: The proposed dynamo parameters

Parameter	Value	Unit
Rated power	300	w
Voltage (DC with a rectifier)	12	V
Number of revolutions	600	RPM
Start Torque	0.35	Nm

5.2.2 Combustion engine

A CE is used to drive the dynamo. The CE choosing criteria is based on the required RPM and torque for the dynamo. The nearest commercially available engine was selected (MHM-Modellbau.de, h). The engine parameters are shown in Table 5.9.

A gearbox (OMC-Stepperonline.com) with a reduction ratio of 10:1 is employed to match the engine output RPM with the dynamo input RPM.

Table 5.9: The proposed combustion engine parameters

Parameter	Value	Unit
Rated power	514	w
Number of revolution	5000-30000	RPM
Torque range	0.16-0.98	Nm

5.2.3 Engine auto-start system

The currently available engines are manually starting engines (eg. pull start mechanism) which is not appropriate in the current context as will be explained in Chapter 6. Consequently, an automatic electric start-up system is employed to fully automatize the system. This automatic starting system consists of a separate battery powering a separate electric motor that can be initiated remotely to start up the CE. The system chosen is an integrated system (NitroRCS.com) than can be fixed in the model and be connected permanently to the engine.

5.2.4 Fuel pump and fuel tank

The fuel pump (ErcMarket.com) is fitted to regulate the fuel flow between the fuel tank and the CE. It serves also in shutting down the running engine by cutting off the fuel supply to it. The pump specification used in this task is shown Table 5.10.

A 500 ml capacity nitro fuel (Conrad.de, b) tank was also chosen to ensure continuous fuel supply for the engine. Usually, the tank should be sized with known data about engine Specific Fuel Consumption (SFC) and the desired time for the run. The SFC for the chosen engine is provided. Therefore the tank was chosen with respect to the available volume in the model hull.

Table 5.10: The proposed fuel pump specification

Parameter	Value	Unit
Voltage range	4.8-6	V
Flow rate	1000	cc/minute
Lift	0.8	m
Weight	175	grams

5.2.5 Interchangeable components parameters and measuring devices

- **Fuel flow** is to be measured using a flow meter ([Conrad.de](#), c). It is a widely used sensor in the field of RC models with a minimum sensitivity of 20 ml/min. Another alternative solution with a sensitivity of 1 ml/min has different digital interface options for data transmission ([Digikey.de](#)).
- **Fuel level** in the tank can be measured using ([HobbyQueenItalia.com](#)). it is compatible with FrSky telemetry through FrSky FSH-01 Sensor Hub.
- Similarly to the electrical motors, the CE, and the dynamo will also require torque sensors to measure the torque and RPM values. But with a higher range of torque ([Futek.com](#), b).

5.3 Component interconnection

After delineating each of these distinct components and explicating their individual functions, the focus now shifts to comprehending the interactions among these components.

Figure 5.4 illustrates a diagrammatic scheme of components mentioned before, showing their dependencies and how they are correlated to each other. Also, it gives some insight into energy generation and distribution among various components. As well as the signals' path through the system. A breakdown explanation of this diagram is provided in the following bullet points:

- The receiver is where the signal enters into the system after the RC operator sends a command via the transmitter.
- The autopilot is acting as the central hub of the control system. It receives the control signal from the receiver and transmits it to its corresponding components. It also can transmit data and command signals from and to the Raspberry PI. Sensors that are compatible with the ArduPilot will also record their reading into its internal storage unit. In addition, it has its own IMU that also records all data in the same storage unit. it also stores parameters from the battery.
- The PCB is the connecting link between both interchangeable and permanent components. It is the core of the EMS since it regulated the power supplied by the dynamo and the battery and transmits it to the PDB. It also power and control the engine throttle servo to control the amount of energy input to the system. It has a data connection to the Raspberry PI where it can store its captured readings.
- The PDB is also the central electrical energy hub in the system, it transfers the electrical

power from the PCB to the rest of the components. With the increasing number of components that demand separate power supply, a power distribution module can be utilized.

- In the bottom right, the EGM system is illustrated its components and their correlation with the other permanent components.
- Through the telemetry module, some operational data can be transmitted instantaneously to the Gounod station. The telemetry module can receive data from the autopilot or the Raspberry PI.
- As mentioned, the ESC is regulating the BLDC's RPM under various loads. The latter is deriving the propellers.

It is worth mentioning that due to some similarities between the Autopilot and Raspberry PI functions, any decision to switch functionalities between the two components might require minor modifications to the proposed diagram and correlation matrix.

To have a broader picture of the proposed system, a correlation matrix is shown in [Figure 5.3](#). In this matrix, all components, sensors, and also parameters of interest were listed as shown. Hence, the interaction between each pair of components is specified at the intersection cell.

For instance, the intersection between the fuel pump row and the CE column is denoted by the blue box which means "Feed" in the matrix legend. Another example for the BLDC motor torque sensor, it interacts with the BLDC with a green box which means "Measure" and intersects with the Raspberry PI with a green box with a blue circle which means "record".

Some components have two correlations or actions to an individual component. for instance, the ESC row intersection with the BLDC motor column is donated with two different symbols which means "Control" and "Electrical feed" since the ESC do both actions to the BLDC motor.

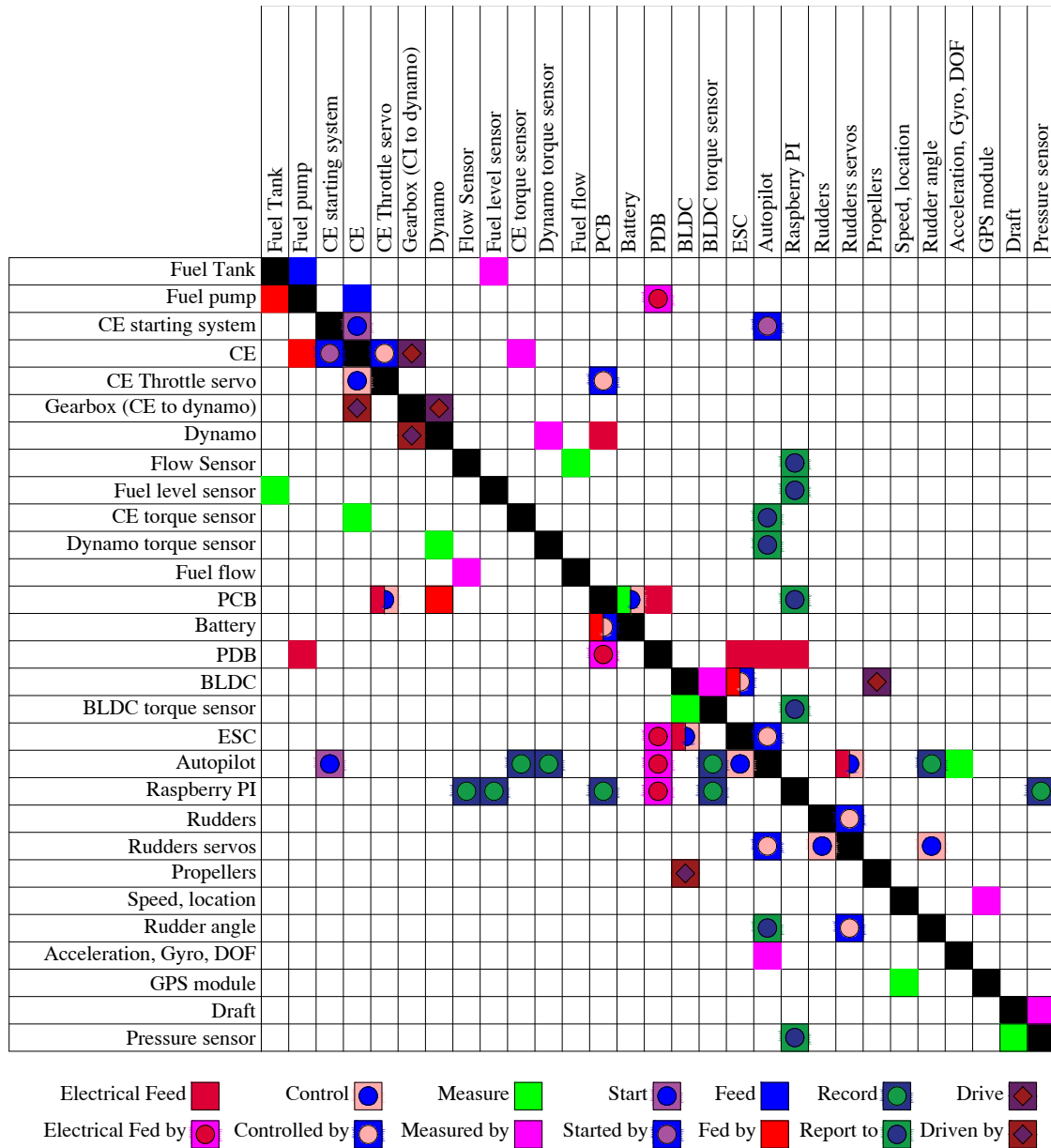


Figure 5.3: A correlation matrix of components illustrates the interconnection among individual components as well as the measuring parameters

5.4 Miscellaneous component

In addition to the permanent and changeable components mentioned before, there are furthermore small components that were necessary to provide fixation and interconnection between these main components. These components are such as connectors between the rotary parts, cables with different adapters, and for sure plenty of various types of screws. Customized 3D-printed parts were also printed to fulfill specific needs where there are no commercial solutions available.

In order to ensure watertightness where the rudder stock is penetrating the hull, and due to the hull surface curvature at this area. Customized 3D printed fins were printed so one of their sides will fit on the hull curvature from the outside and the other side will provide a flat horizontal surface. This flat surface will offer a good contact area for the water-tight seal of the rudder shaft. Additionally, a propeller holder was designed and 3D-printed with respect to the stern tube size and hull shape. both parts are shown in Figure 5.5.

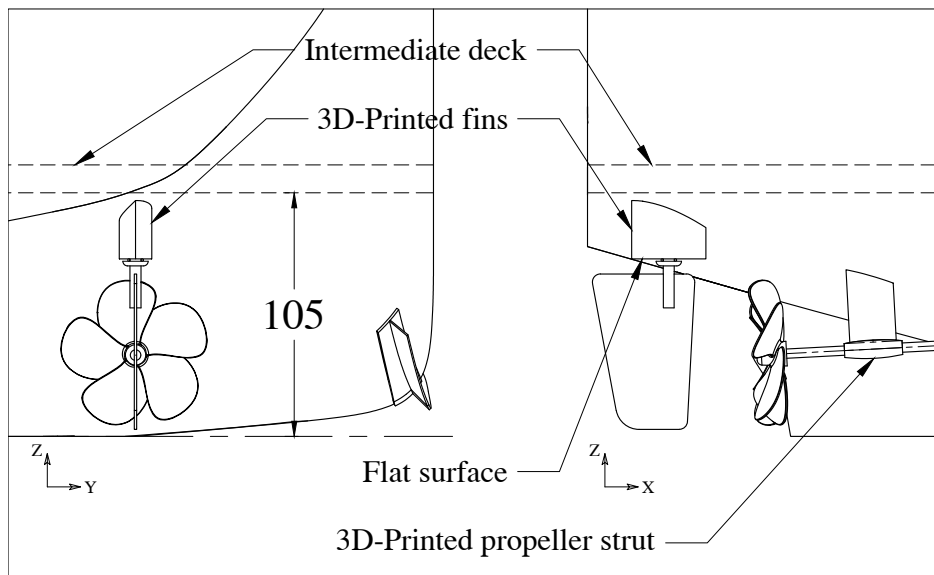


Figure 5.5: 3D-Printed parts (Dimension in mm)

5.5 Model assembly planning

The above-mentioned components were distributed within the hull taking into account some factors such as the available space within the model hull, each component function, as well as considerations regarding accessibility and ease of interchangeability.

First of all, Medium-density fibreboard (MDF) plate was fixed on the model's bottom. It is used as a horizontal surface to facilitate aligning components. It also serves as a protective layer to safely use bolts to fix the components in place.

An intermediate deck was fitted at the AFT of the model. It serves as a platform for fixing the rudders' servos. Figure 5.8, Figure 5.7 and Figure 5.6 shows the proposed arrangement of the component inside the hull. Also, the components are listed in Table 5.11.

With respect to the end of the propeller shaft inside the hull and the dimensions of the coupling, motors were placed and eventually the ESC. The PDB is then placed to provide the connection between the ESCs and the batteries.

As a general note, it should be acknowledged that the physical model's layout could deviate from the layout provided. Such modifications are primarily aimed at improving cable management. However, these adjustments do not pose significant challenges, as the majority of components are situated along the model's center line. Furthermore, the model's draft is intended to be attained using solid weights, which can also serve to adjust the trim.

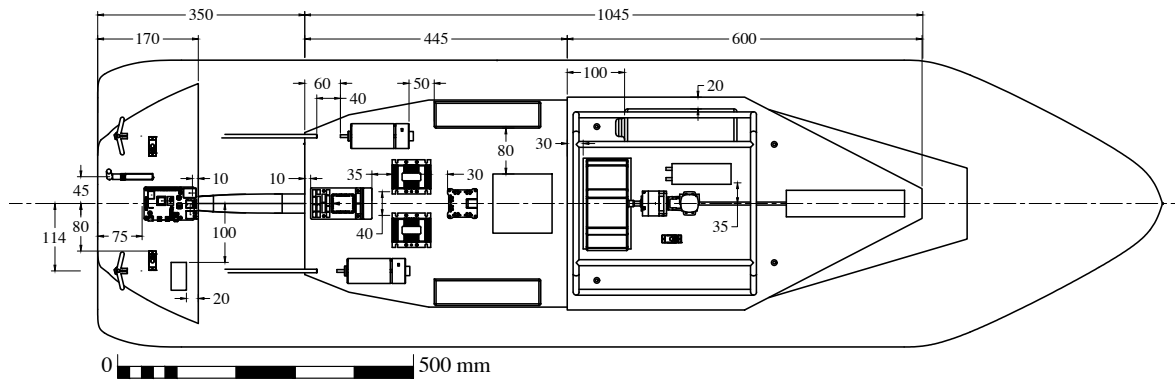


Figure 5.6: Arrangement of components in a two-dimensional layout, with dimensions specified in millimeters.

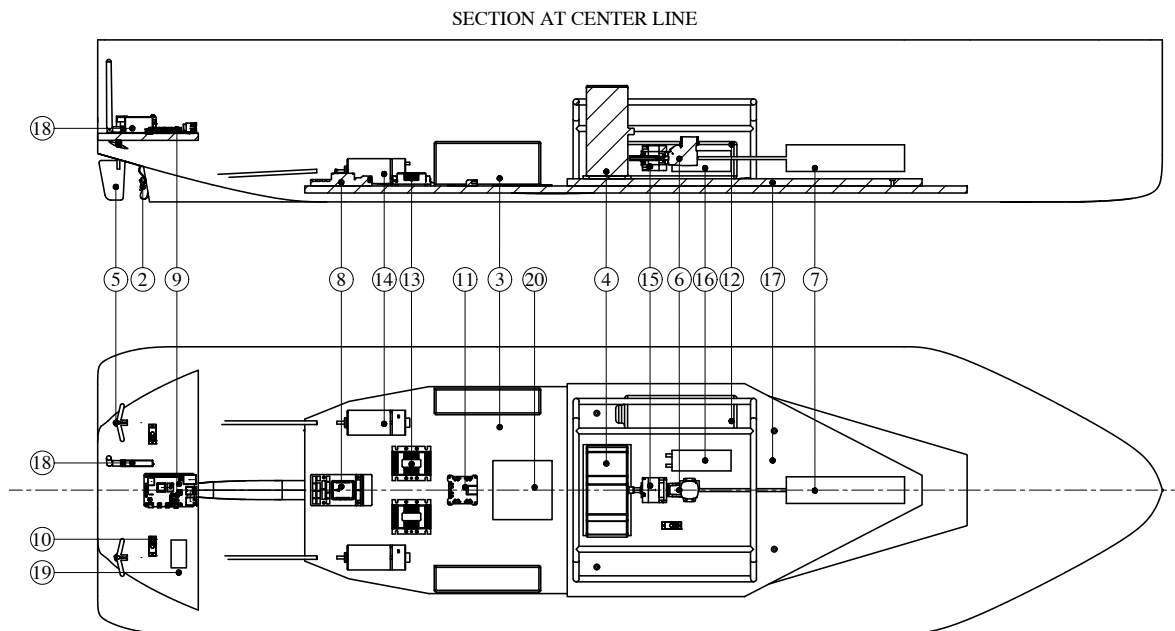


Figure 5.7: Arrangement of components in a two-dimensional layout

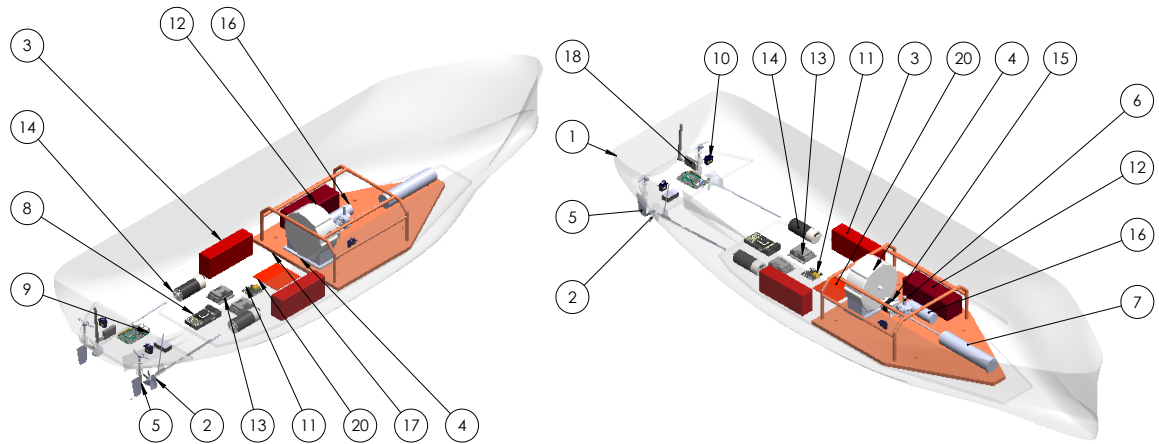


Figure 5.8: Arrangement of components in 3D perspective views

Table 5.11: List of major components

No.	Item	Description	Quantity
1	Hull	GFRP 16.61:1 scaled-down model	1
2	Propeller	5 blades, 65 mm diameter, 6.5 mm pitch	2
3	Battery	4S LiPo 5000 mAh battery	2
4	Dynamo	300 watts. 12 volt DC with rectifier	1
5	Rudder	67x45mm	2
6	Combustion engine	O.S. Max-12TG-X 12E Pull-start	1
7	Electric starter	E-Starter with 2S LiPo 1800 mAh battery	1
8	Autopilot	Pixhawk 6	1
9	One-board computer	Raspberry PI 4	1
10	Rudder Servo	Torcster Mini Servo NR-85 MG Digital 20g	2
11	PDB	Pixhawk PX4 Mini PM06 V2	1
12	Fuel tank	Nitro fuel tank 500 ml	1
13	ESC	EzRun MAX10 G2, 140A	2
14	Brushless DC electric motor	MAX Marine P359 350KV	2
15	Gearbox	Nema 17 Gear Reducer Ratio 10:1	2
16	Fuel pump	4.8-6v, Flow rate: 1000cc/minute	1
17	Interchangeable plate	MDF plate with handle	1
18	Telemetry module	FrSky	1
19	Receiver	ARCHER-R8 Pro Receiver	1
20	PCB	Printed Circuit Board	1

As explained before, the interchangeable components containing the EGM are assembled into one unit that can be easily dismantled from the model and replaced with any other EGM for future analysis. Figure 5.10 demonstrates this idea.

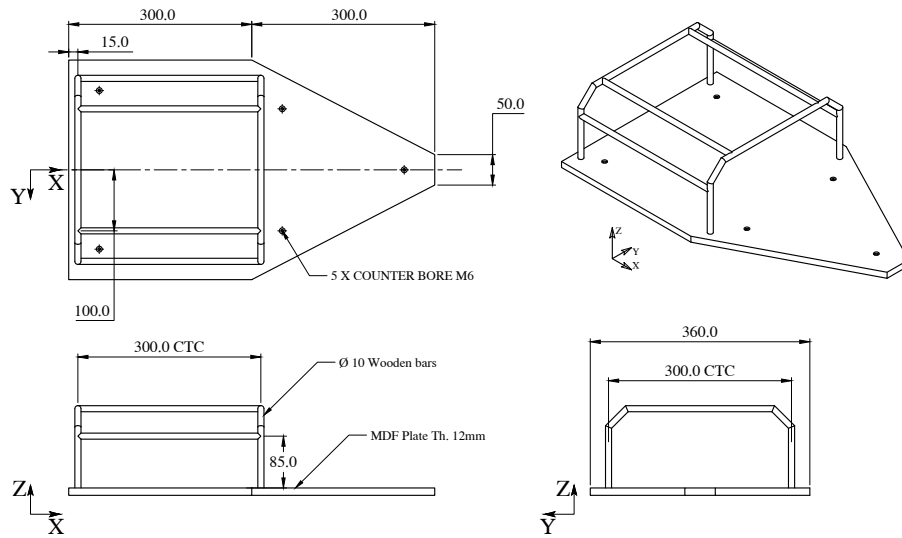


Figure 5.9: Proposed design of the interchangeable plate intended to enclose the EGM components, with dimension specific in millimeters

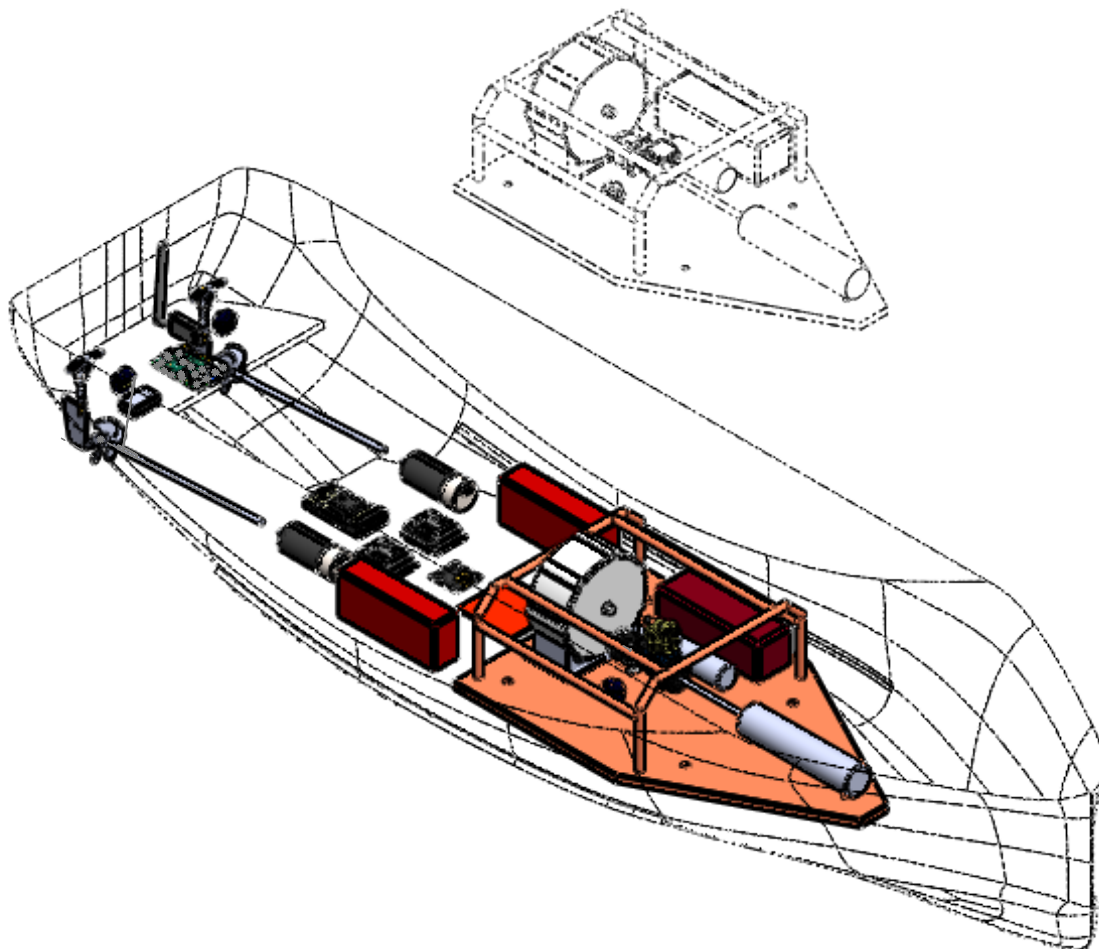


Figure 5.10: A 3D illustration of interchangeability feature for the EGM components

5.6 Components weight list and price

In the detailed design phase, it was necessary to have a general figure about the expected total cost of the model and also the approximated weights of the intended components with the hull. This will serve as a reference point for future comparisons and reflections. The list shown in Table 5.12 comprises the components' designations, quantity, price, weight, and acquisition status.

The acquired components' prices were directly listed when purchased. However, the prices of the proposed components were obtained from different online stores. These prices might be subjected to fluctuations upon actual procurement or alternations suppliers. Similarly, the weights obtained from these stores (if available) might slightly deviate from the actual supplied component weight.

Furthermore, elements utilized for fixation and interconnection among all components pose a challenge in terms of weight tracking, so the proposed procedure is to weigh the entire model when all the installation work is done. This measured weight is then compared with the theoretically calculated displacement at a draft of 9 cm. The difference will represent the needed solid weight to maintain that draft. This will cover any uncertainty in the weight calculation.

Nevertheless, this list is a first iteration and will be anticipated to expand progressively as the project advances.

Table 5.12: List of major component weight and cost

No.	Item	Description	QTY	Weight (grams)	Price	Status
1	Hull	GFRP 16.61:1 scaled-down model	1	10680	158.62 €	Acquired
2	Propeller with stern tube	5 blades, 65 mm diameter, 6.5 mm pitch	2	103.8	46.86 €	Acquired
3	Battery	4S LiPo 5000 mAh battery	2	468	127 €	Acquired
4	Dynamo	300 watts. 12 volt DC with rectifier	1	2750	157 €	Proposed
5	Rudder	67x45mm	2	35	18.88 €	Acquired
6	Combustion engine	O.S. Max-12TG-X 12E Pull-start	1	251	154 €	Proposed
7	Electric starter	E- Starter with 2S LiPo 1800 mAh battery	1	600	55 €	Proposed
8	Autopilot	Pixhawk 6	1	51	504.16 €	Acquired
9	One-board computer	Raspberry PI 4	1	46	77.95 €	Acquired
10	Rudder Servo	Torcster Mini Servo NR-85 MG Digital 20g	3	20	50.7 €	Acquired
11	PDB	Pixhawk PX4 Mini PM06 V2	1	36	18.45 €	Acquired
12	Fuel tank	Nitro fuel tank 500 ml	1	95	18 €	Proposed
13	ESC	EzRun MAX10 G2, 140A	2	120	92.35 €	Acquired
14	BLDC	MAX Marine P359 350KV	2	78	58.15 €	Acquired
15	Gearbox	Nema 17 Gear Reducer Ratio 10:1	2	528	44.88 €	Proposed
16	Fuel pump	4.8-6v,Flowrate: 1000cc/minute	1	175	49 €	Proposed
17	Interchangeable plate	MDF plate with handle	1	1610		Proposed
18	Telemetry module	FrSky	1	16.6	100.80 €	Acquired
19	Receiver	ARCHER-R8 Pro Receiver	1	13	44.45 €	Acquired
20	Remote control	Taranis X20s	1		514.29 €	Acquired
21	GPS Module	Holybro M9N GPS	1	32	75.59 €	Acquired
Summation				17708.4.6 Grams	2366 €	

6

Energy management system

In the detailed design of the model, it is required to have one interchangeable EGM along with other permanent components such as the propulsion system and control unit. The current scoop is including the EGM configurations based on the CE

As discussed before, the architecture of the current EGM consists of one CE driving a dynamo. This architecture also includes a buffer battery which can provide a temporary backup power source for the system for a short period of time. Having two or more power sources onboard will categorize the EGM as a hybrid system (Nguyen et al., 2021).

In full-scale marine vessels batteries are commonly used with the generators for various purposes such as: adding a degree of freedom to the system to control and optimize the onboard power. Batteries can provide the needed power when the generators are shut down to prevent operating in low-efficient regions. When the generated energy is higher than the demand, the excess energy can be unitized by charging the batteries. Batteries can boost the generator to drive the system in case of high energy demands (Bui et al., 2018).

Therefore, with all these processes in a hybrid powering system - generator with batteries in this case - it is essential to develop an EMS to adequately distribute the power among various components onboard and obtain the maximum efficiency from these different power sources. (Bui et al., 2018).

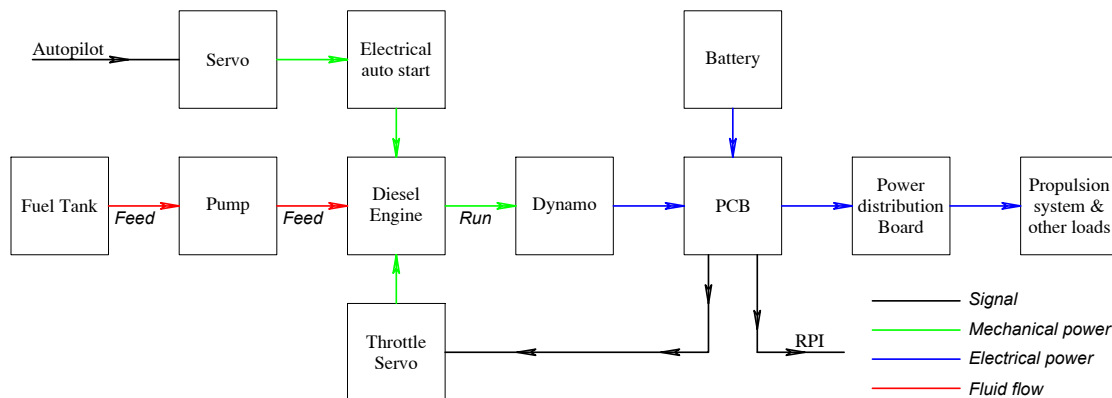


Figure 6.1: The diagrammatic representation of energy generation module based on a combustion engine

Returning to the power train configuration for model scale, the dynamo is driven by a CE to generate the necessary power to charge the batteries besides fulfilling the system power demand. When the battery is fully charged, the dynamo will only generate the power to fulfill the other components' power demand. In emergency cases when the EGM is out of

service for any reason, batteries can provide a backup solution to ensure continuous sailing for the model to reach a nearby service area. The described EGM with all its components and auxiliaries is diagrammatically presented in Figure 6.1.

The EGM start-up, power control, and shutdown processes are regulated through different components which are mainly controlled by signals from the control module (eg. the autopilot, the Raspberry PI or the PDB). These processes are described as follows:

- **System start-up:** This is done through the electrical auto start-up system (described before) which is triggered by a servo pushing its button.
- **Dynamo power alter:** This is done by controlling the CE output power by controlling its throttle which eventually will control the dynamo-generated power. The throttle is also controlled by a separate servo which is a common practice for RC models.
- **Engine shutdown:** This is done by cutting off the fuel supply to the engine which can be executed by shutting down the fuel pump.

These crucial processes can be executed via control signals. However, these processes are still manual and require the RC input signal to be triggered. It is obvious now that it would be beyond the operator's capabilities to manually synchronize all these processes besides the safe operation on the model. Therefore, it is necessary to automate their occurrence according to the operational needs.

The suggested method for utilization is a PCB, offering a high level of flexibility for customization to meet the energy management system requirements. The PCB board is expected to regulate the following processes:

- Start/Stop battery charging according to battery SOC.
- Provide a control signal to the engine throttle servo to alter the dynamo output.
- Alternate between the battery or the dynamo as the main source of power according to the operational needs.
- Provide operational data about battery voltage, SOC, and charging start/end time and charging period.

With more information known about the CE efficiency graphs, this proposed EMS can be extended to engage the batteries while the power demand is low where the CE is expected to operate in a low-efficiency region.

The correlation between these processes and their occurrence is illustrated in Figure 6.2, which can be considered as the bases for programming the PCB.

To conclude these processes in a practical way, assuming the RC operator is sailing the model at low speed where the power demand is relatively low, then the model will use only batteries in this case. If the RC operator pushed the throttle to achieve higher speed, the PCB will automatically trigger the CE which in turn will operate the dynamo. The latter will be then the main power source as long as the required power is in range with the CE high-efficiency operation region.

Another practical scenario assumes that the model runs on low power demand where the battery SOC reaches a critical level. Then, and automatically without the interference of

the RC operator, the CE will be started up to assign the dynamo as the main power source. The latter will continue sailing the model even if it is operating in a low-efficiency region but additionally, it will charge the empty batteries.

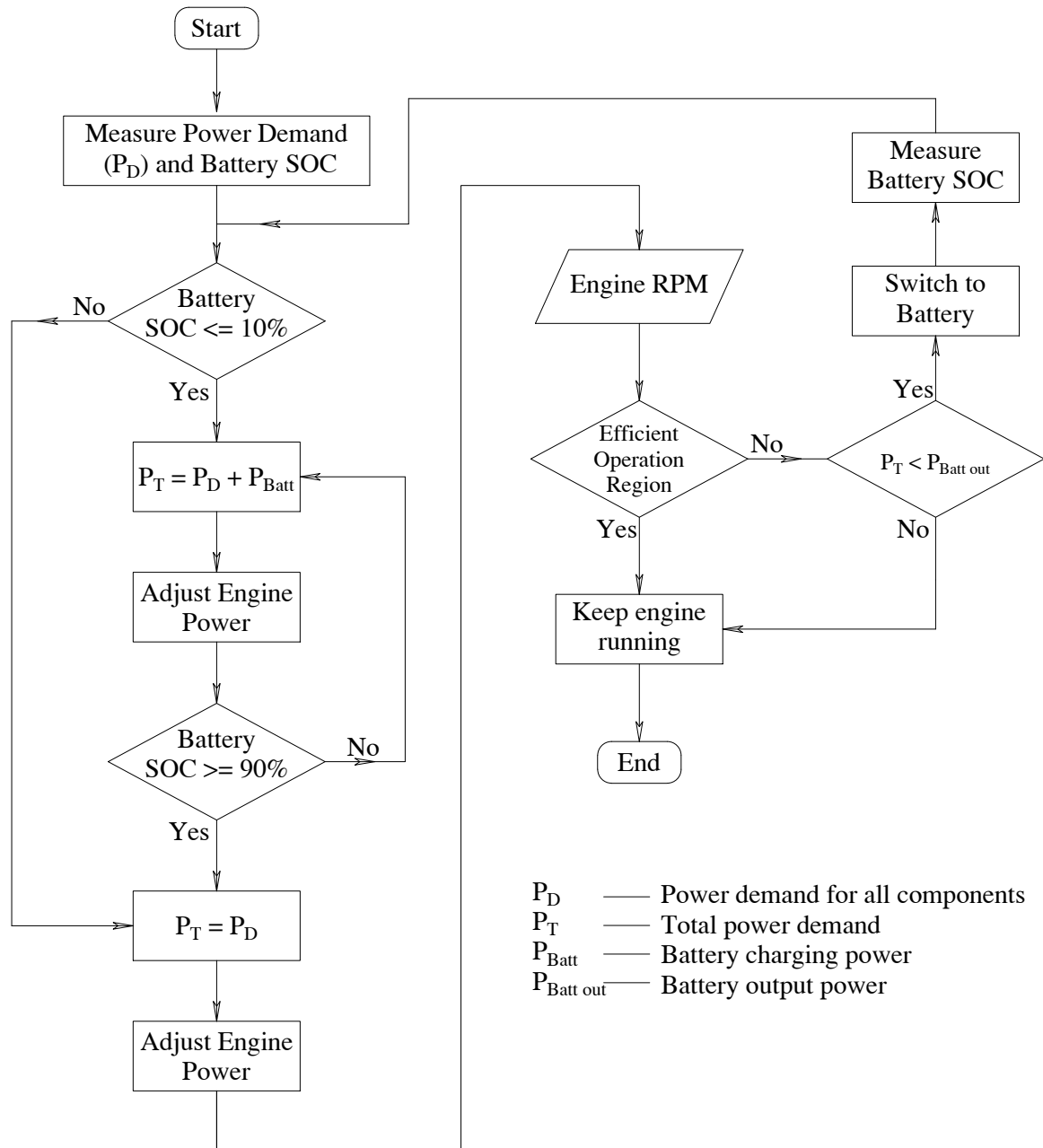


Figure 6.2: The proposed energy management system flow chart

This page intentionally left blank.

7

Data model development

After harvesting the data from multiple sources, it became necessary to organize and store it in a manner that retrieval and restoration were done smoothly. To achieve this task efficiently, data model system is conceptualized. The data model should involve organizing data captured from different sources. This structure is not only helpful in terms of data analysis but also will give insight into how these parameters are correlated (Jabary et al., 2022; Kim and Kim, 2017).

To effectively process and provide structured ship operation data, it is necessary to synchronize and identify the relationships between various data collected from different resources and at different frequencies. This will be one of the cornerstones for efficient data analysis. Therefore, the data context should be established similarly to the context of the physical entities.

As discussed in previous chapters, the main objective of this application is to evaluate the performance of the energy system of a scaled ship model that will require the analysis of different types of data. These data are mainly categorized into six distinct categories, which are: Ship operation data, Low-frequency data, high-frequency data, External data, General data, and Reference data (Jabary et al., 2022). However, for a scaled model within a controlled environment, these categories can be shortened into the following:

1. Operation data

This includes data about the planned runs, what are the operation profiles included within the run.

2. Low-frequency data

Which comprises data that are not frequently changing during the model run such as ship loading conditions, ship hydrostatics, and water temperature.

3. High-frequency data

Contrary to Low-frequency data, this includes raw sensor data captured for different parameters during the model operation. These parameters were described in detail in Chapter 4.

4. Reference data

This contains all information about the model and its components data sheets or reference values driven from trials. Additionally, the components operating diagrams and efficiencies.

The information objects mentioned are correlated to each other within the operating context. These relationships are represented in an overall entity-relationship model (ERM)

shown in Figure 7.1.

The ERM is a data model that is utilized to represent the relationship between different entities in the database. It serves also in database design. The model usually consists of three components. The first component is the entities that represent a real-world object. Each entity has its own attributes describing its properties and features which is considered the second component of the data model. The last component is the relationship among these entities. It is also possible to illustrate the data model graphically using what is known as an Entity-relationship diagram which provides a clear understanding of how the entities are correlated and eventually how the database should be structured (Chen, 1976).

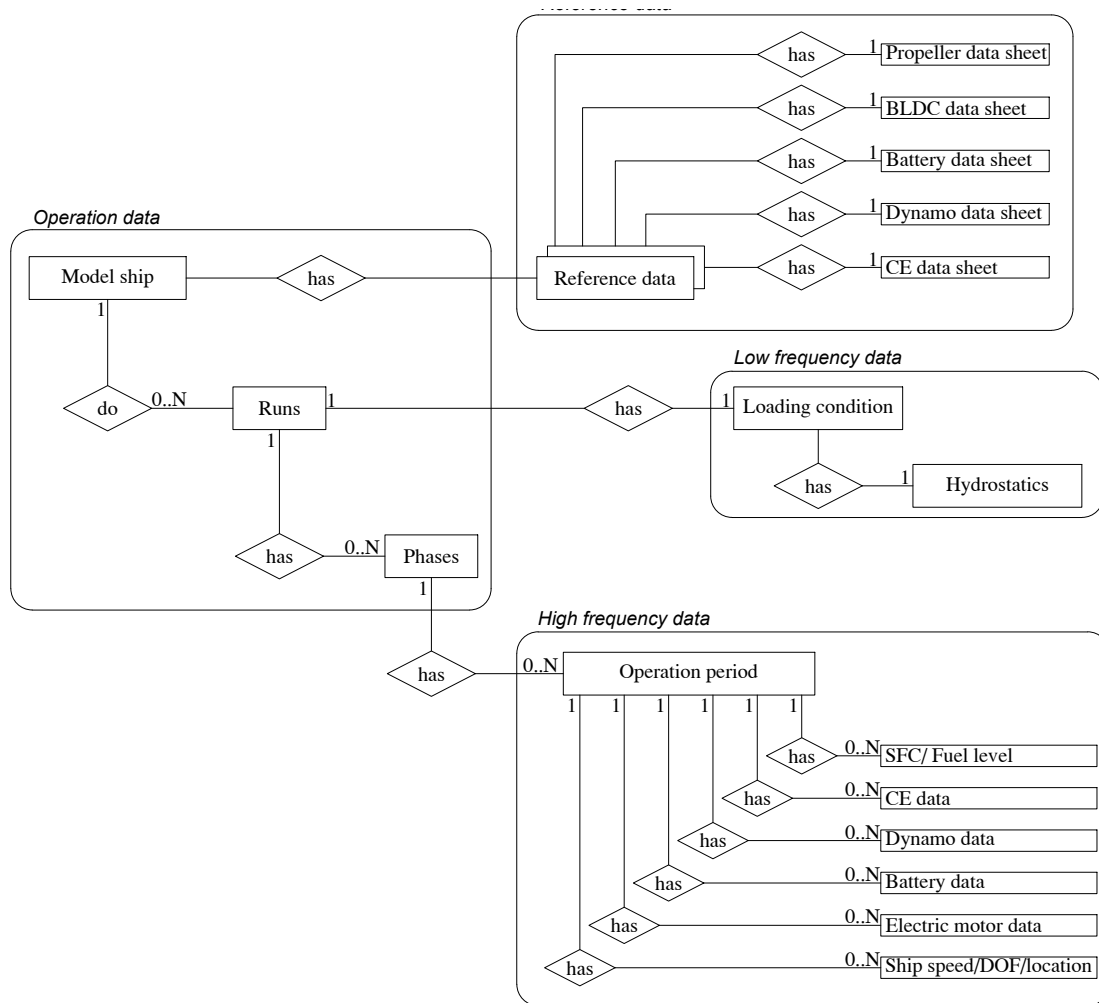


Figure 7.1: Overall data models ERM proposed diagram

A relationship between runs and the ship model is an example of how to interpret the notation with the relationship direction. In other words, the demonstrator would have (0..N) number of runs and the runs will be only associated with one ship model (not more than one or none). In general, the information objects at a lower level within that tree cannot exist without their associated higher-level information objects.

In the case of high-frequency recorded data, it is advantageous that all the data points

should be correlated to the same time step, ensuring proper synchronization. This synchronization is an essential requirement for performing meaningful data analysis. By having the data recorded with consistent time steps, it becomes feasible to include parameters of interest into the same plots, facilitating further analysis and exploration of relationships and patterns within the data (Jabary et al., 2022). It will also save the time needed to synchronize these parameters later in data preprocessing phase.

7.1 Data management system architecture

For the sake of efficient data analysis, several processes should be performed simultaneously and smoothly. Those processes are mainly data import, data storage/retrieval, and data processing. Jabary et al. (2022) presented a system that consists of 4 main components as follows:

1. **Information model:** In this process, the operational data are planned to be represented as information objects with descriptions of their relationships to each other - as described in Chapter 7. Software like pgModeler can be utilized for the formulation of this logical information model. It also can provide an output file format like Structured Query Language Data Definition Language (SQL DDL) that can be easily integrated into the database management system while creating the physical model (physical model in the context of information modeling means how the data will be stored and organized in a database management system). It also can provide the possibility to visualize the model via a web browser using HTML as an output file.
2. **Data storage and retrieval:** One possible solution for data storage and access is an open-source object-relational database system called PostgreSQL. The physical structure of the database is designed based on a relational model. This means that the data can be organized and retrieved in a way that is similar to how objects are used in programming.
3. **Data import:** Reference data as well as the operational data can be imported by using customized Python algorithms which can handle data with different formats such as SQLite, CSV and .dat.
4. **Data analysis:** Developed Python code can be used to access the stored and synchronized data for further analysis, but in order to have an efficient analysis, these data are subjected to pre-processing operations as will be explained in Chapter 8.

The previously explained components and process are visually represented in Figure 7.2.

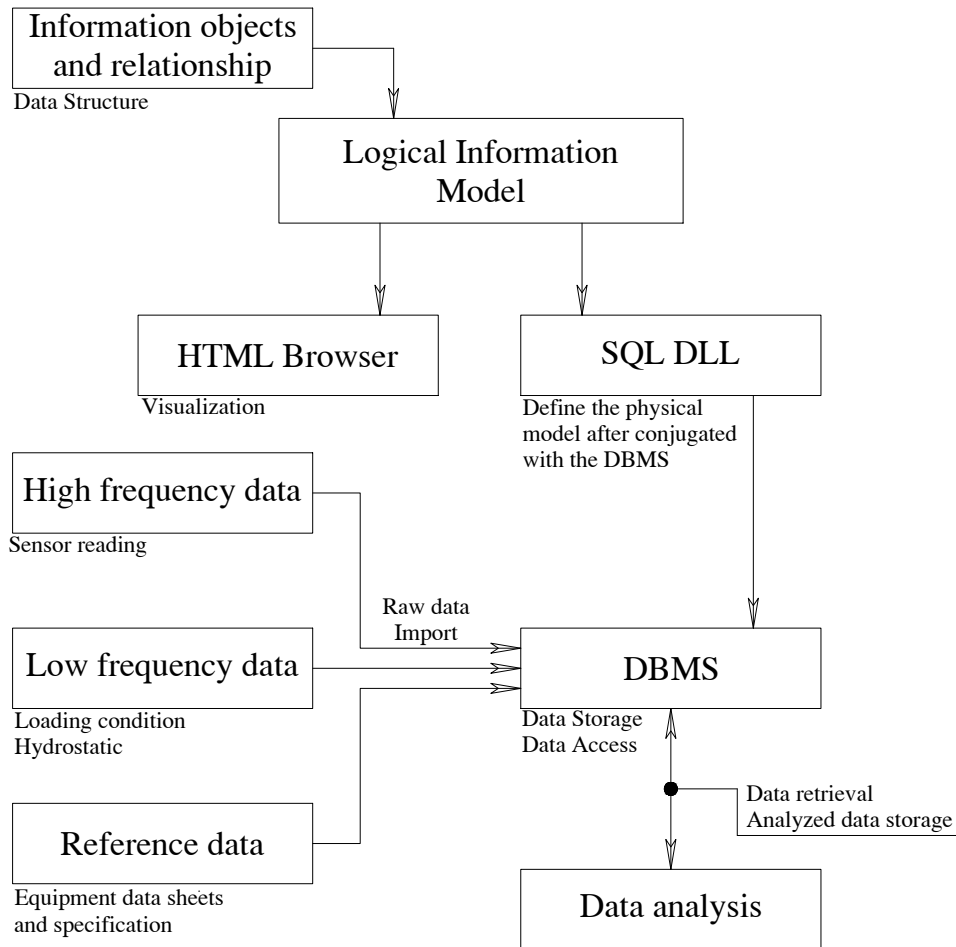


Figure 7.2: The proposed data management system architecture

Within this chapter, a comprehensive literature review of several existing data preprocessing methods has been undertaken. This involves elucidating their methodologies, benefits, and limitations. These diverse methods will subsequently be applied to the developed data preprocessing algorithms, subjecting their performance to real-world testing.

The gathered data are the key feature for a reliable evaluation of ship operation performance and successive DT implementation (Zhang et al., 2022). The ship operators can now obtain vast data representing different parameters within the ship's complex systems. This can be attributed to the rapid development of sensors and telemetry technology as well as the increasing complexity of modern ship systems (DMA, 2018).

The obtained raw data is preprocessed, then undergoes a correlation analysis to identify the interdependence among operational parameters, unveiling the influencing operational condition. Furthermore, these data are utilized for ship performance assessment when compared against the ship reference data.

The recent developments in fields like Information Technology, Data Science, and Machine Learning have created more opportunities for conducting an in-depth analysis of the gathered data which are attributed to complexity and vast size (Jabary et al., 2023b).

Jabary et al. (2023b) categorized the potential challenges while processing the data into two main groups:

1. Challenges concerning data form.

Data are captured from different sensors in different formats with different frequencies which will require customized codes (programs) to import and synchronize these data.

2. Challenges concerning data content.

Data gathered might have some weaknesses which can pose obstacles to the proper data analysis process. According to ISO (2017), these can be categorized as :

- a) Missing data which might occur due to sensor or telemetry module failure.
- b) Outlier data points that deviate significantly from the trend of other data points.

To ensure accurate and reliable data analysis, it is essential to synchronize the recorded data from various sources. Once the data is synchronized, it continues preprocessing to identify and eliminate any flaws or inconsistencies. This preprocessing stage aims to enhance the quality and integrity of the data, enabling more accurate analysis and interpretation.

With regard to the above-mentioned challenges, a data management system was developed to overcome any potential data flaws. The following sections will address these data-processing steps and methods employed.

8.1 Data Synchronising

In a scenario where data is collected from different sources (e.g., sensors) at various frequencies, with different temporal periods, it is crucial to synchronize the raw data. During this process, the data points from different sources are been aligned to a common time reference. This will enable meaningful comparison and accurate operational data correlation analysis.

8.1.1 Dynamic Time Warping (DTW)

Bellman and Kalaba (1959) introduced Dynamic Time Warping (DTW), and later in the 70s it was employed in many applications such as speech recognition (Myers et al., 1980), signature/handwriting matching (Tappert et al., 1990), and signal processing (Müller, 2007).

DTW is a method for measuring similarity between time series data. DTW can also handle data sets with varying lengths by allowing what is called "elastic" transformation (Senin, 2008a). In other words, it allows stretching or compression of the time axis to align similar data occurrence patterns even if the data sets have different time periods.

It should be mentioned that this time warping behavior is only done for the sake of correlation and comparison between the parameters. However, the original signal temporal length before warping is kept unchanged.

8.1.1.1 DTW algorithm implementation

The DTW algorithm implementation is explained in the following steps:

1. Consider two different signals denoted by (x) and (y) each one containing (N) and (M) number of entries. Both can be represented as $x_{1:N}$ and $y_{1:M}$. It is required to align these two signals.
2. Start to construct the cost matrix (**D**) which will tell which point from the signal (x) corresponds to the signal (y) and how much cost to align them.
3. The (**D**) is initialized in a way that the dimension of the (**D**) is (N+1) x (M+1). The first column ($\mathbf{D}_{i,0}$) and first row ($\mathbf{D}_{0,j}$) are filled with ∞ . But $\mathbf{D}_{0,0}$ is filled with zero as illustrated in Figure 8.1a.
4. Calculate the distance and the cost to align the first entry in (x) signal to the first entry in signal (y). The obtained result is filled ($\mathbf{D}_{1,1}$). The cost is calculated using the following equation

$$D_{i,j} = d(x_i, y_j) + \min \begin{cases} D_{i-1,j-1} & \text{(match)} \\ D_{i-1,j} & \text{(insertion)} \\ D_{i,j-1} & \text{(deletion)} \end{cases} \quad (8.1)$$

Where $d(x_i, y_j)$ is the absolute difference between x_i and y_j .

5. Iterate the process for each entry from signal (x) against all entries in signal (y).
6. Depending on the minimum values that are used to calculate the cost, the warping path is determined. The warping path is showing which points are corresponding to each

other from both signals with minimum cost to align as shown in Figure 8.1b.

7. The cost for alignment of both signals is found in cell $(\mathbf{D}_{N,M})$. In Figure 8.1b, the alignment cost is 2.0.
8. The entries that correspond to each other along the warp path are then plotted on the same plot.

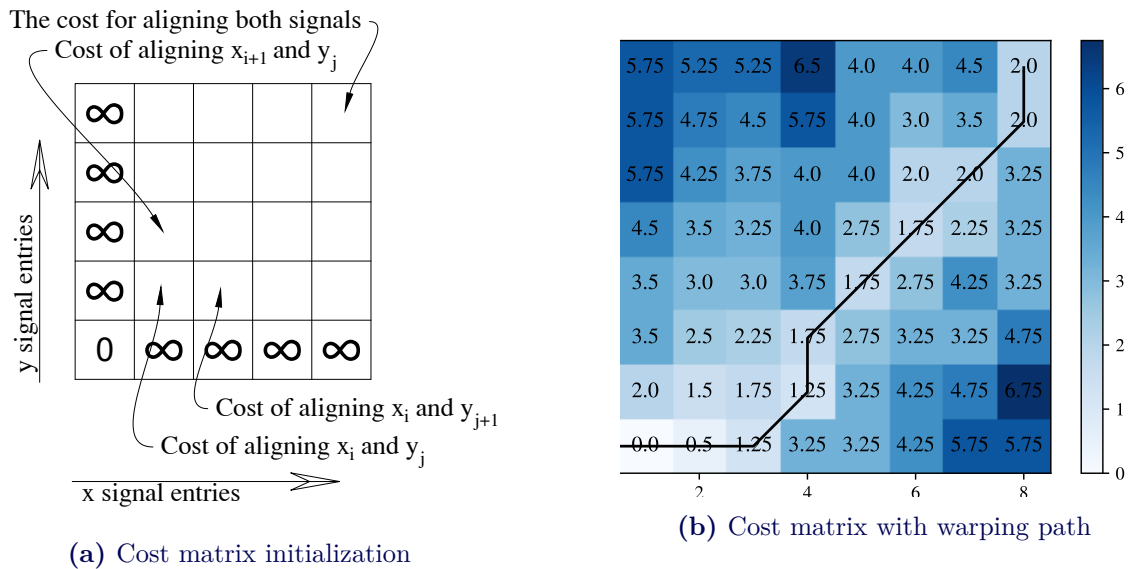


Figure 8.1: Demonstration of Dynamic Time Warping (DTW) cost matrix initialization (on left) and graphical representation of warping path (on right)

It should be mentioned that DTW at its core is computationally expensive especially when dealing with populated time series data sets. This is directly attributed to the cost matrix size that is directly influenced by the number of data points. Furthermore, it's important to consider that as it measures the distance between data points from each data set, it could yield misleading results when dealing with two data sets of varying dimensions.

8.1.2 Cross-correlation method

Another method that has been popular in synchronizing time series data is the cross-correlation method. This approach involves a straightforward procedure of sliding one series over the other and subsequently computing the correlation between the two series. The alignment of the two series will occur at the point where the maximum correlation is identified. On one hand, it is less computationally expensive, but on the other hand, it does not feature the time-warping ability. This makes its performances tied to data sets with the same temporal time.

8.1.2.1 Cross-correlation algorithm implementation

The cross-correlation is calculated according to Equation (8.2), where (n) is the number of data points in the series and (m) is the time offset between the two series. The lag value $C_{xy}[m]$ will be iterating between the minimum and maximum possible lag values (Bourke,

1996).

$$C_{xy}[m] = \sum_n x[n] \cdot y[n + m] \quad (8.2)$$

For each lag value, the correlation coefficient is calculated according to Equation (8.3). Generally, it is a scalar value that varies between 1 to -1. The closer this value to 1 or -1 means a strong correlation between both series and closer to zero means a weak correlation.

$$r = \frac{\sum (x_i - \bar{x})(y_i - \bar{y})}{\sqrt{\sum (x_i - \bar{x})^2 \sum (y_i - \bar{y})^2}} \quad (8.3)$$

8.2 Data compilation

In the case of dealing with data sets that are sharing the same time steps but one data set has a different frequency, ISO 19030 has recommended two methods to address two possible scenarios.

- **Compilation high to low-frequency data** is done by averaging the high-frequency data over a relevant time interval between two successive low-frequency records.
- **Compilation low to high-frequency data** is done by duplicating the low-frequency data over relevant time with time steps of the high-frequency data.

ISO 19030 proposed Equation (8.4) to perform high to low-frequency data compilation and Equation (8.5) for the opposite case.

$$a_{i+f-1} = \frac{1}{n_k} \sum_1^{n_k} m_k \quad \text{for } i < k \leq i + f^{-1} \quad (8.4)$$

Where a_{i+f-1} is the average high-frequency value over time step (i) and time step (f^{-1}). (f) is the high data frequency. n_k is the number of high-frequency measures between two successive low-frequency measures and m_k is their summation. (k) is the low-frequency data time step.

For low to high-frequency compilation, ISO 19030 recommends that the values of the low-frequency measures be duplicated over relevant time intervals. The low-frequency value m_k at a time interval k is to be duplicated to the values a_i with time stamps i from the high-frequency measures. Where i lies between k and $k - t^{-1}$.

$$a_i = m_k \text{ for all } i \text{ in } k - t^{-1} < i \leq k \quad (8.5)$$

8.3 Data cleaning

Not all data captured by sensors are meaningful, so it is essential to distinguish between both raw and net data (Ícaro Aragão Fonseca and Gaspar, 2021). Therefore the raw data should undergo some cleaning processes to extract more meaningful data (eg. net data) from it. In this section, different data filtering techniques will be discussed. These filtering methods will be utilized to identify and eliminate any potential data anomaly. These potential flaws

together with some proposed methods to handle them are discussed in the following subsections.

8.3.1 Data denoising

Salgado et al. (2016) mentioned the difference between noise and outliers. While outliers might be of use if they are presenting a truly abnormal behavior in the system. However, noise is always presenting value errors or mislabeling that should be cleaned in a process known as signal denoising.

Liu et al. (2020) presented that cleansing noisy signal data is the most essential preparatory step in data analysis. Data sets might have superimposed noise and outliers and the presence of the noise is an obstacle to the outliers detection method to have true detections. He also added that utilizing the outliers removal methods to denoise the data set is not a proper approach.

8.3.1.1 Kalman filter

The Kalman filter, named after its creator Rudolf E. Kalman, is a recursive algorithm designed to estimate the evolving state of a system in the presence of noise. This system, which is typically dynamic, can be represented by a set of mathematical equations that relate the observable measurements and the underlying state (Welch, 2020). The working principle of the Kalman filter can be divided into two key steps: prediction and update. These steps are briefly explained below.

1. **The prediction step:** This step provides us with an estimation of the system's next state with regard to the current state. The uncertainty of this estimate is also predicted which is represented by a covariance matrix.
2. **The update step:** This step involves using the new measures to correct the previous estimations (values and uncertainty). Then the Kalman gain is measured which represents the ratio between the predicted and measured certainty. Then, the initial estimate and error covariance is updated.

These two steps are then iterated improving the accuracy of the estimated states, therefore smoothing out the signal noise. The working principle of the Kalman filter is summarized in Figure 8.2.

In the Kalman filtering algorithm, there are manually input parameters that highly influence the filtering performance. These parameters are measurement noise variance and process noise variance) denoted by R_n and Q_n respectively

The first parameter (Measurement noise variance (R_n)) is representing the uncertainty associated with the measurements. A higher value means a more noisy and less reliable signal. So the Kalman filter will put less weight on the measurements and rely more on its previous state estimate.

The other parameter (Process noise variance (Q_n)) represents the uncertainty associated with the process model itself. A higher value means less precise for the model. The Kalman filter will then allow its state estimate to change more freely from one step to the next.

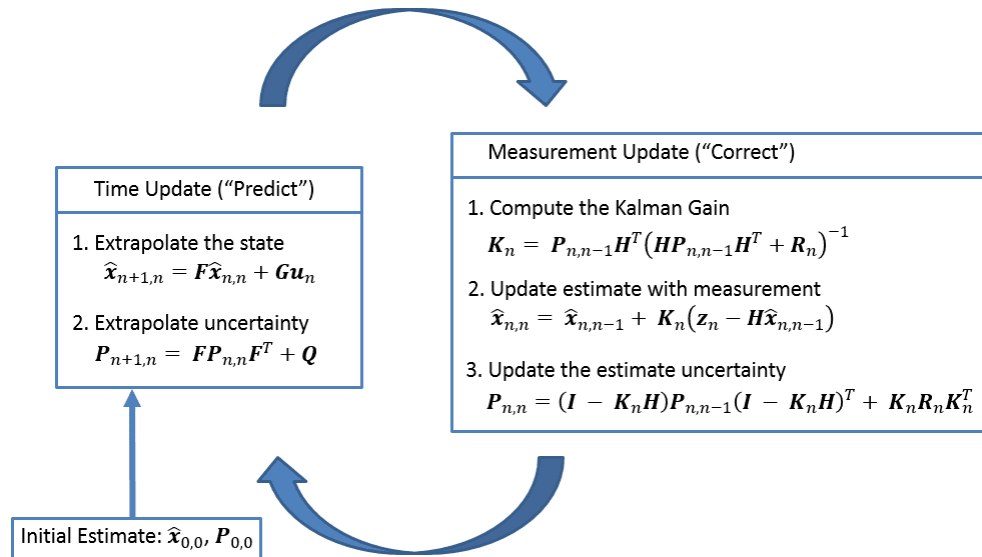


Figure 8.2: Summarized Kalman filter principle and formation (Becker, 2023)

8.3.1.2 Low-Pass Filtering

As mentioned by Jiao et al. (2015), the low-pass filtering concept is about cutting off signals with respect to their values. A common method to determine which signals are required to be eliminated is by filtering out signals that have a frequency higher than a certain value. For a timer series data set or signal, it will be necessary to transform it from time to frequency domain. One method to do it is to use Fast Fourier transform (FFT). The detailed steps is to be as follows :

1. Using the FFT to switch the signal from time to frequency domain.
2. Calculate the frequency for each entry.
3. Replace those signals with frequencies higher than a certain threshold value with zero.
4. Inverse the FFT transformation to convert back the signal to the time domain again.

Similar to the R_n and Q_n parameters in the Kalman filter, the determination of the minimum frequency threshold necessitates manual definition, which may involve some trial and error to identify an appropriate value.

8.3.2 Data Outliers

Data outliers are described as those data points which are inconsistent with the remaining data set (Hodge and Austin, 2004). The existence of these outliers in the data set will cause misleading analysis results (Hasan, 2019). These outlines may occur due to human error or instrumental failure. However, within this thesis, the data is reported mainly from sensors. These sensors are prone to some potential flaws such as failure, malfunction, or rapid attrition. As a result, the sensor may occasionally produce anomalous or erroneous readings, commonly referred to as outliers (Gaddam et al., 2020).

8.3.3 Outliers Visualisation

Before applying filtering methods to eliminate the data outliers, it is beneficial to have an insight into how these outliers are distributed across the data set. There are several that serve as tools to detect the potential outlier. Some of these methods are discussed below

8.3.3.1 Scatter plot

A scatter plot can be utilized to visualize a relationship between two variables. It is a useful tool to have a quick overview of the correlation between the variables, outliers, data patterns, and distribution (Kaliyaperumal and Kuppusamy, 2015). However, with intense data sets, it may be challenging to detect the outliers since a scatter plot does not provide a standard way for highlighting the outliers. Another drawback of the scatter plot is that it does not provide any statics summary about the data set (eg. mean, median) or measures of dispersion (e.g., range, interquartile range). To overcome the mentioned drawbacks, the box plot is introduced.

8.3.3.2 The Box Plot

The box plot, also known as the Box-and-Whisker is a graphical method to visualize the data point distribution and summary statics (Williamson et al., 1989). The box plot consists of the following elements and is illustrated in Figure 8.3.

1. Box

The box contains 50% of the data. the left boundary is 25th percentile (Q1) and the right boundary 75th percentile (Q3). The box length is representing the data spread within this range.

2. Median

The median or middle quartile is represented by a vertical line inside the box splitting it in half.

3. Whiskers

The whiskers are horizontal lines extending from the box on both sides representing the data points located outside the Interquartile Range (IQR) (eg. the other 50% of the data). Both ends of the whiskers are representing minima and maxima values. the length of these whiskers is governed by $Maxima = Q3 + 1.5 \times IQR$ and $Minima = Q1 - 1.5 \times IQR$

4. Outliers

Outliers are the individual points located outside the whiskers.

8.3.3.3 Kernel density estimation plot

Kernel density estimation (KDE) estimates the probability density function which is driven by smoothing a histogram for the data set. It is another tool commonly used in data analysis to estimate the underlying probability distribution of a data set (Lang et al., 2022). The process of KDE includes the following steps:

1. Choose a kernel function: Common choices include the Gaussian (normal) distribution.

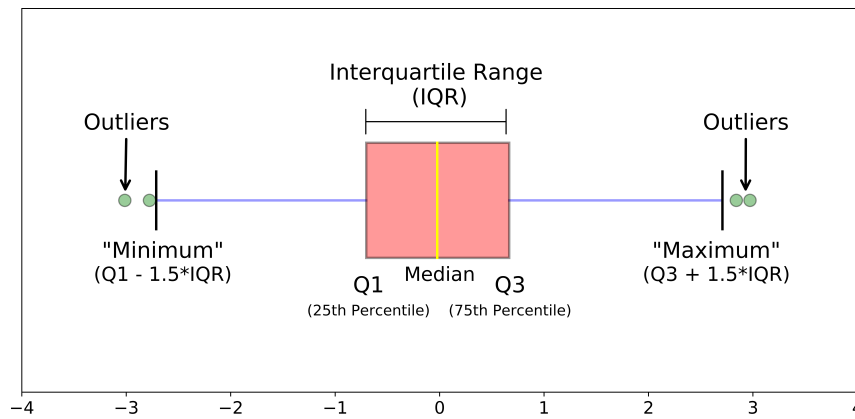


Figure 8.3: Box plot example graph illustrating different component of the plot (Azevedo, 2022)

2. Determine the bandwidth: This will control the width of the kernel and the smoothness of the estimated function.
3. Placing a kernel at each data point in a way that the center of the kernel is located at each data point.
4. Summing up the kernel to obtain the smooth estimate of the probability density function (PDF).

After obtaining the estimated PDE, the user should define the threshold value that defines the region of low density. Points located below this limit are considered as potential outliers. The threshold is determined manually based on the nature of the domain data.

For the sake of a better understanding of these visualization methods, Python code was used to generate a simulated data set resembling sensor readings. Some randomly generated outliers were included within this data set to give a more comprehensive representation of a real-world scenario. These methods were illustrated in Figure 8.4.

In the top graph, the scatter plot provided a quick glance at the data correlation, pattern, and distribution of outliers with no ability to contrast these outliers. In the second plot, the outliers data were clearly identified (Those points located outside the Whisker). The third graph is representing the smoothed PDF where the outliers can be identified by those low-density regimes at both curve ends. However, in the Kernel density estimation plot, the decision of a data point to be an outlier is dependent on the manually defined threshold.

8.3.4 Outliers Removal

In order to conduct an effective data analysis, it is necessary to clean the data set from any potential outliers. Thanks to ongoing development in data science, there are now several outliers removal methods available that can be utilized for this task. ISO 19030 gives a suggestion of one statistical method that can be utilized for outliers removal.

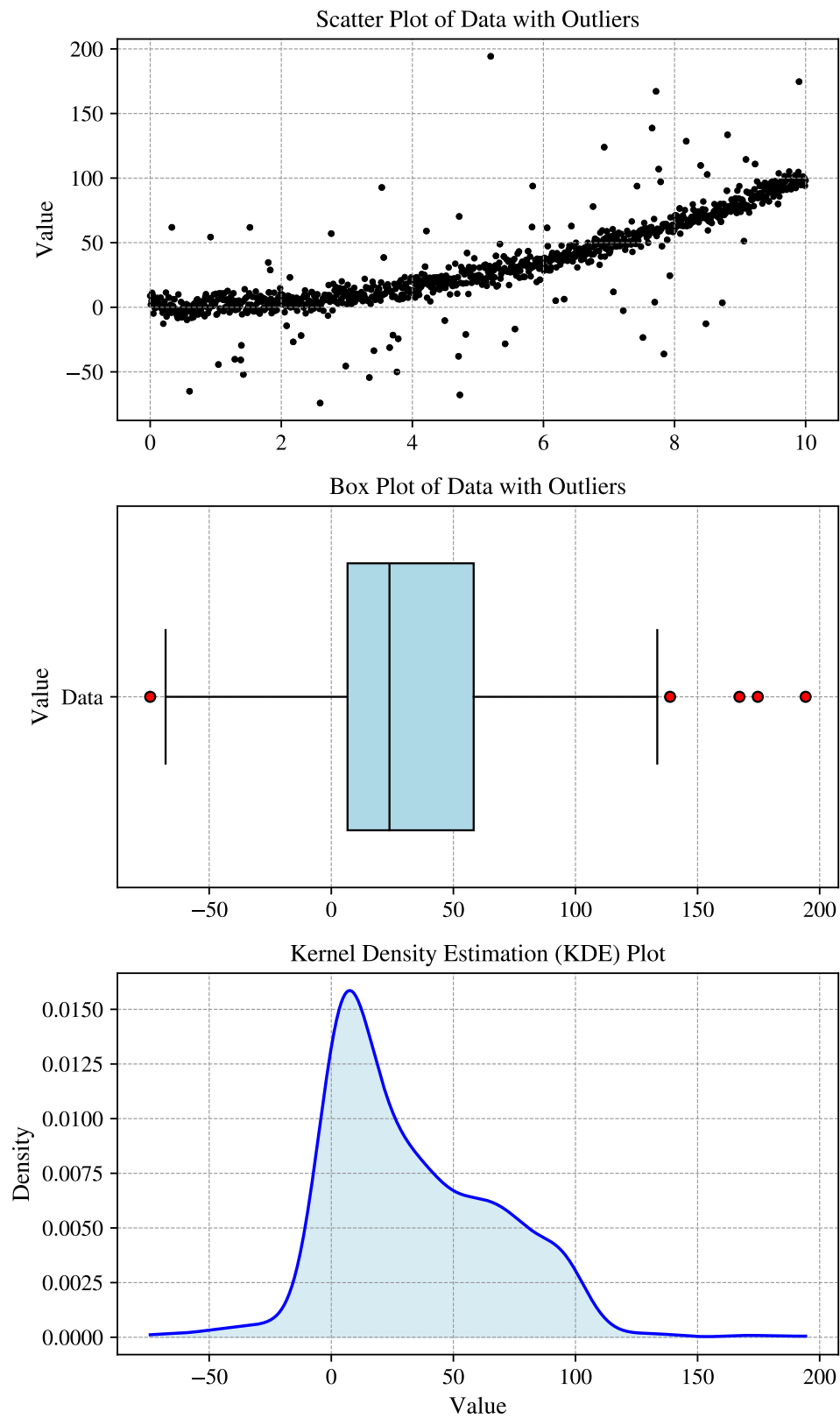


Figure 8.4: Exemplary comparison between the outliers visualization methods (scatter plot, box plot, and kernel density plot)

8.3.4.1 Chauvenet's Criterion

The Chauvenet's Criterion is a statistical outliers removal method (Lin and Sherman, 2007) which is also suggested by ISO 19030 standard. It is a method that is used to identify and remove outliers from the data set. From a statics point of view, outliers are those data points that significantly deviate from the rest of the data set. Based on this definition, Chauvenet's Criterion provides a mathematical approach to determining how often each data point occurs with respect to the data point distribution.

The criterion is applied through the following steps:

1. The data set is divided into equally spaced and non-overlapping blocks (the reason behind the subdivision will be discussed later).
2. The mean is calculated for each block using the following formulas:

For data not measured in angles

$$\text{Mean} = \mu = \frac{1}{N} \sum_i^N d_i \quad (8.6)$$

For data measured in angles

$$\text{Mean} = \mu = \text{atan2} \left(\frac{1}{N} \sum_{i=1}^N \sin(d_i), \frac{1}{N} \sum_{i=1}^N \cos(d_i) \right) \quad (8.7)$$

3. Calculate the standard error of the mean using the following formula:

For data not measured in angles

$$\Delta_i = |(d_i - \mu)| \quad (8.8)$$

For data measured in angles

$$\Delta_i = \begin{cases} 360 \text{ deg} - r_i & \text{if } r_i = \text{mod} (|(d_i - \mu)|, 360) > 180 \text{ deg} \\ r_i & \text{otherwise} \end{cases} \quad (8.9)$$

4. Calculate the standard error for each block using the following formulas:

$$\sigma = \sqrt{\frac{1}{N} \sum_i^N \Delta_i^2} \quad (8.10)$$

5. Calculate the probability of occurrence for any value using the following formula:

$$P(d_i) = \text{erfc} \left(\frac{\Delta_i}{\sigma \cdot \sqrt{2}} \right) \quad (8.11)$$

6. A data point is considered an outlier if the following criteria is achieved:

$$P(d_i) \cdot N < 0,5 \quad (8.12)$$

The whole block is considered invalid if one data point does not meet Chauvenet's Criterion. According to ISO 19030, this criterion is extended to other measured parameters that share the same time step. In other words, not only the corresponding data block is marked as invalid when a data point does not meet Chauvenet's Criterion but also other blocks related to other parameters that have the same time window are also marked as invalid. Figure 8.5 demonstrate the graphical representation of Chauvenet's criterion.

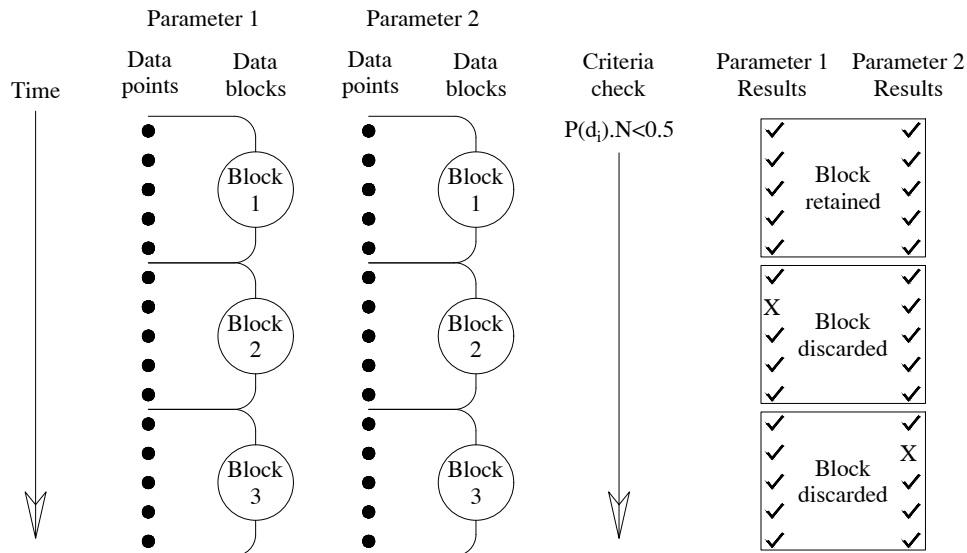


Figure 8.5: Chauvenet's criterion graphical representation

Although its usefulness, Chauvenet's Criterion has the drawback of being computationally expensive. This is because of the necessity to iterate the calculation process for all available data points within the data block as shown in Equation (8.8) afterward the calculation should be iterated across all data blocks as shown in Equation (8.10). Therefore, the method presented below can be utilized with less computational effort.

8.3.4.2 Interquartile Range filter

The IQR filter has the same methodology followed in the box plot method described before but with further steps to crop these visualized outliers. This method does not require any iteration process as done in the previous method. Therefore it is commonly used with big data sets to save computational efforts.

8.3.4.3 Z-Score and Modified Z-Score

Z-Score is another statistical method that is commonly used to describe the correlation of a single value to a group of values (Yaro et al., 2023). The Z-Score is calculated using Equation (8.13).

$$Z_{score} = \frac{x_i - \mu}{\sigma} \quad (8.13)$$

Where μ and σ are the mean and standard deviation values of the time series respectively. A certain point is considered an outlier if its Z-score exceeds a certain value of a predefined threshold. Yaro et al. (2023) mentioned that the common value of this threshold is ± 3 .

As shown in the Equation (8.13), the Z-Score is dependent on the mean value of the targeted time series. This makes the results highly influenced by the existence and the values of the outliers since this can skew the mean value of the data set. Therefore, the mean value will have a weak representation of the data set.

The Modified Z-Score is a more robust method than the conventional Z-score method. The Z-Score in this method is calculated using the median value of the time series as shown in equations Equation (8.14) and Equation (8.15) (201, 2014). Similarly to the Z-Score method, the point is considered an outlier when it exceeds a threshold of ± 3.5 (Iglewicz and Hoaglin, 1993).

$$M_i = \frac{0.6745 (x_i - \tilde{x})}{MAD} \quad (8.14)$$

$$MAD = \text{median}_i \{|x_i - \tilde{x}|\} \quad (8.15)$$

These outliers detection methods described are all suitable to be applied to univariate time series data sets. However, each method employs a different technique to identify these outliers which will result in a different quantity of outliers per each method.

Blázquez-García et al. (2021) highlighted that if the detection method was applied to the entire time series, then only global outliers will be detected. However, if the time series was divided into what is called a time window (or blocks according to ISO 19030), the outliers detected will be local outliers since they are been compared with their neighborhood. They added also that all the global outliers are considered local outliers but not the opposite.

In simpler words (just an example), assume that the model run duration was 1 hour, and the model had a constant speed varying between 2 to 3 meters per second during most of the time. But for any reason, it was decided to test how fast the model can go with at full RPM value and it was recorded to be 7 meters per second and the model kept this speed for only 3 minutes for safety reasons. In data analysis of the speed time series, there is a high potential that the data points in the regime of 7 m per second speed will be detected as an outlier although it was a real case that happened intentionally. but this will only happen if the entire data set was examined for outliers as one part. Alternatively, if the time series was divided into time blocks, this high-speed region will be considered as part of the study, and only global outliers will be detected and removed.

8.4 Missing data

Another potential issue with sensor-measured data is missing data within the data set. Missing data can arise due to various reasons, such as sensor malfunctions, communication errors, power failures, or simply the inherent limitations of the sensing technology.

Another source of these missing data - as mentioned before - is the fingerprint of the deleted outliers from the data set. This usually happens when the outlier deletion method replaces the outlier with a NaN in order to preserve the time step.

Techniques for overcoming the missing data issue are mainly categorized into two main

categories (Agarwal, 2013). One strategy is to simply ignore these missing data, the other one is to estimate these missing data based on available data imputation methods.

8.4.0.1 List or Pairwise deletion method

- **The listwise deletion** method (known also as complete case analysis) is the simplest method to handle the missing data. It basically omits all the records that have at least one missing data.
- **The pairwise deletion** method (known also as available case analysis) is not based on deleting the whole record, it is based on only deleting those missing entries corresponding the parameters of our interest. This method has the advantage of keeping the maximum possible number of records within the data set.

Figure 8.6 provides a straightforward comparison of various deletion methods as they were employed in an illustrative scenario. On one hand, in the case of the listwise deletion method, the data set size might be significantly reduced no matter which parameters will be analyzed. It can be noted that the RPM parameter has lost two valid records just because it is corresponds to empty records from FOC and speed.

On the other hand, in the case of pairwise deletion, the data set size is well preserved depending on which parameters are chosen for analysis. For example, if the intention to analysis time with the speed, only those missing value from the time and the speed parameters will be deleted as shown in case 1 analysis. Another example if the intention is to study the time and the RPM as shown in Case 2, the data set preserved its full size since these two parameters have full entries.

Full data set			
Time	Speed	RPM	FOC
T 1	--	R 1	F 1
T 2	S 2	R 2	F 2
T 3	S 3	R 3	--
T 4	S 4	R 4	F 4

Listwise deletion				Pairwise deletion																					
<table border="1" style="width: 100%; border-collapse: collapse;"> <thead> <tr> <th>Time</th> <th>Speed</th> <th>RPM</th> <th>FOC</th> </tr> </thead> <tbody> <tr> <td>T 2</td> <td>S 2</td> <td>R 2</td> <td>F 2</td> </tr> <tr> <td>T 4</td> <td>S 4</td> <td>R 4</td> <td>F 4</td> </tr> </tbody> </table>				Time	Speed	RPM	FOC	T 2	S 2	R 2	F 2	T 4	S 4	R 4	F 4	Case 1		Case 2							
Time	Speed	RPM	FOC																						
T 2	S 2	R 2	F 2																						
T 4	S 4	R 4	F 4																						
<table border="1" style="width: 100%; border-collapse: collapse;"> <thead> <tr> <th>Time</th> <th>Speed</th> </tr> </thead> <tbody> <tr> <td>T 2</td> <td>S 2</td> </tr> <tr> <td>T 3</td> <td>S 3</td> </tr> <tr> <td>T 4</td> <td>S 4</td> </tr> <tr> <td> </td> <td> </td> </tr> </tbody> </table>				Time	Speed	T 2	S 2	T 3	S 3	T 4	S 4			<table border="1" style="width: 100%; border-collapse: collapse;"> <thead> <tr> <th>Time</th> <th>RPM</th> </tr> </thead> <tbody> <tr> <td>T 1</td> <td>R 1</td> </tr> <tr> <td>T 2</td> <td>R 2</td> </tr> <tr> <td>T 3</td> <td>R 3</td> </tr> <tr> <td>T 4</td> <td>R 4</td> </tr> </tbody> </table>		Time	RPM	T 1	R 1	T 2	R 2	T 3	R 3	T 4	R 4
Time	Speed																								
T 2	S 2																								
T 3	S 3																								
T 4	S 4																								
Time	RPM																								
T 1	R 1																								
T 2	R 2																								
T 3	R 3																								
T 4	R 4																								

Figure 8.6: Comparison between listwise and pairwise deletion methods

These deletion methods can possibly decrease the data set size which will result in reducing the statistical power and increasing the standard error (Jadhav et al., 2019). According to Raaijmakers (1999), the statistical power is reduced up to 90% when 30% of the observations

are missing. Therefore, they are only appropriate to use when the amount of missing data is relatively small in comparison with the data set size. These methods are also only valid in case of the missing data occurrence is random.

8.4.0.2 Data imputation

The data imputation method is another way to handle missing data within the data set without causing a data set size decrease. Basically, the imputation methods are estimating the missing values based on the available data.

Many methods are available for data imputation. However, three commonly used methods will be reviewed in this work.

- **Mean imputation:** it is a method where the missing values are directly replaced with the mean value of the data set. Although its simplicity, this imputation process can result in a change in the shape of the distribution. One noticeable effect is a decrease in the standard deviation when comparing it before and after imputation. The greater the number of missing values, the more pronounced the shrinkage in the standard deviation becomes.

To enhance the imputation method, a slight improvement can be achieved by stratifying the data into subgroups. This approach divides the data set into smaller subsets based on relevant characteristics or variables. By imputing missing values within each subgroup separately, the imputation process can better reflect the characteristics of the specific subgroups, potentially leading to more accurate and representative results (Jadhav et al., 2019).

- **Regression Imputation:** It is a method for handling missing data by using regression models to predict the missing values based on the relationships between variables in the data set. Regression can be assumed linearly for the sake of simplicity, However, this method still has an advantage over the mean imputation method in that the data distribution is preserved to some extent.
- **kNN Imputation:** K-nearest neighbors (kNN) imputation is a method used to fill in missing values in a data set based on information from similar or "nearest" data points. The idea behind kNN imputation is that observations that are close to each other are likely to have similar values. The data set is used as training data. This method is utilizing the whole data pattern by considering similarities between observations.

The continuous development of fields like statistics and data analysis has led to various imputation methods based on different techniques. However, it is important to note that there is no universally superior imputation method that can be universally applied to all recorded parameters.

Therefore, it is necessary to establish a clear method to evaluate the results after data imputation. One method for evaluation is to compare the data set after imputation with a similar data set from another source (eg. manually reported data, another sensor, or simulation results).

The imputed results can also be graphically visualized with the raw data where any bias

or abnormal values can be detected visually. Other plotting techniques such as histograms and density plots can provide a better insight into the data distribution.

8.5 Data down-sampling

The data compiling concept can be also utilized for what is called data down-sampling. Data down-sampling is a common method to compress time-series data sets via mathematical modeling (Steinarsson, 2013). This will help not only to enhance the data visualization, but also reduce the computational effort needed to process these data afterward (Donckt et al., 2023). This technique can be effectively employed with densely populated time series data sets in situations where the measured data frequency is sufficiently high where there is no significant changes occur between each entry. It also contribute to a certain degree to mitigate any potential data noise.

8.6 Cross-verification of data

Data checks after some pre-processing steps are also highly needed intermediate processes to evaluate the applied method's efficiency individually. Some pre-processing methods (such as the Kalman filter) have manually defined case-wise variables that lead to different results. Therefore, post-check processes will be the key to evaluating how far or close the result processed data is from the original data. These checks also are utilized to evaluate the outliers removal and data imputation methods.

Cross-correlation of the data set after each process is one of the possible post-checks that can be employed. This involved checking the correlation between the processed data sets before and after processing. This will give an insight if the pre-processing steps are resulting in satisfactory results or not.

Another strong method is to correlate the processed results against the same parameter results that were measured from another calibrated/higher accuracy source.

In the context of RC model, the throttle input can be related to the model speed. This is done by running various speed tests and relating the throttle value to the model speed. Therefore, these speed values related to known throttle values are to be stored in the system as what is called "Desire speed". Then, when the data is captured during the model run, both desired and actual speeds will be reported. Then the desired speed data will be utilized as a guide when evaluating the pre-processed applied on the actual speed data.

Jabary et al. (2023b) recommended three different methods to measure the correlation between. Each method is showing different dependencies between the data sets. These methods are briefly described below :

1. Pearson's correlation: It is a correlation method that simply measures the linear correlation between two variables. It is coefficient varies between $[-1,1]$. If the coefficient is equal to -1 or 1, this means that the two matrices lie on the same line (Sedgwick, 2012).
2. Spearman's rank correlation: It is a correlation method that captures the monotonic

relationship between two variables. Its correlation coefficient also varies between $[-1,1]$. If the two compared variables are increasing together, then the correlation coefficient will equal $+1$. If the first variable is decreasing while the second parameter is increasing then the correlation coefficient will be -1 (Sedgwick, 2014).

3. **Distance correlation:** It is a method that measures both linear and nonlinear correlation between two variables. The correlation coefficient varies between $[0,1]$. Where "0" indicates independent matrices and a value of "1" indicates equivalence Davis et al. (2018).

8.7 Data processing pipeline

After introducing the different data processing mechanisms, it was necessary to apply them in a proper sequence supported by reasonable justifications. The data processing pipeline is decomposed in the following proposed sequence.

1. **Data synchronization:** For time series data sets, synchronizing harvested data is the most prior process to do. The reason behind this is any other later process will present inappropriate results if there are potential lag between the data sets. This lag will influence the data compilation process since the data will be either averaged or duplicated in the wrong time step. In addition, in processing multivariate outliers, having a consistent outliers behavior between different data sets will provide insight into these outliers' nature (ie. to detect multivariate outlier points, data sets should be aligned to the same time axis).
2. **Data compilation:** unifying data frequency is proposed to be the second step. The reason behind this is to have a consistent data size which will have a positive influence on removing unwanted values such as Zeros and NaNs afterward. By standardizing the data frequency, the same number of entries will be deleted from all data sets and eventually will result in having equally sized data sets which will streamline any further analysis. Furthermore, data compilation from high to low frequency provides an additional advantage by potentially reducing the signal noise.
3. **Data denoising:** The reason behind choosing to remove the noisy effect before detecting the potential outliers is that most outliers detection methods discussed before are influenced by the data set statistical properties such as mean, median, and data distribution. Therefore, the presence of these noises will have a direct impact on these values and will lead to an efficient outliers removal process.
4. **Outliers detection method:** After eliminating the randomness behavior caused by the noise from the data set. It is time to further clean the data set from any potential outliers. In this process, outliers values will not be deleted completely from the data set, they will be simply replaced by NaN to pave the way to be imputed in the next step.
5. **Data imputation:** In this step any potential missing data will be imputed using any of the suggested imputation methods mentioned before.
6. **Data downsampling:** The reason behind placing it at the end of the data processing

pipeline is the fact that it should be only applied in the extreme need case only when the data set is requiring high computational resources to be analyzed. This process might lead to unintentionally fading some important features, so it is highly recommended to perform checks before and after employing it.

This proposed pipeline is not strict and should be flexible depending on the nature of the harvested data. For instance, if the gathered data inherently suffer from wide data gaps, then it would be plausible to apply the data imputation at an earlier step.

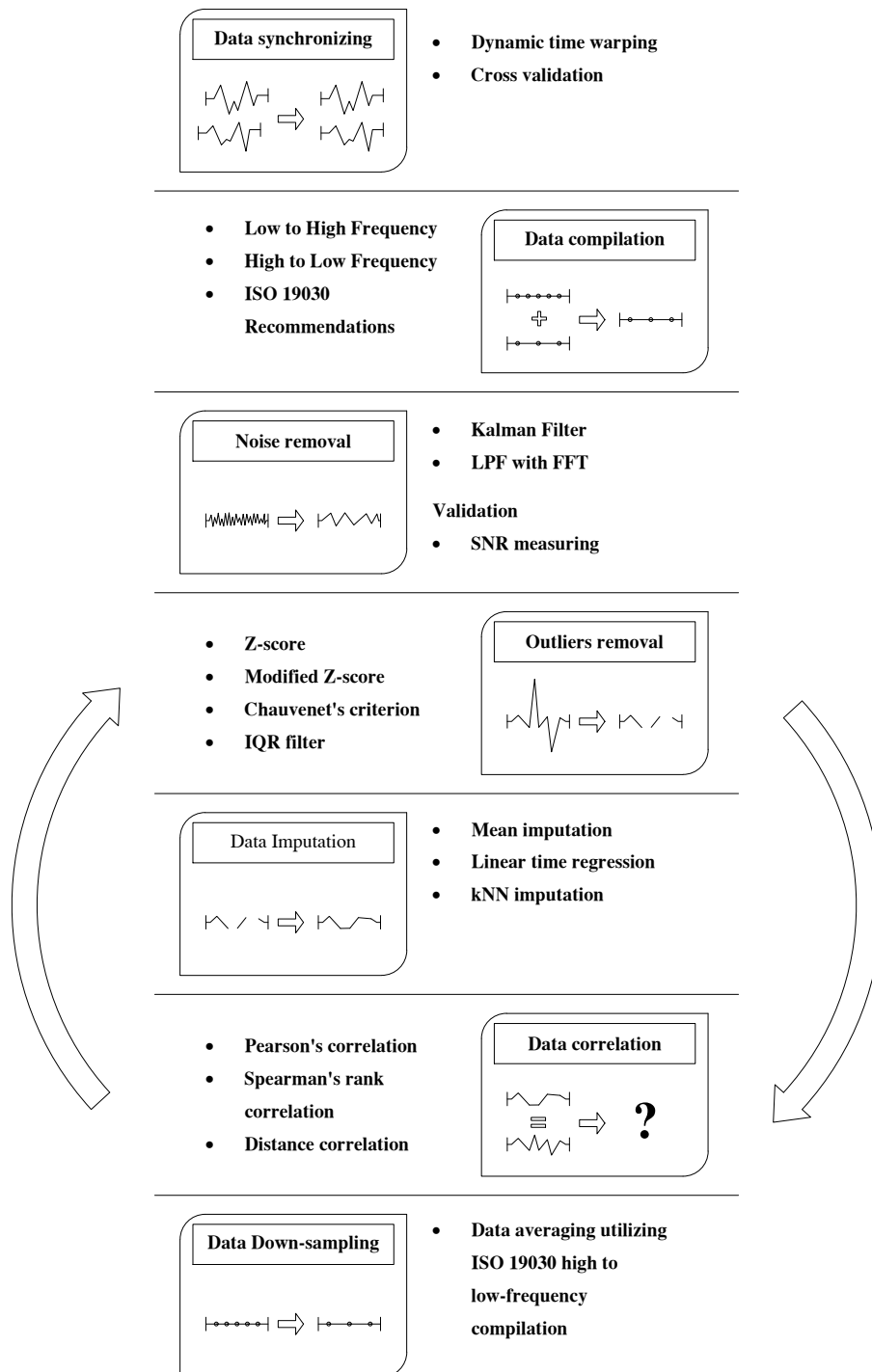


Figure 8.7: Graphical representation of the proposed data pre-processing pipeline

This page intentionally left blank.

9

Results

This chapter presents and discusses the outcomes of the thesis. Firstly, it covers the status of the model's equipment and the employed power configuration. Secondly, it delves into the application of the developed data pre-processing algorithms, which were utilized to enhance the quality of the data collected by the model's onboard system. Moreover, the chapter involves the derivation of parameter formulations alongside their reflection on naval architecture aspects.

9.1 Final Equipping and Configuration of the Ship Model

The model was equipped with the essential components that can provide valuable operational data to be analyzed. The decision was made to employ batteries as the primary power source for all components, as it remains a valid power source with parameters of interest for analysis. The equipment employed in the model is shown in the shortened list in Table 9.1. Additionally, a simplified version of the model diagram is shown in Figure 9.1 for the actual components in the current model version.

Table 9.1: The list of the final components installed in the model

No.	Item	Description	Quantity
1	Hull	GFRP 16.61:1 scaled-down model	1
2	Propeller	5 blades, 65 mm diameter, 6.5 mm pitch	2
3	Battery	4S LiPo 5000 mAh battery	2
4	Rudder	67x45mm	2
5	Autopilot	Pixhawk 6	1
6	Rudder Servo	Torcster Mini Servo NR-85 MG Digital 20g	2
7	Power distribution board	Pixhawk PX4 Mini PM06 V2	1
8	ESC	EzRun MAX10 G2, 140A	2
9	Brushless DC electric motor	MAX Marine P359 350KV	2
10	Gearbox	for the brushless motors, reducer ratio 2:1	2
11	Telemetry module	FrSky	1
12	Receiver	ARCHER-R8 Pro Receiver	1
13	GPS module	Holybro M9N GPS	1

With these components, the model is capable to be remotely driven through a considerable distance. Furthermore, the inclusion of the Pixhawk 6 Autopilot and the GPS module enables the collection of valuable operational data.

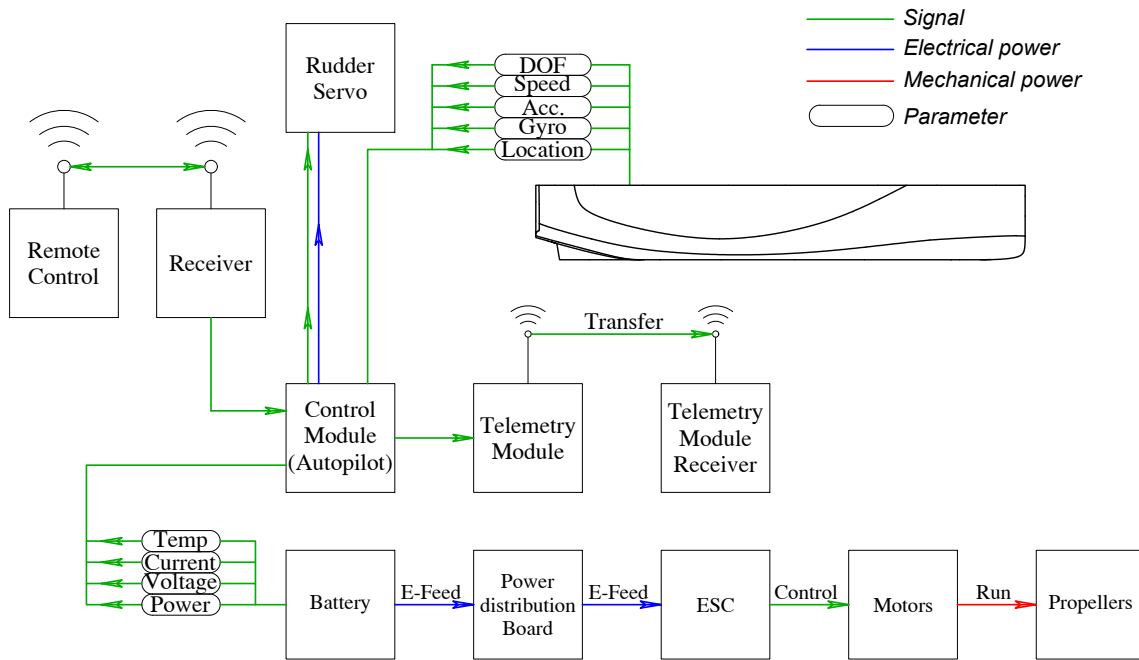


Figure 9.1: Simplified diagram for the onboard components in the final model state

Additional solid weights as shown in Figure 9.2 were added to specific locations to maintain an even keel floating position at a draft of 9 cm. The final weight and COG position is summarized in Table 9.2.

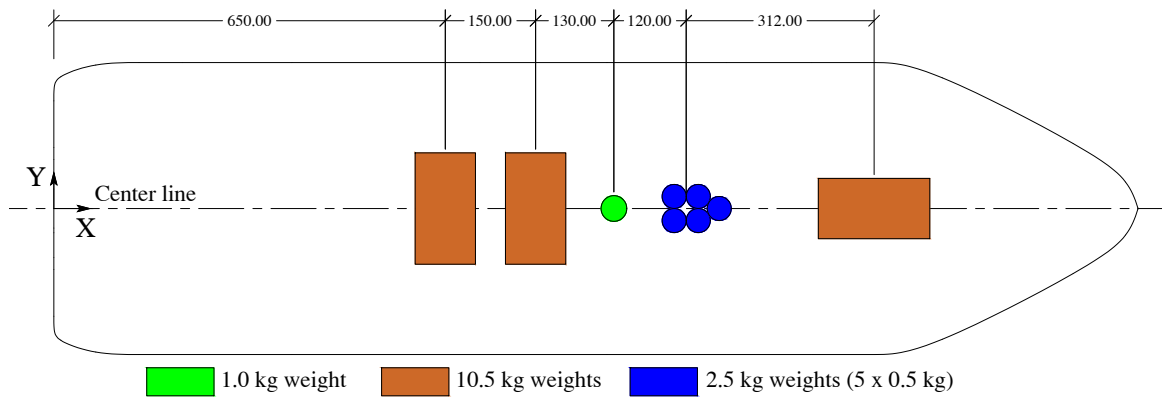


Figure 9.2: Additional solid weights layout for maintaining models draft of 9.0 cm during the model trials, with dimensions specified in millimeters

Table 9.2: Model final weight and COG

Parameter	Symbol	Value	unit
Lightweight	W	53.5	kgs
Longitudinal center of gravity	LCG	86.6	Centimeters from AFT
Transverse center of gravity	TCG	0.00	Centimeters from CL
Vertical center of gravity	VCG/KG	8.00	Centimeters from Baseline

9.2 Model static thrust or bollard pull test

The first test that was done was the static thrust test or the bollard pull test. Although this kind of test is only dedicated to tug boats, it still can provide some valuable insights into the propulsion system efficiency.

The test configuration is about attaching the model to a load cell that measures how much pulling force is applied on the line under the effect of different propeller loading. Since the ship is stationary, the hull resistance and other parameters related to the ship's speed such as η_D are not influenced. Nevertheless, this test still can detect possible propeller cavitation occurrences.

From the data processing point of view, this test involved recording data from two different sources (the onboard autopilot and the onshore load cell) which allows putting the developed Python code for data synchronizing and compilation in a test.

Besides the load cell reading, the relevant data captured during the test from the autopilot were the battery current drawn, battery voltage, battery output power, and the throttle percentage. These data showed a consistent frequency of 1 reading per 0.1 seconds while the load cell reading has a 5 times higher frequency.

Nonetheless, the battery voltage and drawn current are not included in the following study. The reason behind that is that the battery output energy parameters encapsulate both parameters with respect to the time step. These parameters correlation is represented by this direct relation ($E = V \times I \times Time$).

Since power is the derivative of energy by definition. Then, the instantaneous power drawn was derived by differentiating the given energy values with respect to the established time step. This simple mathematical computation can be done using a forward differentiation as shown in Equation (9.1).

$$Power = \frac{dE(t)}{dt} = \frac{E(t) - E(t - \Delta t)}{\Delta t} \quad (9.1)$$

Table 9.3 concludes the different available parameters including their units, source, and frequency.

Table 9.3: Static thrust test captured parameters with their attributes

Parameter	Unit	Source	Frequency (Hz)	No. of data points	Duration (Minutes)
Battery current	Amps	Autopilot	10	5455	09:05.400
Battery voltage	Volt	Autopilot	10	5455	09:05.400
Battery output power	Watt	Driven	10	5455	09:05.400
Battery energy	Wh	Autopilot	10	5455	09:05.400
Throttle percentage	%	Autopilot	10	5455	09:05.400
Thrust force	g-force	Load cell	50	15004	04:59.982

It is worth noting the significance of the throttle percentage value in this context. It not only mirrors the behavior of the other parameters exceptionally well but also its signal does

not suffer from any noise or outliers. This is due to the fact that the throttle signal is a manually input signal given by the RC operator through the remote control. Unlike other parameters, the throttle signal remains immune to external disturbances. These attributes render the throttle signal very reliable when it comes to selecting a reference to validate the pre-processing procedures.

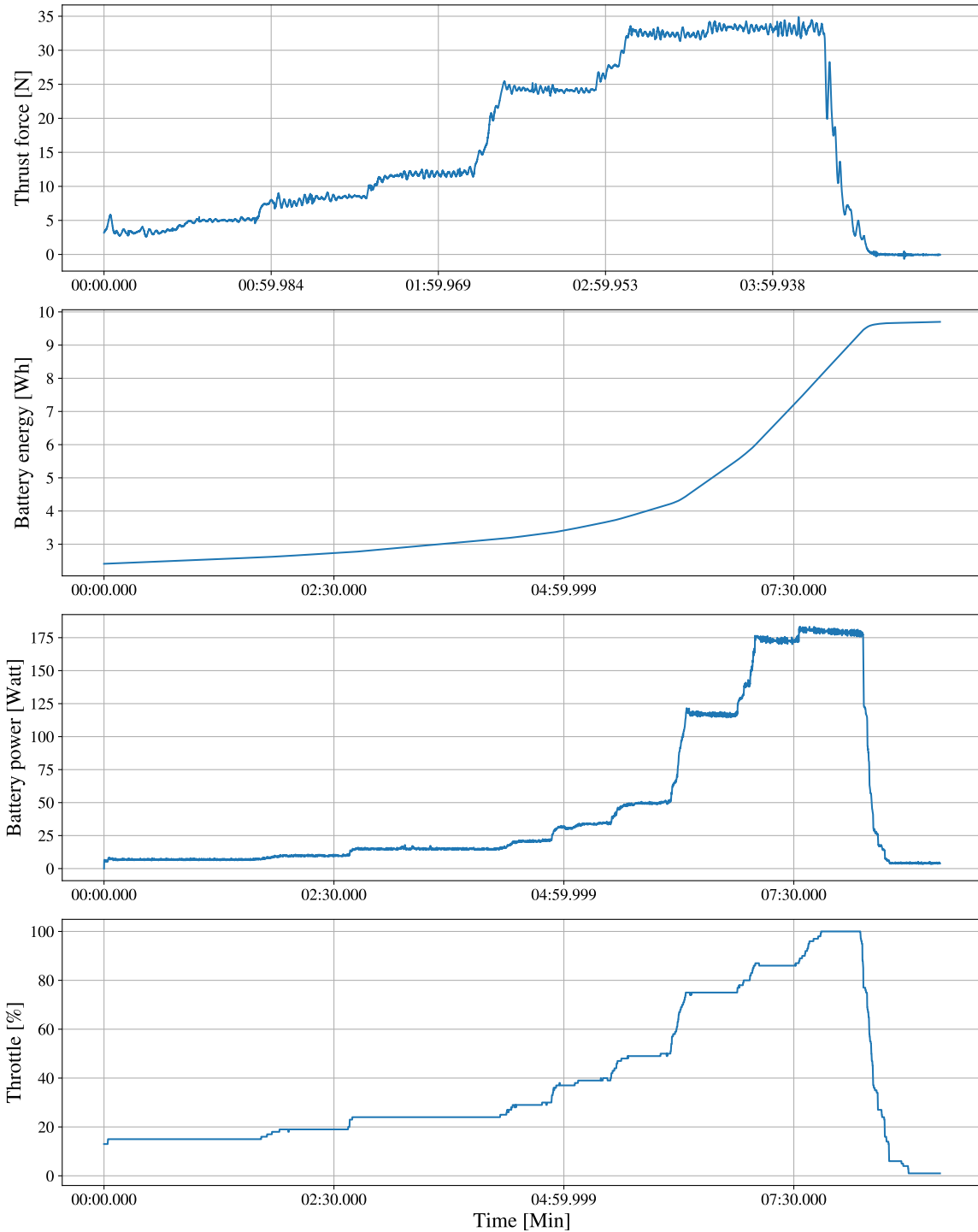


Figure 9.3: Time series graph for the parameters involved in the static thrust test (thrust force, battery drawn energy, battery power, and throttle percentage)

Figure 9.3 gives a first insight into the chosen data for analysis. In this graph, there are two major observations. The first is the misalignment between the thrust force signal and other signals. The second observation is the strong correlation between the throttle and the battery power signals with the exception that the throttle signal exhibits almost no noise. Also for the sake of compatibility, the measuring unit of the load cell was converted from gram force to newtons.

9.2.1 Data synchronizing

As explained in the Chapter 8, the first preprocessing step is synchronizing the data. Since only the thrust force signal is showing different behavior in terms of frequency and length. It is plausible to only synchronize it to the rest of the other data sets.

The difference in both signal length and frequency made the DTW the optimum choice for the synchronizing task. this decision was supported by the DTW inherent capacity to stretch or compress one signal to match the target signal. The throttle signal was assigned a target signal in this context because of the above-mentioned reasons.

9.2.1.1 Dynamic time warping

As shown in Figure 9.3, the maximum throttle value is 100% while the maximum thrust force value is 3.5 N which is a significantly less value numerically. This big gap in the values will distract the DTW algorithm from picking the perfect matching points. To overcome this issue, both data set values were normalized which means that all values in both data sets will have values between [0,1]. This is done by Equation (9.2). However, the original values are retrieved after the synchronization is done.

$$X_{Normalized} = \frac{X - X_{Min}}{X_{Max} - X_{Min}} \quad (9.2)$$

Where X_{Min} and X_{Max} are the minimum and maximum values in the data set respectively.

Applying the developed code, the thrust force signal was synchronized to the throttle signal. Figure 9.4 illustrates aligning paths between trust force signal data points to their corresponding data points in the throttle signal. The plot is meant only to demonstrate the concept behind the DTW algorithm with no intention to show the time step of any signal numeric values.

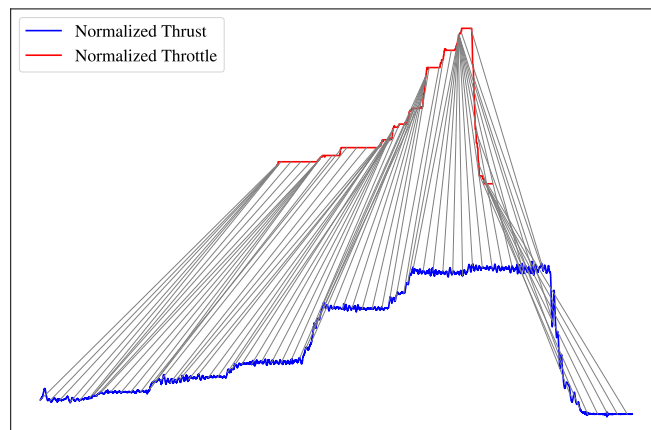


Figure 9.4: DTW data points aligning visualization

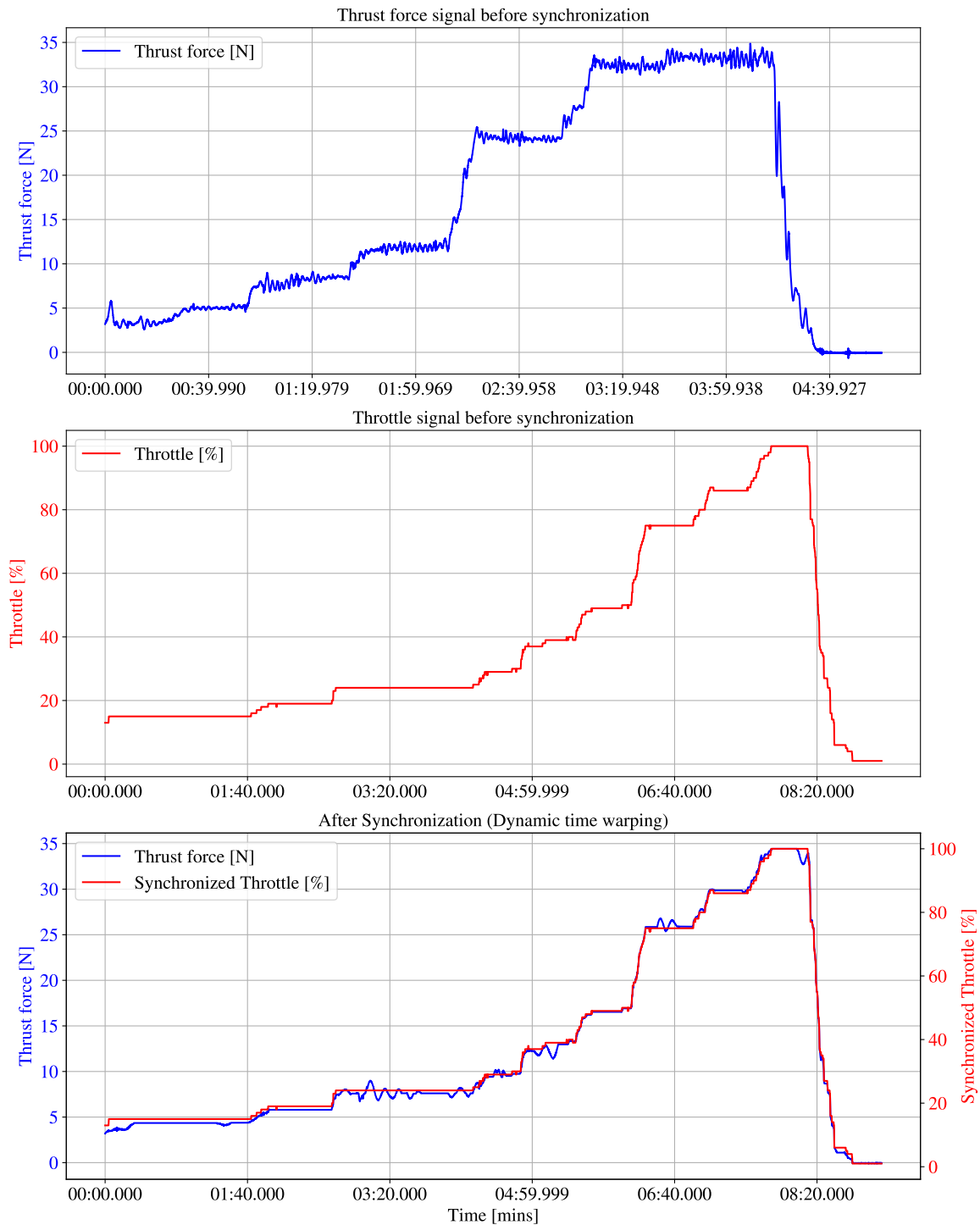


Figure 9.5: A graphical representation of the throttle and thrust force signals before and after synchronizing using DTW algorithm

Figure 9.5 shows the final results of the synchronized data set after retrieving their original units. It is notable that the thrust force signal length has been changed from about 4:39 to 8:20 minutes, thanks to the "elastic" transformation feature of the DTW. It worth to emphasize here that this transformation does not mean that the thrust signal is distorted.

Furthermore, the synchronized signals have a significantly high correlation coefficient based

on three different correlation methods as shown in Table 9.4.

Table 9.4: Correlation coefficients between throttle and thrust force signals before and after synchronizing using dynamic time warping method using (Pearson, Spearman’s rank and Distance correlation)

	Pearson’s correlation	Spearman’s rank correlation	Distance correlation
Before synchronizing	0.5086	0.5746	0.5668
After synchronizing	0.9994	0.9938	0.9994

However, if the data sets are highly populated and attributed with different frequencies, DTW can be employed with less computational effort involved. This can be achieved by down-sampling the data set to a known time step. In this context, the load cell records are taken each 0.02 seconds, which is a relatively minimal interval with respect to other parameters. Then it was decided to down-sample the thrust force signal to a 10 Hz frequency (1 record per 0.1 seconds) to match other frequencies. The down-sampling process was done in steps to capture any sudden behavior that might occur. The representation of synchronizing results is graphically demonstrated in Figure 9.6. This graph demonstrated subtle fluctuations in the correlation coefficient, even though the reduction in the number of data points was substantial, resulting in a noticeable decrease in memory usage and elapsed time.

To recap this, the results of the synchronizing results for the final down-sampling step were compared against those from the original data set. The comparison is shown in Table 9.5. The observation that Spearman’s rank correlation has slightly improved during down-sampling was somewhat unexpected. This can potentially be attributed to the down-sampling process itself. As the signal is down-sampled, the inherent noise is mitigated through value averaging. Consequently, this reduction in noise might create a more conducive environment for Spearman’s rank correlation method to accurately capture the monotonic relationship between the two data sets.

It can be concluded that the same or even better results were obtainable with almost 60% of the computational efforts saved.

Table 9.5: DTW results comparison before and after data downsampling (from 50 Hz to 10 Hz)

Time step, in ms	0.02	0.10
Frequency, in Hz	50	10
No. of data points	15000	3000
Elapsed time, in ms	438.4	177.7
Memory usage, in MiB	50.01	20.95
Pearson’s correlation	0.9996	0.9995
Spearman’s rank correlation	0.9939	0.9969
Distance correlation	0.9995	0.9994

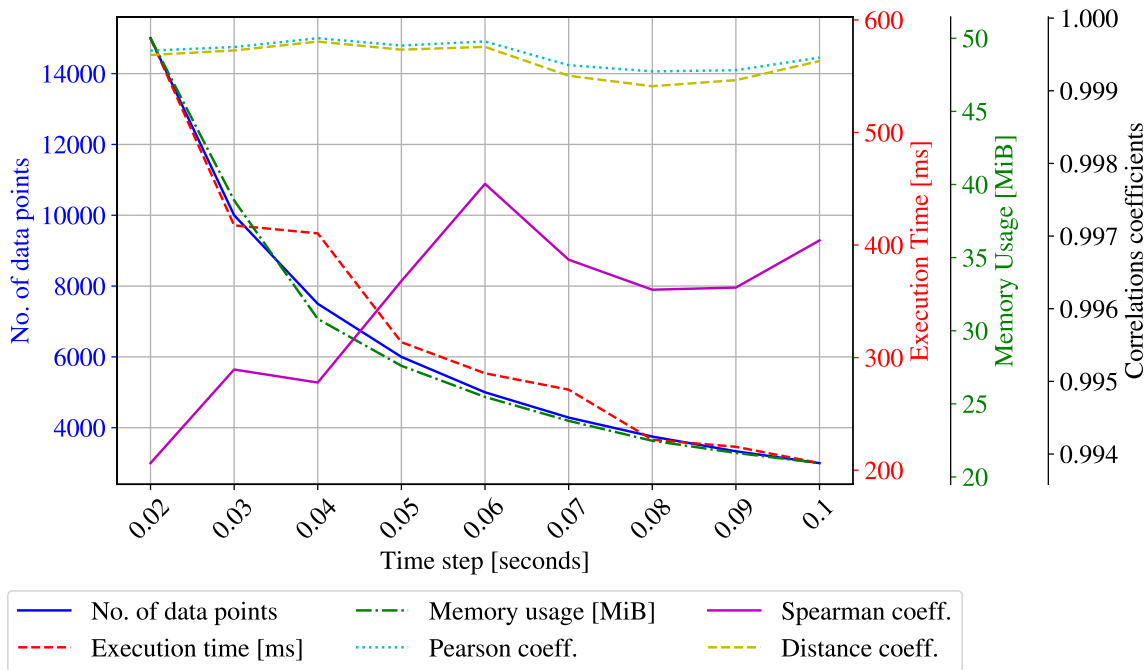


Figure 9.6: A graphical representation of the synchronizing process results with different signal downsampling rates for the thrust force signal

9.2.1.2 Cross-correlation

For the sake of comparison, the cross-correlation method was also employed in synchronizing the same two data sets. The cross-correlation method does not enjoy the time-warping feature. Therefore, it is recommended to be applied to data sets that have the same frequency and length. To achieve that in the current case, the thrust force signal is been averaged to match the throttle signal. This is done by using the recommended compilation method from ISO 19030. After compilation, the data sets are ready for cross-correlation employment which evolves sliding one data set over the other until the maximum correlation is found. Similarly, the correlation coefficients of the synchronized data sets were computed before and after data synchronizing to fully evaluate the method's performance. The correlation coefficients are shown in Table 9.6.

Table 9.6: Correlation coefficients (Pearson, Spearman's rank, and Distance correlation) between the throttle and thrust force signals before and after synchronization using the cross-correlation method.

	Pearson's correlation	Spearman's rank correlation	Distance correlation
Before synchronizing (with compilation)	-0.4155	-0.4769	0.5668
After synchronizing (with compilation)	0.9815	0.9907	0.9892
Before synchronizing (without compilation)	-0.5086	-0.6883	NA
After synchronizing (without compilation)	0.6782	0.8114	0.7151

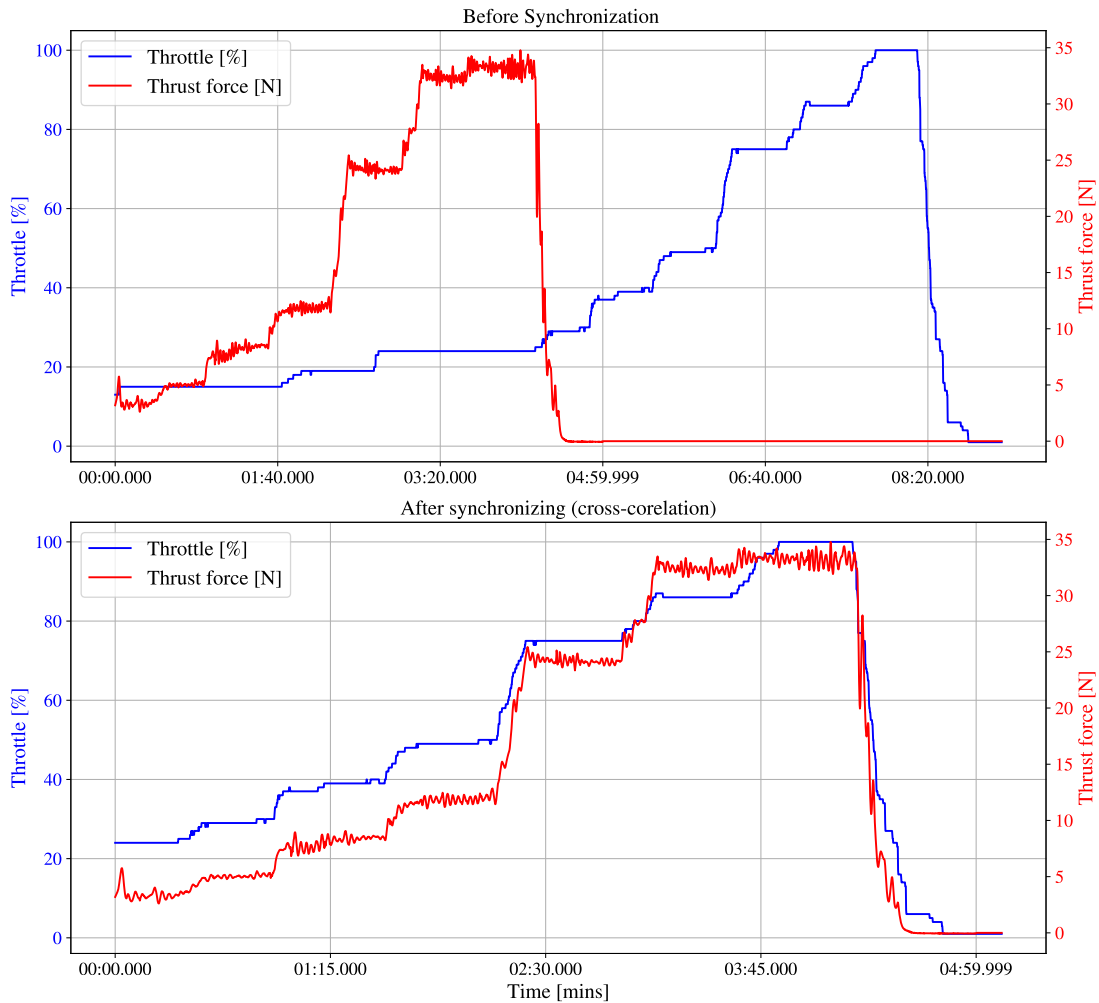


Figure 9.7: A comparison between the unsynchronized and synchronized result using cross-correlation method

9.2.1.3 Comparison and discussion

Considering the correlation coefficient values shown in Table 9.4 and Table 9.6, both methods showed very close results since there is not much gap between coefficient values. However, On one hand, DTW still have the advantage of warping the signal along the time axis to match the desired signal length. This allowed direct employment of DTW without the need for any preparation for the data set. On the other hand, the cross-correlation required data compilation to provide satisfactory results.

It is of high importance also to consider the computational resources required by both methods, this is summarized in Table 9.7. It is evident that the DTW method is computationally more intensive compared to the cross-correlation method although the data point count is only 3 times higher. This can be attributed to its remarkable warping capability that involves constructing a cost matrix with a dimension equal to the number of data points of each data set. In contrast, the cross-correlation method involves finding the signal lag that corresponds to the maximum correlation.

Compiling the data from high to low frequency also contributed to facilitating the synchronizing process with the cross-correlation. A similar effect was also experienced on DTW

when the data set underwent downsampling.

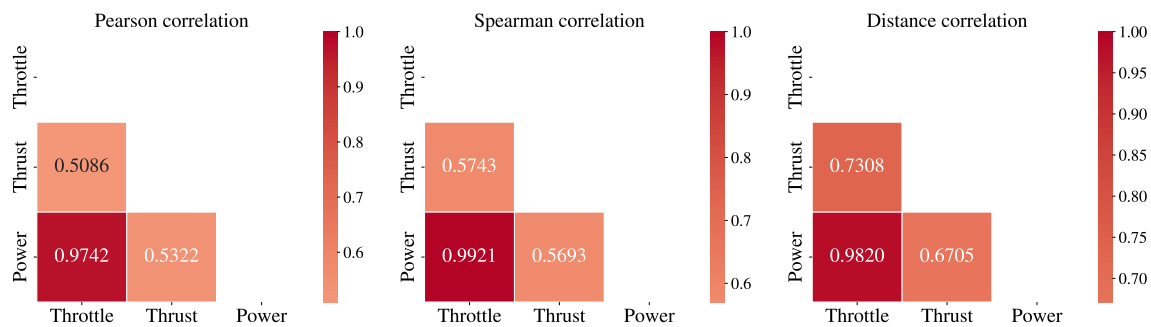
Table 9.7: Synchronizing methods computational efforts comparison

Method	Thrust force data set size	Throttle data set size	Elapsed time (milliseconds)	Memory (MB)
DTW	15004	5455	451.9	49.95
DTW (1 Hz down-sampled)	3000	5455	177.7	20.95
Cross-correlation	5455	5455	1.56	0.34

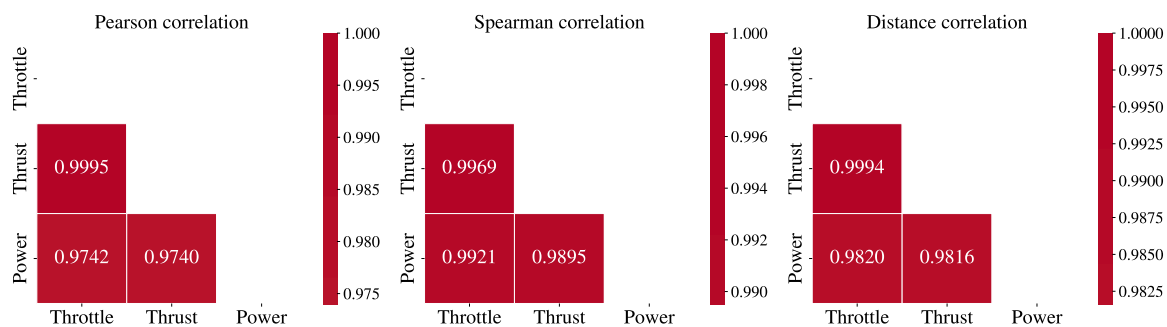
In general, it would be very advisable to merge the DTW with signal downsampling technique to leverage from both the warping feature will minimum computational effort.

9.2.1.4 Data evaluation

Since the other parameters have the same frequency and correlate well with the throttle signal. It is necessary to check the overall correlation between all parameters before heading to the next preprocessing step. This time, a heat map graphical presentation in Figure 9.8 was employed for better visualization.



(a) A heatmap depicting the correlation coefficients among the parameters (throttle, power, and thrust force) using three distinct correlation methods (Pearson, Spearman’s rank, and Distance correlation) before synchronization.



(b) A heatmap depicting the correlation coefficients among the parameters (throttle, power, and thrust force) using three distinct correlation methods (Pearson, Spearman’s rank, and Distance correlation) after synchronization using DTW

Figure 9.8: Comparison of the correlation matrices among the parameters (throttle, battery power, and thrust force) using three different correlation methods (Pearson, Spearman’s rank, and Distance correlation) before and after synchronization, employing a heat map visualization technique

9.2.2 Data denoising

As shown in Figure 9.3, parameters such as battery power, and thrust force exhibit noisy signals. This noise is an entirely undesirable attribute that necessitates reduction if not elimination. For the sake of the experiment, two distinct approaches were employed.

9.2.2.1 Kalman filter

As explained in Chapter 8, the challenge of the Kalman filter is to determine the measurement noise variance (R_n) and process noise variance (Q_n). Ananthasayanam (2018) proposed a hypothesis for tuning these values. However, it was decided to iterative process by systematically trying different values for (R_n) and (Q_n). The results signal is then correlated with a reference signal. The optimum (R_n) and (Q_n) chosen were those that achieve the highest correlation with the throttle signal.

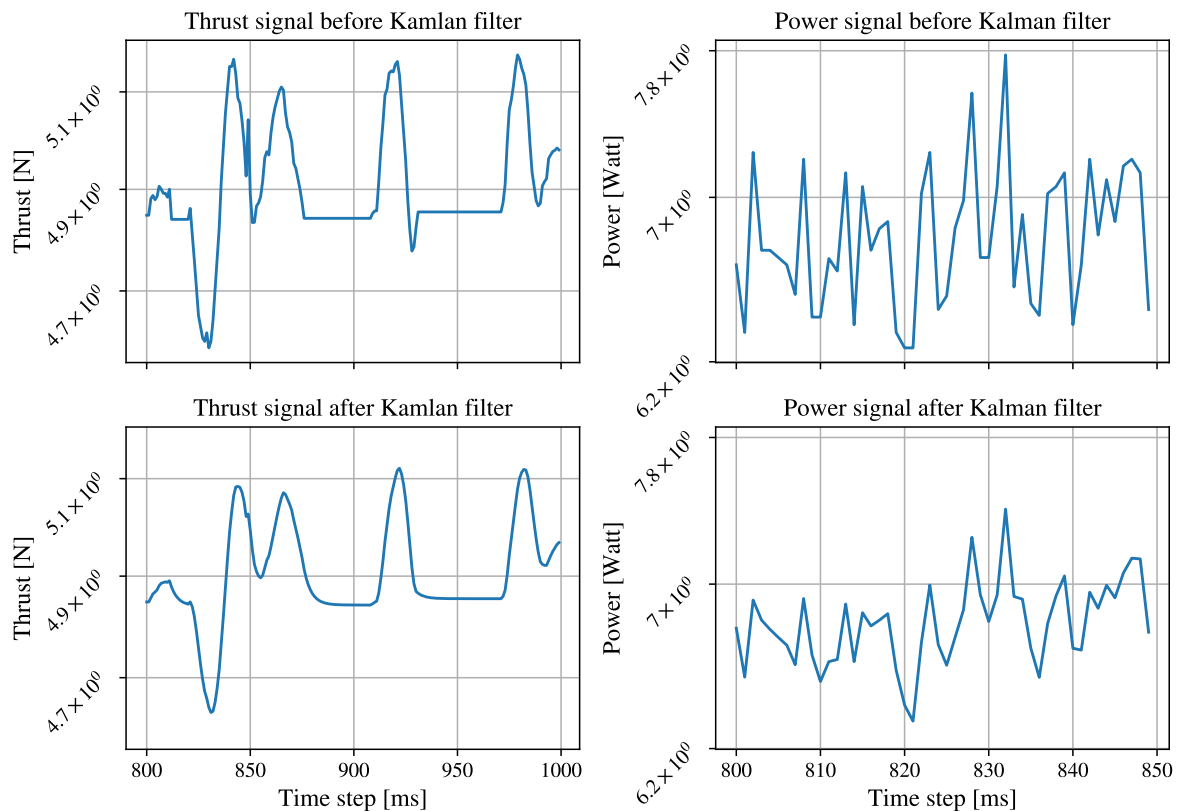


Figure 9.9: A comparison of thrust and power signals within a time window before and after the implementation of the Kalman filter.

In the above figures, a time window was extracted from the complete signal to visually emphasize the impact of the denoising process. Additionally, the y-axis was set to a logarithmic scale. It is visually notable that the power signal spikes are mitigated, while the thrust force signal was slightly smoothed. This distinct behavior of the thrust force signal can be attributed to the earlier down-sampling procedure, which included a data synchronization step.

9.2.2.2 Low-pass filter

The second approach used is the Low-pass filter (LPF) conjugated with FFT. This approach is also requiring tuning the frequency threshold value that will set the lower limit for the accepted frequencies. Similarly, the chosen threshold value used is the one that allows maximum correlation with the throttle reference signal. It is worth mentioning that this method is less complex and easier to be comprehended.

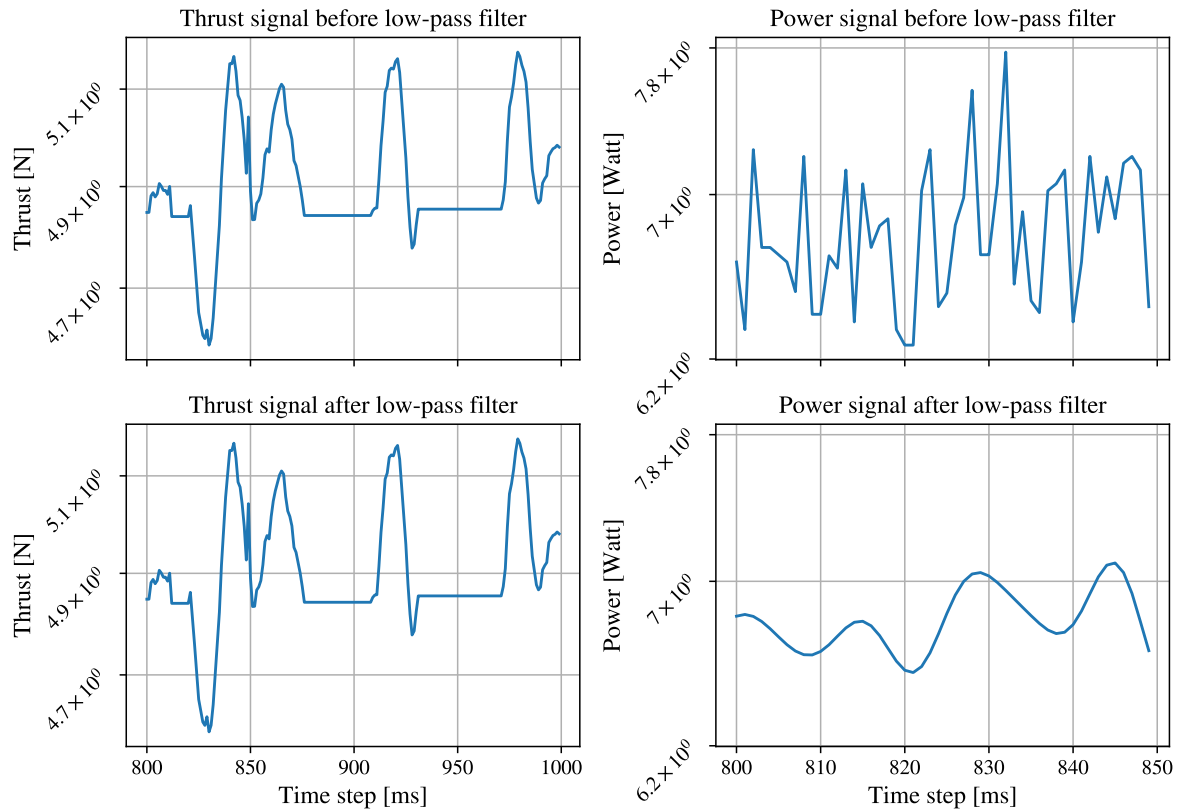


Figure 9.10: Thrust and power signal comparison before and after applying the low-pass filter

It is unsurprising that the thrust signal remains unchanged due to the reasons mentioned earlier, while the battery power signal has undergone substantial smoothing through the implementation of the filter approach.

9.2.2.3 Comparison and discussion

In order to summarize the denoising step, it is necessary to have additional numeric values that emphasize how the signals have been affected. The concept here is to measure what is known as Signal-to-noise ratio (SNR) that represents the level of a desired signal to the level of background noise. This is computed using Equation (9.3)

$$SNR(dB) = 10 \log \left(\frac{P_{\text{signal}}}{P_{\text{noise}}} \right) \quad (9.3)$$

Where P_{signal} and P_{noise} are the power of the desired signal and the power of the noise in the signal respectively. The signal power for the discrete signal is calculated using Equation (9.4).

$$P_{\text{signal/noise}} = \frac{1}{N} \sum_{n=0}^{N-1} |x[n]|^2 \quad (9.4)$$

Where N and $x[n]$ are the number of signal entries and their values respectively. The challenge here is there is no clear signal available to use as reference in SNR computation. Therefore, it was decided to create an artificial signal with respect to the existing signal. This artificial signal has no other rule except being a baseline to compare the denoised signal against.

This artificial signal was created by utilizing the simple moving average (SMA) approach. SMA is the most basic form of time series smoothing. It works by averaging a set number of past data points to produce a smoothed value (Hansun, 2013). It can be mathematically represented by SMA.

$$SMA = \frac{P_M + P_{M-1} + \dots + P_{M-(n-1)}}{n} \quad (9.5)$$

the degree of smoothness of the obtained signal is controlled by the number of entries taken in each averaging process or what is known as (sliding window size (SWS) (Alexander et al., 2016)). The bigger window size results in a smoother signal. Hence, a decision was made to employ a window size of five to generate the fairly smoothed signal. It's crucial to emphasize that the primary intent behind this smoothing process is to create a smoothed reference signal explicitly for the purpose of comparison with other real signals. The fidelity of the resultant signal isn't a primary concern, as it will serve as a singular reference against which all other signals will be juxtaposed for comparison.

Subsequently, the original signal, as well as the signals processed with Kalman filtering and low-pass filtering, were all compared to the reference signal. The resulting SNR is summarized in Table 9.8.

Table 9.8: Signal-to-noise values for different signal-denoising approaches

	Original signal	Kalman filter	Low-pass Filter
Thrust signal SNR, in dB	38.962	41.889	38.981
Power signal SNR, in dB	37.407	39.123	39.337

The SNR values obtained showed almost similar behavior from both filtering approaches when applied to the battery power signal. However, the Kalman-filtered thrust signal has slightly higher SNR which means that the signal is more dominant than the noise.

To have a broader view of these filtering approaches' results, the correlation between the power and the thrust signal was checked with the throttle signal. The results are listed in Table 9.9.

Table 9.9: Comparison between different correlation coefficients between the denoised signals and the throttle reference signal

	Pearson's correlation	Spearman's rank correlation	Distance correlation
Thrust force (Original)	0.9995	0.9969	0.9994
Thrust force (KF)	0.9995	0.9954	0.9995
Thrust force (LPF)	0.9995	0.9928	0.9994
Battery power (Original)	0.9742	0.9921	0.9820
Battery power (KF)	0.9742	0.9923	0.9820
Battery power (LPF)	0.9742	0.9924	0.9821

In the provided table, it is noticeable that data denoising does not significantly influence the correlation with the reference throttle signal. This phenomenon can be attributed to the underlying principles of the correlation methods, which primarily focus on assessing overall linearity, monotonicity, or nonlinearity across the entire signal range. These fundamental characteristics are minimally affected by relatively weak noises. Nonetheless, the comparison of SNR yielded more distinct variations that highlighted the impact of the denoising methods. This also emphasized the effectiveness of the developed code that optimally chose a threshold value that cures the noise without distorting the whole signal .

Since most of the Kalman filter behavior is tied to two coefficients (R_n) and (Q_n), the functionality of it was not conveniently controllable. On the other hand, the LPF function has proven to provide significant fluid manipulation in the aforementioned data processing part. Subsequently, the decision was taken to use LPF conjugated with FFT function for any preceding data denoising.

9.2.3 Outlier detection and removal

As the next step, it was necessary to check the outliers' existence through the data sets. This is done visually by a combination of scatter and box plots as shown in Figure 9.11.

From the naval architect's point of view, The above graph is providing a reasonable correlation between the thrust force and the battery output power. Except for the top right plateau where the battery power is almost constant despite the thrust force still increasing. This behavior might be attributed to a combination of BLDC motor and the propeller efficiency curves which unfortunately were not available to have a deeper look at this behavior.

One of the possible scenarios which still needs to be confirmed by deeper analysis is that as the BLDC motor RPM increases, the motor might start operating in higher efficiency region. Due to this, the motor is drawing the same power but with a higher output thrust force.

From a data analysis point of view, the box plots shown in Figure 9.11 are indicating a decent amount of potential outliers in the battery power readings contrary to the thrust force signal that does not suffer from any. For this, several outliers detection methods were utilized to find the more suitable method to apply.

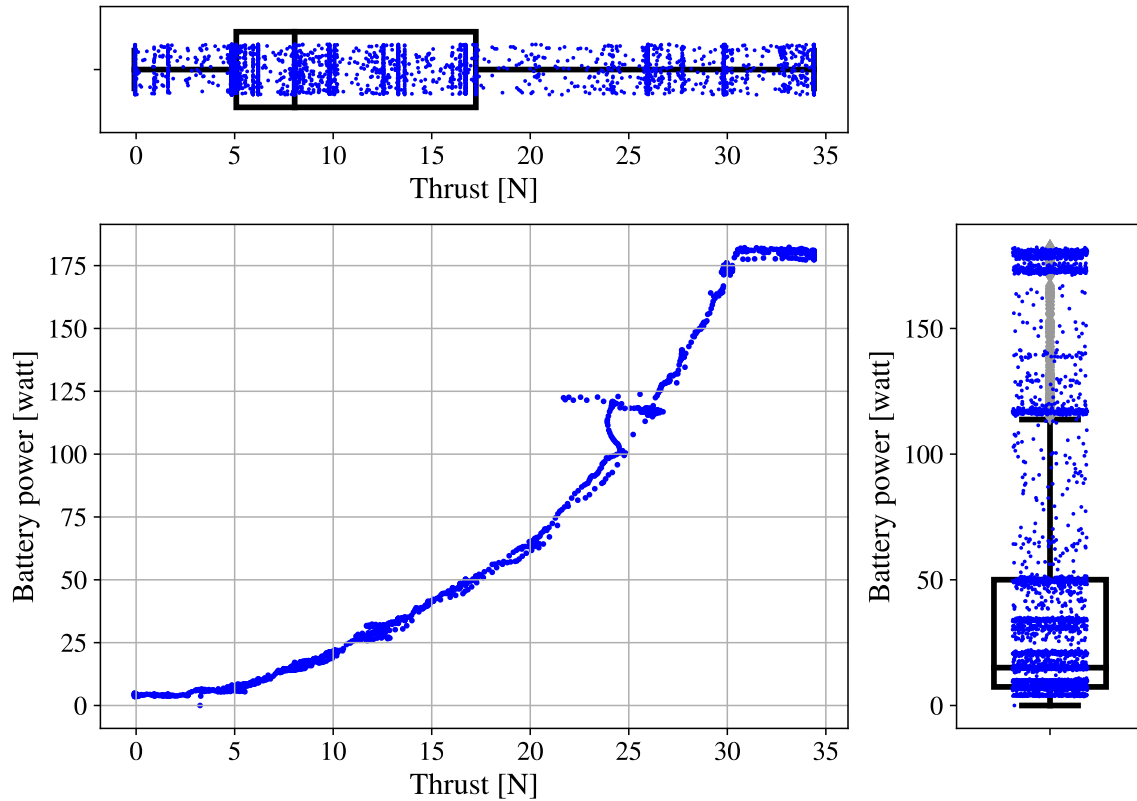


Figure 9.11: Univariate (box plots) versus multivariate (scatter plot) outlier visualization for both battery power and thrust signal recorded during the static thrust test

Another notable phenomenon is the disruption evident in the latter half of the graph, specifically within the range of 100 to 125 watts of battery power reading. This occurrence can be attributed to the model's inclination to rotate around the load cell during the test. Addressing this necessitated manual intervention, involving a slight adjustment to ensure that the model was precisely aligned perpendicular to the load cell, as intended.

9.2.3.1 Univariate outlier detection (as one block)

First, the data sets were checked for potential outliers as one block. This is the most simple and direct approach. The methods utilized were, Z-score, modified Z-score, IQR, and Chauvenet's criteria. Results are listing in Table 9.10

Table 9.10: Univariate outlier detection methods results applied on battery power and thrust force signals

	Z-Score	Modified Z-Score	Interquartile range	Chauvenet criteria
Battery power	0	1294	1183	0
Thrust force	0	1155	0	0

Evidently, both the Z-score and Chauvenet's criteria failed to identify any outliers within both the battery power and thrust data sets. These outcomes can be explained individually

for each method. On one hand, the Z-score primarily identifies outliers based on the standard deviation, which is significantly impacted by the data set’s values and the number of entries, including any possible outliers. Such influence can readily distort the Z-score of all data points. Furthermore, this method is solely applicable to normally distributed data (data that conforms to a bell-shaped histogram distribution) which is not the characteristic exhibited by the data in this scenario.

On the other hand, Chauvenet’s criteria have a different approach, the outliers detection is based on $P(d_i) \cdot N < 0.5$ criteria which is a function of the number of points in the data set. Therefore, the method is less sensitive to detecting outliers if the number of entries is high. To overcome this drawback and according to ISO 19030 recommendations, the filter sensitivity is to be mitigated by reducing the number of points involved in the filter. This is done by dividing the block into equally-spaced time windows and analysis them locally.

Both the modified Z-score and IQR methods have effectively identified a significant number of outliers in the battery power signal. These methods share a common strategy of utilizing the data set’s median value as a reference to identify outliers. This approach mitigates the impact of varying entry values and quantities, thereby enhancing their ability to accurately detect outliers within the data set. The variance in the number of identified outliers stems primarily from the predetermined threshold values within each algorithm, which were initially set to default values. Additionally, these threshold values are a contributing factor to the IQR method’s inability to detect any outliers in the thrust force signal.

9.2.3.2 Univariate outlier detection (as multiple blocks)

To mitigate some of the above-mentioned issues and to investigate the effect of dividing the time series data set into the outliers detection. A small study was done involving an iterating algorithm that can split the data set into a given number of blocks and systemically finds any potential outliers for each block by the methods mentioned before.

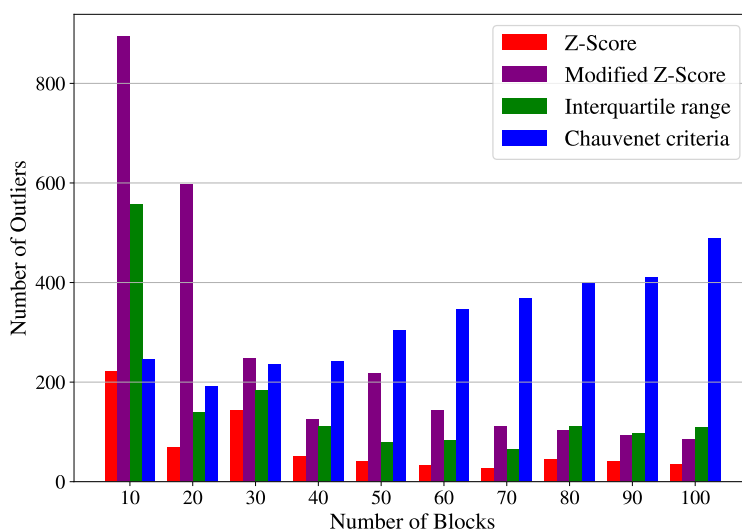


Figure 9.12: A graphical representation of the results of univariate outliers detection methods applied on battery power signal with different time series block sizes

The synthesis of results from both single-block and multiple-block data sets provided a comprehensive framework for comprehending the behavior of these methods across a broader range.

Due to the previously mentioned results, the Z-score method is still attributed to fewer detected outliers. Chauvenet's criteria exhibit a distinct behavior in that, as the number of data points is further reduced, the filtering criteria become progressively more stringent.

The number of outliers detected by both the IQR and modified Z-score methods demonstrates a declining trend as the number of blocks increases. This phenomenon can be attributed to the fact that with a greater number of blocks, fewer data points are taken into consideration. This reduced data coverage enhances the likelihood of a more uniform distribution within each signal block, consequently reducing the identification of outliers. It is worth mentioning that this behavior is predicted to change if the data were inherited by randomness.

9.2.3.3 Discussion

A decision has been made to exclude the Z-score method due to its evident limitations in outlier detection. The focus will now shift to the remaining three methods for the subsequent phase of in-depth analysis. A comprehensive understanding of the outlier detection process will emerge when these identified outliers undergo imputation using various methods. This comprehensive perspective will subsequently guide the selection of the most suitable combination of outlier detection and imputation techniques.

9.2.4 Data imputation

As outlined in the preceding section, an iterative algorithm for outlier detection employing diverse methods and varying block sizes was developed. In this stage, the algorithm was expanded to include three distinct imputation methods (Mean, Time Linear, and kNN). To enhance automation, the algorithm was further designed to compare these outcomes with the reference throttle signal through the three previously detailed correlation methods. The output of this algorithm will be the best combination of several blocks, outlier detection method, imputation method, and correlation coefficients.

The approach employed here involves replacing the outliers with NaNs (Not-a-Number) entries. Then, the role of the imputation method will come to properly approximate these entries.

The ISO 19030 guidelines recommend that when a data point is marked as an outlier, the other corresponding data points for other parameters are systemically considered outliers. This recommendation was followed in this context also since it will ensure consistency between the different parameters.

Another recommendation is that if a data point is detected as an outlier, the whole block is considered an outlier. In the current scenario, this recommendation resulted in massive data removal in a way that imputation methods could not handle. This is attributed to the relatively small data sets we have in comparison with the data sets that are obtainable from

real ships which the ISO 19030 was made for.

The algorithms that were developed were put into action on the battery power parameters, which are more heavily affected by outliers, as indicated in Figure 9.11. Based on the outcomes of the developed algorithm, in conjunction with visual analysis of the output graphs, a decision was reached to prioritize the combination of modified Z-score as the outlier detection method and kNN as the data imputation method for this case. Additionally, this decision aligns with the segmentation of the block into 20 non-overlapping time frames. The resulting data set is shown in a comparison with the original one (ie. the one from the previous step) in Figure 9.13.

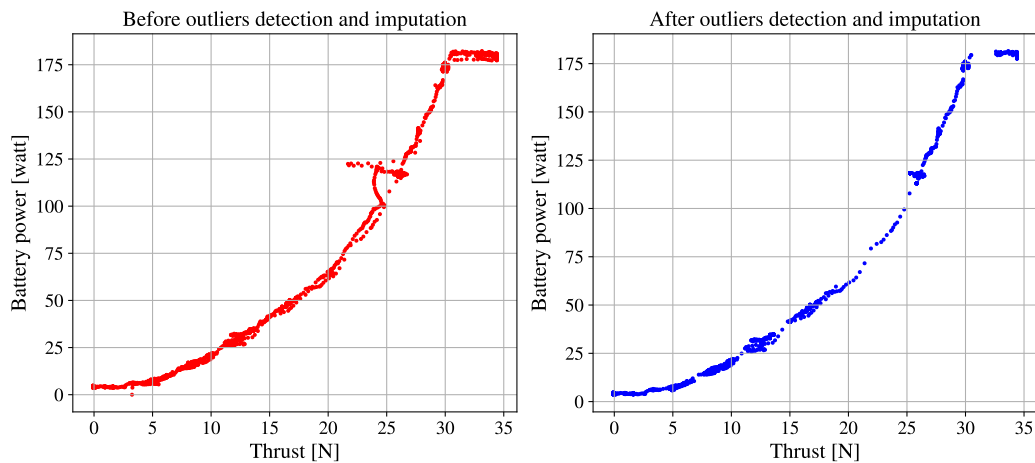
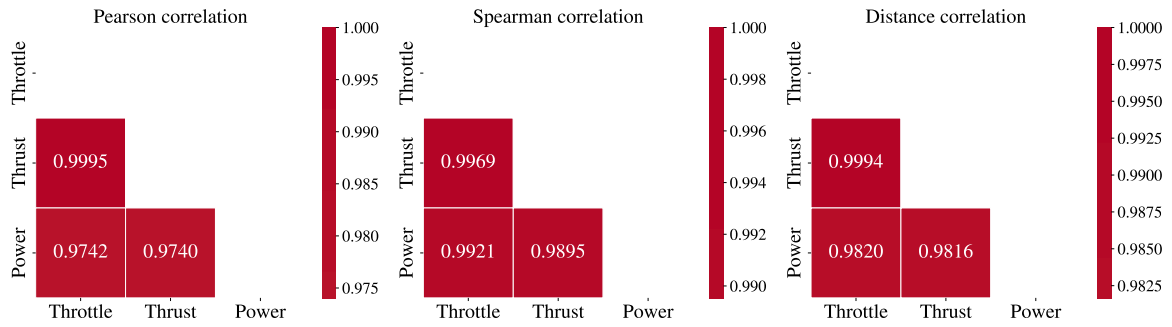


Figure 9.13: A comparison between the dataset before and after outliers removal and data imputation method using modified Z-score and kNN respectively with 20 blocks

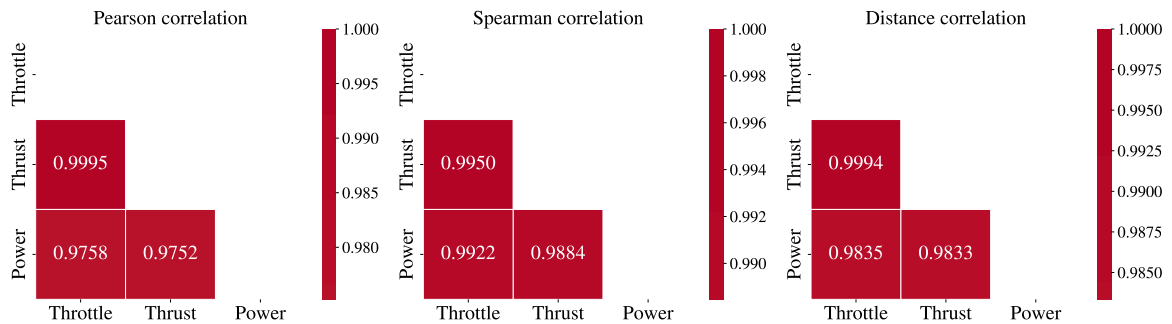
9.2.4.1 Discussion

When analyzing data sets that are quite unknown with no or low prior experience, it is of great help to employ multiple algorithms and methods to workbench and decide the best fit.

The combination chosen gave the chance to appropriately cure the middle disturbance in the graph. It also resulted in a gap in the upper right plateau. However, this part already has different behavior which needed to be analyzed separately. The correlation between the three parameters was also preserved in a good way as shown in Figure 9.14 which ensures the effectiveness of the developed algorithm in detecting and applying the appropriate outlier detection and removal method.



(a) A heatmap depicting the correlation coefficients among the parameters (throttle, power, and thrust force) using three distinct correlation methods (Pearson, Spearman's rank, and Distance correlation) before outliers removal and imputation



(b) A heatmap depicting the correlation coefficients among the parameters (throttle, power, and thrust force) using three distinct correlation methods (Pearson, Spearman's rank, and Distance correlation) after outliers removal and imputation

Figure 9.14: Comparison of the correlation matrices among the parameters (throttle, battery power, and thrust force) using three different correlation methods (Pearson, Spearman's rank, and Distance correlation) before and after outliers removal and imputation using modified Z score, kNN with 20 equal time series blocks, employing a heat map visualization technique

9.2.5 Formulating

As mentioned, the static trust test also known as the bollard pull test is a special kind of test that is conducted for vessels that are involved in towing operations such as tugs and trawlers. It is usually done as part of the sea trial phase when the ship is being delivered.

However, at zero speed thrust with other parameters such as torque and RPM can be used to derive thrust coefficient (K_T) and torque coefficient (K_Q) that can be compared with the same coefficient from the open water tests graphs. This will give an insight into the effect of the hull on the propellers at zero advance coefficient. Therefore, the measured (K_T) and (K_Q) are expected to be less than the ones from the propeller graphs due to the hull effect.

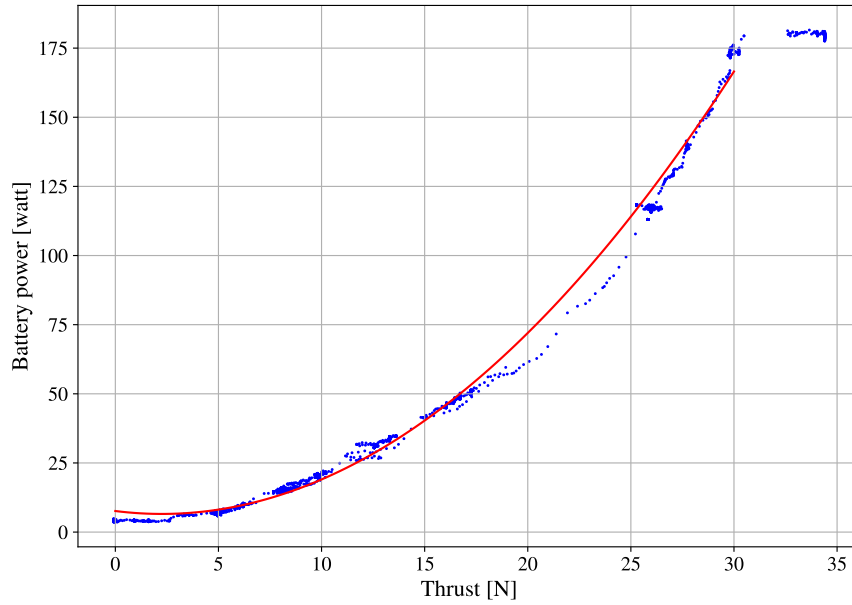


Figure 9.15: Second order curve fitting representing the correlation between the thrust force and battery power at zero speed condition

Nonetheless, for prospective implementations, a correlation was established between the thrust forces measured in newtons and the corresponding battery power in watts. This relationship was determined through curve fitting techniques, as depicted in Figure 9.15.

$$T = 0.21 \times P_{Battery}^2 - 0.94 \times P_{Battery} + 7.62 \text{ with } R^2 = 0.995 \quad (9.6)$$

T is thrust force in newtons and $P_{Battery}$ in watts.

9.3 Model self-propulsion test

Another model test was executed, this time the model was moving freely under his own propulsion system. In this case, the parameters of interest were mainly focused on the model speed and the battery power. These parameters together with the model test results are utilized to derive the propulsion system efficiency.

It is worth noting that this particular run had to take place in an outside environment, allowing for the measurement of vessel speed via GPS. This aspect has implications for the subsequent results, as demonstrated later.

The speed was measured using the GPS module attached to the model, which in turn records these readings in the flight controller (Pixhawk 6). Systemically, the throttle signal with the drawn power from the battery is also recorded on the same device.

Through this data storage approach, all the signals saved on the autopilot will inherently maintain synchronization. This synchronization arises because the data recording process for each signal initiates simultaneously once the model's flight controller is armed. However, it's important to note that certain parameters might possess distinct frequencies. Nonetheless, this variation can be effortlessly managed through the data compilation technique. These attributes of the parameters are summarized in Table 9.11.

Table 9.11: Speed test captured parameters

Parameter	Unit	Source	Frequency (Hz)	No. of data points	Duration (Minutes)
Battery energy	Wh	Autopilot	10	6642	13:31.598
Battery output power	Watt	Driven	10	6642	13:31.598
Throttle percentage	%	Autopilot	10	6642	13:31.598
Speed over the Ground	m/s	GPS module	5	3321	13:31.598

Figure 9.16 provide an overall view of the three parameters mentioned before. The visual correlation between these parameters is very apparent. Additionally, two distinct regions are noteworthy, occurring approximately between time steps 230 and 300 seconds and between 400 and 520 seconds. These segments correspond to instances when the model was driven back to the shore and disarmed for checks. It's important to acknowledge that during this disarming period, although the model wasn't operational, the flight controller continued recording time steps. Consequently, our focus on these regions can be mitigated in subsequent steps.

The parameters were checked for correlations using the previously utilized correlation methods as shown in Figure 9.17.

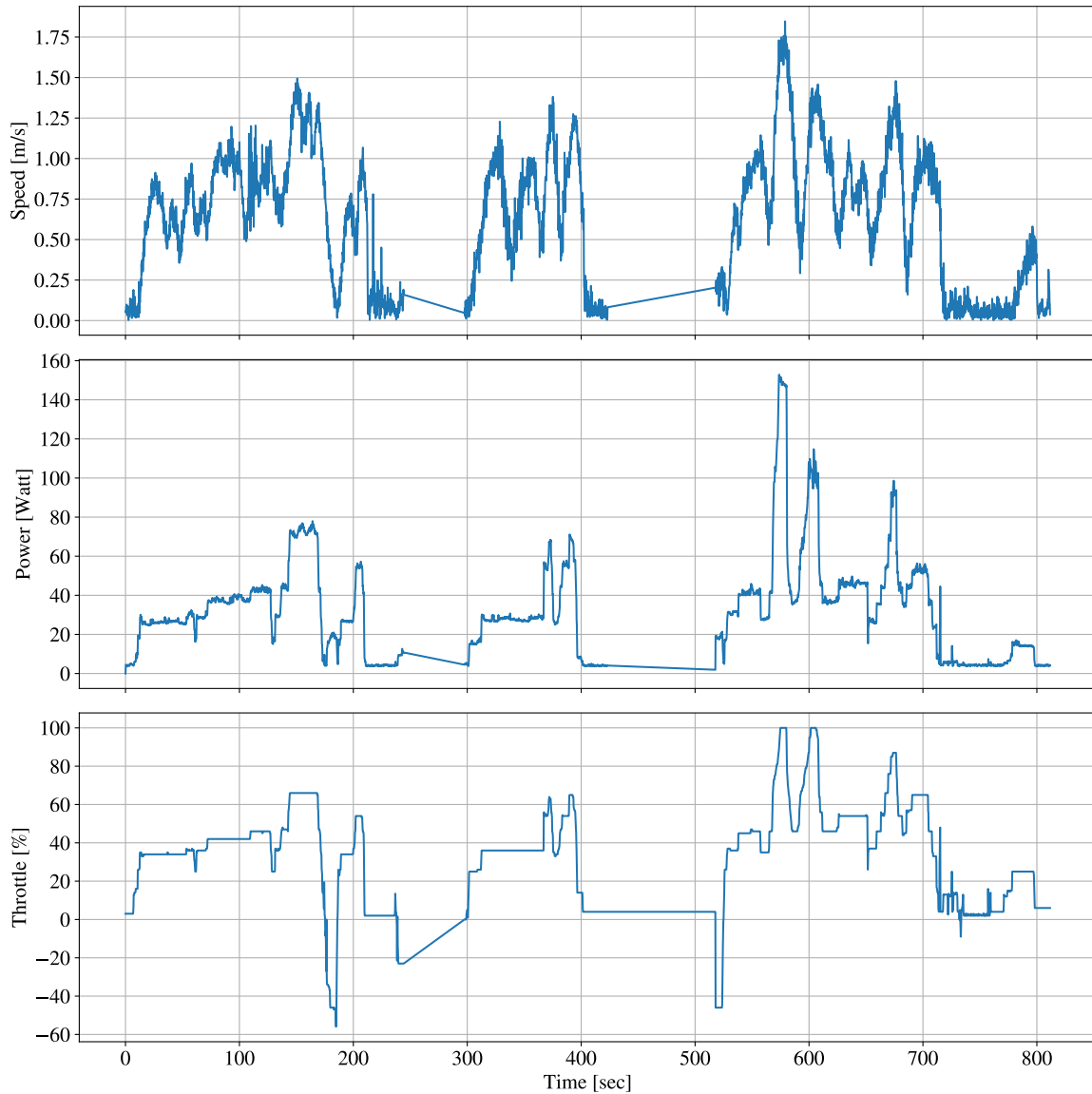


Figure 9.16: Overall insight into the three parameters of interest for the speed runs

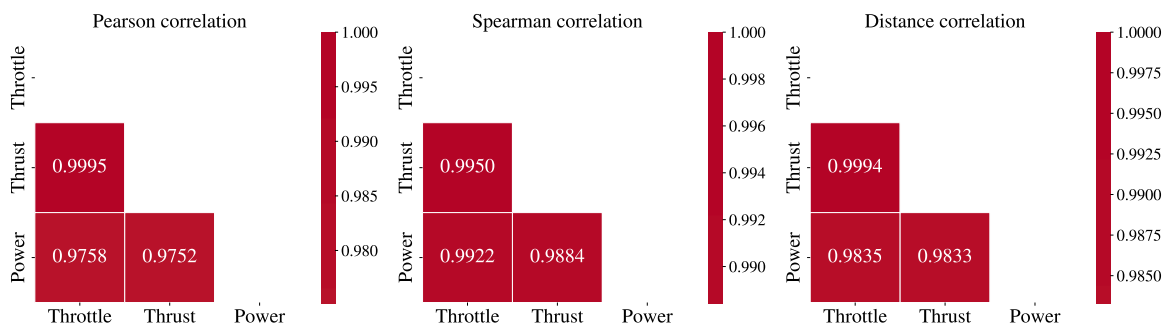


Figure 9.17: A heatmap depicting the correlation coefficients among the parameters (throttle, battery power, and model speed) using three distinct correlation methods (Pearson, Spearman’s rank, and Distance correlation) during the speed test

9.3.1 Data denoising

As explained before, the data noise was mitigated using the LPF for previously mentioned reasons. the results are shown in Figure 9.18 and Table 9.12.

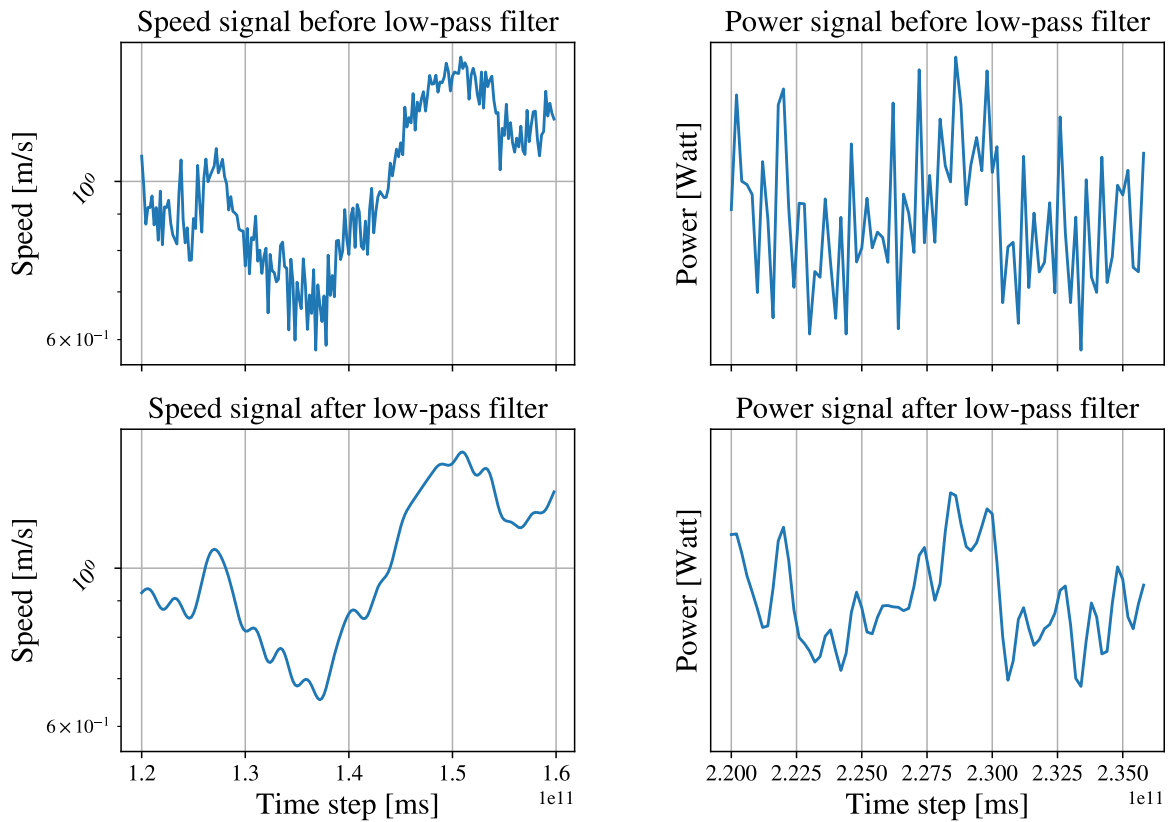


Figure 9.18: Speed and power signal comparison before and after applying the low-pass filter

Table 9.12: Signal-to-noise values for speed and power signals before and after denoising using LPF

	Original signal	Low-pass Filter
Speed signal SNR, in dB	21.860	27.646
Power signal SNR, in dB	22.924	23.181

From the above table, both signals have been affected with denoising process. However speed signal had more impact. The is attributed to its inherent by the excessive noise noted in Figure 9.16.

9.3.2 Outlier detection and data imputation

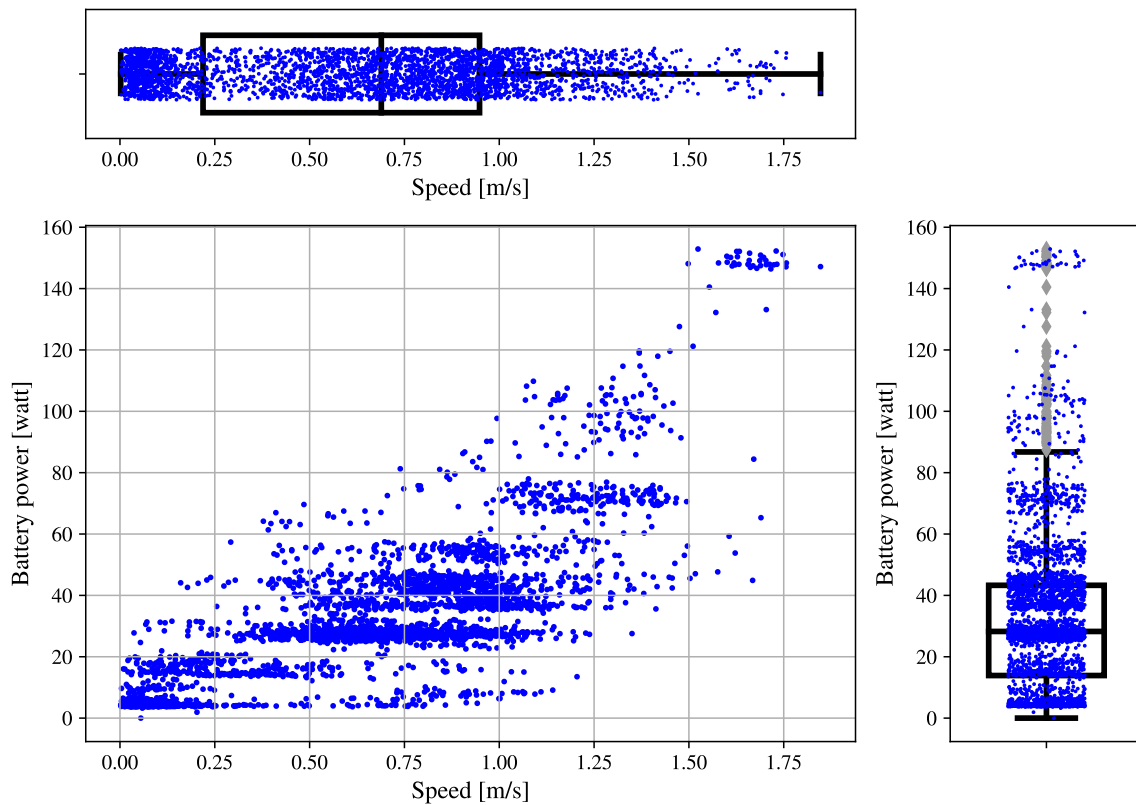


Figure 9.19: Univariate (box plots) versus multivariate (scatter plot) outlier visualization for both model speed and battery power signals recorded during the model self-propulsion test

Figure 9.19 shows a very noisy scatter graph between the model speed and battery power. It can be noted that the point could have some consistent pattern where it can be seen that at a single value of battery power, there are multiple values of model speed. This is attributed to multiple reasons

1. The model runs were conducted in an outside environment where some external parameters like wind and waves are affecting the model.
2. The interaction between the battery power and model speed in this context is not straightforward. As there is an ESC in between that regulates the motor RPM according to the load applied on the propellers. Of course in addition to the other power losses in the gearbox, coupling, and stern tube.
3. If at constant power, the model records variable speed. This gives an indication that the model is not accelerating properly which gives an indication about low propeller performance.

Despite this disturbance in the graph, the overall pattern of the points cloud is showing a slight similarity with the conventional speed-power curve where the speed is in cubic relation with the power. Another note is similar to the previous test results, the battery power signal

is featured with a decent amount of outliers.

With such a noisy scatter graph, the performance of the outliers detection and imputation was not satisfactory due to inherently low-quality data. However, at this point, it was necessary to inspect also the scatter diagram of these parameters with the throttle signal as shown in Figure 9.20.

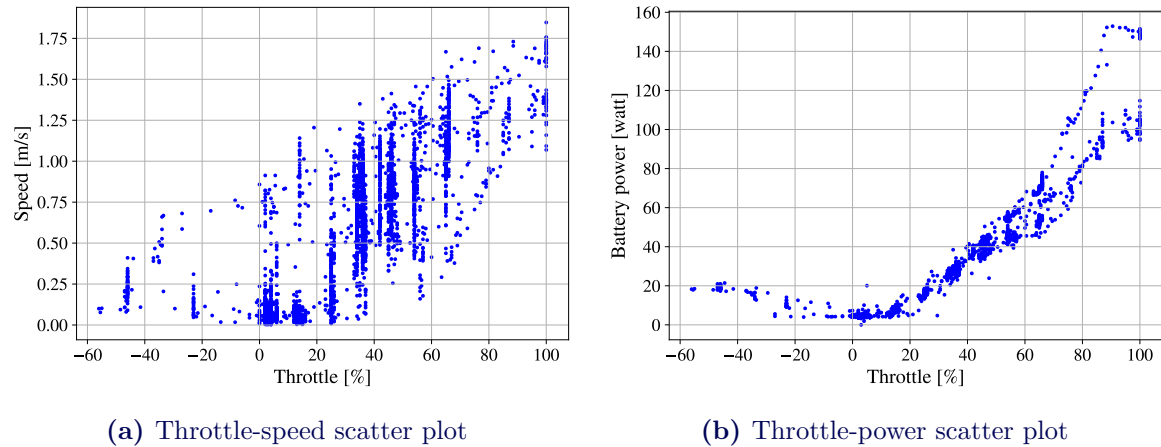


Figure 9.20: Speed and battery power parameters plotted against the throttle value

The above figure emphasizes that the source of the disturbance is the speed measures since the throttle-battery power shows a decent correlation. However, in order to have cleaner data to analyze, it was decided to average the power and the speed values that are corresponding to a single value from the throttle signal.

It is worth noting that there are some negative values of throttle corresponding to positive forward speed. This is because of the attempt to slow down or stop the model while moving. Anyway, these negative throttle values shown in Figure 9.20b were filtered out with their corresponding values from other parameters for better analysis. The resulting scatter plot is shown in Figure 9.21. With this simplified version of the speed-power scatter plot, it is time to proceed to the next steps.

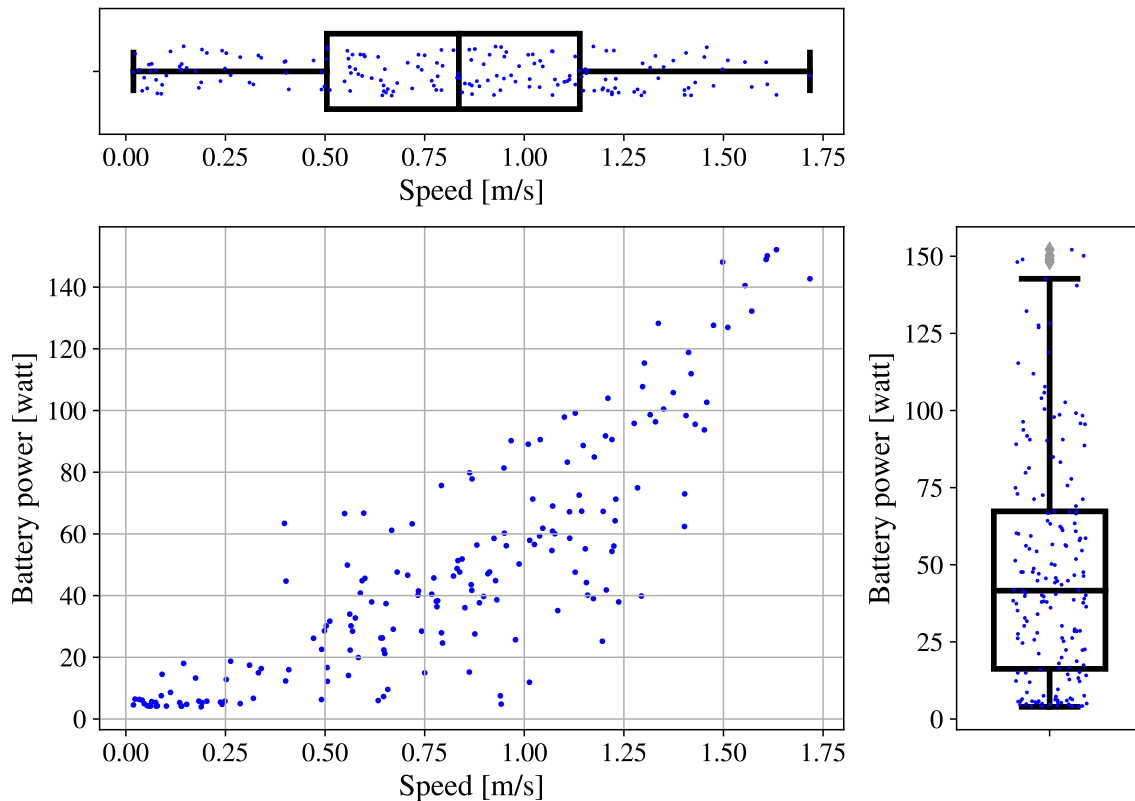


Figure 9.21: Univariate (box plots) versus multivariate (scatter plot) outlier visualization for both model speed and battery power signals recorded during the model self-propulsion test after averaging

Building upon the previously developed algorithm, a decision was made to implement the pairing of Chauvenet’s Criterion for outlier detection with the kNN imputation method. This approach involves segmenting the time series into 2 equal blocks for analysis. This combination showed a good correlation with the throttle signal after removing and imputing the outliers.

To derive a formulation of the acquired results, ISO 19030 recommends utilizing a power-law relationship using log-log transformation. In this method, both parameters were linearized by taking the log and then the curve fitting is done using the following formula

$$\log(P) = \log(a) + b \log(V) + \varepsilon \quad (9.7)$$

where the parameters $\log(a)$ and $\log(b)$ are obtained by fitting a line in $[\log(V), \log(P)]$ space using the linear square method. A power-law relationship is a powerful curve-fitting technique. Which is nonlinear in its original space, and becomes linear in a log-log space. Linear regression methods can then be straightforwardly applied to determine the parameters of the relationship.

This function was added to the developed algorithm and the results are shown in Figure 9.22 and Equation (9.8). the R^2 value of the obtained formulation is only 0.69 which is relatively lower than ISO 19030 recommendations of 0.8.

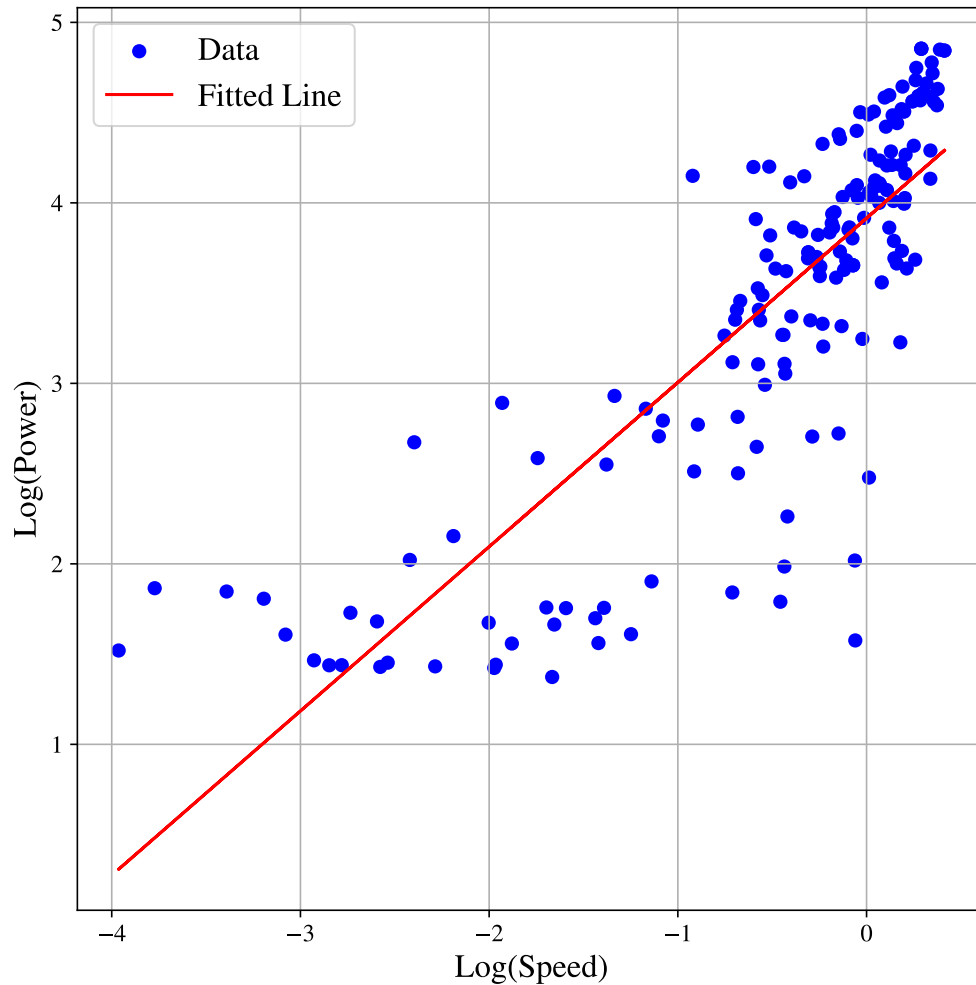


Figure 9.22: Speed and battery power parameters linear regression in log-log space

$$P_{Battery} = 50.16 \times v^{0.91} \quad \text{with } R^2 = 0.69 \quad (9.8)$$

The low R^2 value can be attributed to the poor quality of the obtained data. In any case, it's important to acknowledge these limitations and consider them when interpreting the results.

To enhance these outcomes and subsequently achieve an improved R^2 value that better reflects the underlying relationship, the following solutions are put forth:

- Run the model in a controlled environment where the speed parameters can be measured with correlation with the battery power with minimum influence of the external factors.
- Measuring the motor RPM and torque will give an insight into the power delivered to the propeller. This with proper propeller charts can reflect propeller efficiency.
- Execute more runs to obtain more data. More data means fewer gaps and more accurate

results.

- By considering the recorded rudder angle parameter, it would be enhanced in accuracy to exclude readings aligned with maneuvering phases, and instead prioritize those associated with straight-line runs in the study.

Derived from the established formulation and in consideration of the model's theoretical maximum speed of 1.51 m/s, the resultant battery power corresponds to 73 watts.

With regard to the effective power derived from the model test

$$P_E = R_T \times v = 10.5 \times 1.51 = 15.855 \text{ watts} \quad (9.9)$$

Consequently, the system efficiency encompassing the power train from the battery to the effective power is approximately 0.21, indicating a relatively low level of efficiency. Nonetheless, this initial iteration of the model represents an early stage, and substantial enhancements are anticipated in subsequent iterations.

10

Conclusion and Outlook

In this section, the main key points, and findings will be brought together. This will provide a clear summary of what steps have been followed and what was discovered. Putting them all together will give a bigger picture and understand the importance of this work.

- By combining the RC technologies, the RC model-building techniques, naval architecture principals, and the scientific objective, it was possible to develop a detailed design for a fully functional RC model ship equipped with the necessary sensors to capture a decent amount of meaningful operational parameters.
- The parameters of interest were chosen with respect to the ultimate objective of this project. This will limit the number of sensors reading to those that can provide a high relevant data.
- Working with a scaled-down ship model has it is own drawbacks. The major faced drawback during this work was the availability of such scaled-down equipment. Although almost all of the equipment was available commercially, there were other obstacles such as long delivery time, improper suppliers, or insufficient scientific data about the selected component. However, a list of all proposed solutions together with the suppliers' information was prepared for any future reflections.
- Although a simplified version of the proposed design was used due to time constraints, the built model showed high potential to gather vast amounts of data from different sensors representing different parameters. These data gave proper insights into the system's overall efficiency.
- The data acquired through sensors can be harnessed to derive additional parameters that are not directly observed, thereby expanding the scope of available data. This approach also enables the cross-validation of other parameters.
- With the first runs executed, it was manageable to record valuable data to test the developed data management system with real sensor readings that prove it to be reliable for future utilization and development.
- For the data logging in the RC context, the autopilot offered a very reliable data modeling system. It offered the ability to record multiple parameters in a synchronized way that facilitates the further analysis step.
- The presence of a dependable signal, which exhibits a consistent influence on all other parameters, such as the throttle signal, has substantially facilitated the validation processes.
- In the context of data processing, no single method possesses an absolute advantage.

Various methods, each employing distinct approaches, must be subjected to testing in order to determine the most appropriate one.

- Simple minor techniques such as signal averaging, downsampling, and unit normalization exert a significant influence on the performance of complex algorithms. These techniques can yield equivalent outcomes to those obtained through more computationally intensive processes, or even produce superior results, all while reducing computational burdens and efforts.
- A prior knowledge of the nature of the analyzed data has a positive impact on interpreting the outcomes of sensor data. It can give an early indication if the analysis results will be of use or not.

The subsequent bullet points outline several factors that possess the potential to enhance result outcomes and furnish support for forthcoming advancements.

- **3D scan of the model hull:** during fabricating and fitting some internal components within the model hull, it was noted that there are deviations between the 3D model and the fabricated hull. This deviation was also noted when attempting to achieve the design draft of 9 cm during the towing test since additional 2.13 kgs were added to achieve the required draft. Therefore, a 3D scan of the existing hull is necessary to recreate an accurate 3D model of the existing hull. Then, accurate hydrostatics data will be acquired to be used as reference data for the digital twin application.
- **Propeller open testing:** the propellers used in the model were the nearest match to the reference ship propeller in terms of diameter and the number of blades and were available commercially with a short delivery time. It was also quite challenging to size the required motors to sail the model. Therefore, open water for the available propeller is needed to obtain the necessary propeller graphs to precisely size the electric motors. Another solution is to purchase ready-calibrated propellers of the same size. These graphs will be also used as reference data which the measured data will be compared with.
- **Reference curves:** After the model competition, an extensive amount of runs need to be executed to derive the vast amount of data. These data will be utilized in the first place to develop a reference performance curve correlating different model parameters (Like sea trials in full-scale ships).
- **Engine and dynamo tests:** the chosen component was the nearest commercially available component that can be utilized in this application. However, these components are required to be calibrated in an ideal environment so proper performance curves will be driven and used to evaluate these component performances during the model runs.
- **Sensors reading uncertainty analysis:** The data acquired from the autopilot, the GPS module, and any other conceivable sensors must undergo an uncertainty analysis to ensure the integrity of the results and reliable decision-making results.
- **Sensors calibration:** Although the components obtained offered a valuable reading, it would be highly recommended to calibrate them from time to time to ensure high-quality readings.

- **Machine learning training:** Machine learning models are usually utilized to predict operational conditions that rarely occur such as (excessive trim or heel, very high or low drafts, waves, and shallow waters). With this small-scale model, the operational conditions are producible and controllable to a high extent. Therefore the behavior predicted by machine learning techniques can be easily validated experimentally with low risk.
- **Study of scaling effect in sensor reading:** In order to have a proper insight into the full-scaled vessel with regards to measures taken from scaled-down sensors, dedicated investigations on the scaling results to the reference ship are essential. These investigations should assess the possibility and limitations of such a concept.
- **Multivariate outlier detection** When confronted with multiple sets of time series data, the utilization of multivariate outlier detection techniques, such as isolation forest and local outlier factor, can yield substantial advantages. This approach enhances the alignment across data sets and promotes precise interrelation assessment among them.
- **Runs automation:** To accumulate an extensive data set intended for utilization within the proposed decision support platform, it is imperative for the model to operate within a controlled environment for prolonged durations. This can be achieved autonomously through the synergistic integration of both autopilot and Raspberry Pi functionalities.

This page intentionally left blank.

Bibliography

- Johann Tang. Technical Manual Series: Brushless motor structure and rotation principles, 2021. URL <https://blog.orientalmotor.com/technical-manual-series-brushless-motor-structure-and-rotation-principles>. Accessed 16-Jul-2023.
- Alex Becker. Online kalman filter tutorial, 2023. URL <https://www.kalmanfilter.net/multiSummary.html>. [Accessed 18-Jul-2023].
- Nicolas Azevedo. An introduction to exploratory data analysis | Scalable Path, 1 2022. URL <https://www.scalablepath.com/data-science/exploratory-data-analysis>. Accessed: 19 June 2023.
- Nermin Hasanspahić, Srdjan Vujicic, Leo Čampara, and Klaudia Piekarska. Sustainability and environmental challenges of modern shipping industry. *Istrazivanja i Projektovanja za Privredu*, 19, 12 2020. doi: 10.5937/jaes0-28681.
- Tony R. Walker, Olubukola Adebambo, Monica C. Del Aguila Feijoo, Elias Elhaimer, Tahazzud Hossain, Stuart Johnston Edwards, Courtney E. Morrison, Jessica Romo, Nameeta Sharma, Stephanie Taylor, and Sanam Zomorodi. Chapter 27 - environmental effects of marine transportation. In Charles Sheppard, editor, *World Seas: An Environmental Evaluation (Second Edition)*, pages 505–530. Academic Press, second edition edition, 2019. ISBN 978-0-12-805052-1. doi: <https://doi.org/10.1016/B978-0-12-805052-1.00030-9>. URL <https://www.sciencedirect.com/science/article/pii/B9780128050521000309>.
- Wisam Jabary, Chien Liu, Florian Sprenger, Lutz Kleinsorge, Hauke Baumfalk, Maximilian Kaster, Simon Mewes, Jens Neugebauer, and Ould el Moctar. Development of machine learning approaches to enhance ship operational performance evaluation based on an integrated data model. In *21st Conference on Computer and IT Applications in the Maritime Industries*, pages 153–168, 2023a.
- Omer Berkehan Inal, Jean-Frédéric Charpentier, and Cengiz Deniz. Hybrid power and propulsion systems for ships: Current status and future challenges. *Renewable and Sustainable Energy Reviews*, 156:111965, 2022. ISSN 1364-0321. doi: <https://doi.org/10.1016/j.rser.2021.111965>. URL <https://www.sciencedirect.com/science/article/pii/S1364032121012302>.
- Qikun Wei, Yan Liu, You Dong, Tianyun Li, and Wei Li. A digital twin framework for real-time ship routing considering decarbonization regulatory compliance. *Ocean Engineering*, 278:114407, 2023. ISSN 0029-8018. doi: <https://doi.org/10.1016/j.oceaneng.2023.114407>. URL <https://www.sciencedirect.com/science/article/pii/S0029801823007916>.
- Toh Yen Pang, Juan D. Pelaez Restrepo, Chi-Tsun Cheng, Alim Yasin, Hailey Lim, and Miro Miletic. Developing a digital twin and digital thread framework for an ‘industry 4.0’ shipyard. *Applied Sciences*, 11(3), 2021. ISSN 2076-3417. URL <https://www.mdpi.com/2076-3417/11/3/1097>.
- Elisa Negri, Luca Fumagalli, and Marco Macchi. A review of the roles of digital twin in cps-based production systems. *Procedia Manufacturing*, 11:939–948, 2017. ISSN 2351-9789. doi: <https://doi.org/10.1016/j.promfg.2017.07.198>. URL <https://www.sciencedirect.com/science/article/pii/S2351978917304067>. 27th International Conference on Flexible Automation and Intelligent Manufacturing, FAIM2017, 27-30 June 2017, Modena, Italy.
- José Ríos, Juan Hernandez-Matias, Manuel Oliva, and Fernando Mas. Product avatar as digital counterpart of a physical individual product: Literature review and implications

- in an aircraft. In *Volume: 2 of Advances in Transdisciplinary Engineering*, 07 2015. doi: 10.3233/978-1-61499-544-9-657.
- Werner Kritzing, Matthias Karner, Georg Traar, Jan Henjes, and Wilfried Sihn. Digital twin in manufacturing: A categorical literature review and classification. *IFAC-PapersOnLine*, 51(11):1016–1022, 2018. ISSN 2405-8963. doi: <https://doi.org/10.1016/j.ifacol.2018.08.474>. URL <https://www.sciencedirect.com/science/article/pii/S2405896318316021>. 16th IFAC Symposium on Information Control Problems in Manufacturing INCOM 2018.
- David Guerra-Zubiaga, Vladimir Kuts, Kashif Mahmood, Alex Bondar, Navid Nasajpour-Esfahani, and Tauno Otto. An approach to develop a digital twin for industry 4.0 systems: manufacturing automation case studies. *International Journal of Computer Integrated Manufacturing*, 34(9):933–949, 2021.
- Jan-Erik Giering and Alexander Dyck. Maritime digital twin architecture, a concept for holistic digital twin application for shipbuilding and shipping. *at - Automatisierungstechnik*, 69(12):1081–1095, 2021. doi: [doi:10.1515/auto-2021-0082](https://doi.org/10.1515/auto-2021-0082). URL <https://doi.org/10.1515/auto-2021-0082>.
- BQ Chen, PM Videiro, and C Guedes Soares. Review of digital twin of ships and offshore structures. *Developments in Maritime Technology and Engineering; Guedes Soares, C., Santos, TA, Eds*, pages 445–451, 2021.
- F. Mauro and A.A. Kana. Digital twin for ship life-cycle: A critical systematic review. *Ocean Engineering*, 269:113479, 2023. ISSN 0029-8018. doi: <https://doi.org/10.1016/j.oceaneng.2022.113479>. URL <https://www.sciencedirect.com/science/article/pii/S0029801822027627>.
- Yupeng Yuan, Jixiang Wang, Xinpeng Yan, Boyang Shen, and Teng Long. A review of multi-energy hybrid power system for ships. *Renewable and Sustainable Energy Reviews*, 132:110081, 2020. ISSN 1364-0321. doi: <https://doi.org/10.1016/j.rser.2020.110081>. URL <https://www.sciencedirect.com/science/article/pii/S1364032120303725>.
- D. Gelernter. *Mirror Worlds: or the Day Software Puts the Universe in a Shoebox...How It Will Happen and What It Will Mean*. Oxford University Press, 1993. ISBN 9780190281953. URL https://books.google.de/books?id=PV_nBwAAQBAJ.
- Mengnan Liu, Shuiliang Fang, Huiyue Dong, and Cunzhi Xu. Review of digital twin about concepts, technologies, and industrial applications. *Journal of Manufacturing Systems*, 58: 346–361, 2021. ISSN 0278-6125. doi: <https://doi.org/10.1016/j.jmsy.2020.06.017>. URL <https://www.sciencedirect.com/science/article/pii/S0278612520301072>. Digital Twin towards Smart Manufacturing and Industry 4.0.
- Angira Sharma, Edward Kosasih, Jie Zhang, Alexandra Brintrup, and Anisoara Calinescu. Digital twins: State of the art theory and practice, challenges, and open research questions. *Journal of Industrial Information Integration*, 30:100383, 2022. ISSN 2452-414X. doi: <https://doi.org/10.1016/j.jii.2022.100383>. URL <https://www.sciencedirect.com/science/article/pii/S2452414X22000516>.
- Andrea Coraddu, Luca Oneto, Francesco Baldi, Francesca Cipollini, Mehmet Atlar, and Stefano Savio. Data-driven ship digital twin for estimating the speed loss caused by the marine fouling. *Ocean Engineering*, 186:106063, 2019. ISSN 0029-8018. doi: <https://doi.org/10.1016/j.oceaneng.2019.05.045>. URL <https://www.sciencedirect.com/science/article/pii/S0029801819302616>.
- M Schirmann, M Collette, and J Gose. Ship motion and fatigue damage estimation via a digital twin. In *Life Cycle Analysis and Assessment in Civil Engineering: Towards an Integrated Vision*, pages 2075–2082. CRC Press, 2018.
- S Låg and SW Brathagen. Standardisation as an enabler of digitalisation in the maritime

- industry. *Group Technology & Research, Position Paper, DNV GL AS, Høvik, Norway*, 2017.
- William Froude. Experiments on the surface-friction experienced by a plane moving through water. *British Association for the Advancement of Science*, 42:118–124, 1872.
- Roger Skjetne, Thor I. Fossen, and Petar V. Kokotović. Adaptive maneuvering, with experiments, for a model ship in a marine control laboratory. *Automatica*, 41(2):289–298, 2005. ISSN 0005-1098. doi: <https://doi.org/10.1016/j.automatica.2004.10.006>. URL <https://www.sciencedirect.com/science/article/pii/S0005109804003024>.
- Henrik Lemcke Alfheim, Kjetil Mugerud, Morten Breivik, Edmund Førland Brekke, Egil Eide, and Øystein Engelhardtson. Development of a dynamic positioning system for the revolt model ship. *IFAC-PapersOnLine*, 51(29):116–121, 2018.
- C Maury, G Delhommeau, M Ba, JP Boin, and M Guilbaud. Comparison between numerical computations and experiments for seakeeping on ship models with forward speed. *Journal of ship research*, 47(04):347–364, 2003.
- Icaro Fonseca and Henrique Gaspar. Fundamentals of digital twins applied to a plastic toy boat and a ship scale model. In *34th International ECMS - Conference on Modelling and Simulation - ECMS 2020*, pages 207–213, 06 2020. doi: 10.7148/2020-0207.
- M Zhang, F Tao, B Huang, A Liu, L Wang, N Anwer, and AYC Nee. Digital twin data: methods and key technologies [version 2; peer review: 4 approved]. *Digital Twin*, 1(2), 2022. doi: 10.12688/digitaltwin.17467.2.
- Nur Assani, Petar Matic, and Marko Katalinić. Ship’s digital twin—a review of modelling challenges and applications. *Applied Sciences*, 12:6039, 06 2022. doi: 10.3390/app12126039.
- Muhammad Mazhar Rathore, Syed Shah, Dharendra Shukla, Elmahdi Bentafat, and Spiridon Bakiras. The role of ai, machine learning, and big data in digital twinning: A systematic literature review, challenges, and opportunities. *IEEE Access*, PP:1–1, 02 2021. doi: 10.1109/ACCESS.2021.3060863.
- ISO19030. Ships and marine technology - measurements of change in hull and propeller performance. Standard, International Organization for Standardization, Nov 2016.
- Luca Husemann. Konzeptionierung und entwurf eines modularen schiffsmodells als demonstrator für digitale zwillinge. Number L-006/2022. publisher=CRC Press, 06 2022.
- JS Carlton. 12 - ship resistance and propulsion. In JS Carlton, editor, *Marine Propellers and Propulsion (Second Edition)*, pages 286–318. Butterworth-Heinemann, Oxford, second edition edition, 2007. ISBN 978-0-7506-8150-6. doi: <https://doi.org/10.1016/B978-075068150-6/50014-0>. URL <https://www.sciencedirect.com/science/article/pii/B9780750681506500140>.
- J Holtrop and GGJ Mennen. An approximate power prediction method. *International Shipbuilding Progress*, 29(335):166–170, 1982.
- S M Hasan. Implementation of energy efficiency design index and its impact on the design of oil tanker. 09 2014.
- Adham Bekhit and Constantin Obreja. Numerical and experimental investigation on the freesurface flow and total resistance of the dtmb surface combatant. *IOP Conference Series: Materials Science and Engineering*, 916, 10 2020. doi: 10.1088/1757-899X/916/1/012008.
- E. Bal Beşikçi, O. Arslan, O. Turan, and A.I. Ölçer. An artificial neural network based decision support system for energy efficient ship operations. *Computers and Operations Research*, 66:393–401, 2016. ISSN 0305-0548. doi: <https://doi.org/10.1016/j.cor.2015.04.004>. URL <https://www.sciencedirect.com/science/article/pii/S0305054815000842>.
- MHM-Modellbau.de. FrSky Tandem X20S Fernsteuerung blau (Multi-Protokoll, incl. SD-Karte, Akku, Softcase and Griffschalen), FrSky-X20S-B, a. URL <https://www.>

- mhm-modellbau.de/part-FrSky-X20S-B.php. [Accessed 18-Jul-2023].
- MHM-Modellbau.de. FRISKY-ARCHER-R8 Pro, b. URL <https://www.mhm-modellbau.de/part-FrSky-ARCHER-R8-Pro.php>. [Accessed 18-Jul-2023].
- Zongtong Luo, Xianbo Xiang, and Qin Zhang. Autopilot system of remotely operated vehicle based on ardupilot. In Haibin Yu, Jinguo Liu, Lianqing Liu, Zhaojie Ju, Yuwang Liu, and Dalin Zhou, editors, *Intelligent Robotics and Applications*, pages 206–217, Cham, 2019. Springer International Publishing. ISBN 978-3-030-27535-8.
- ArduPilot.org. ArduPilot — ardupilot.org. <https://ardupilot.org/>, 2023. [Accessed 16-Jul-2023].
- PIXHawk.org. Homepage - PIXHawk, 6 2023. URL <https://pixhawk.org/>.
- Matt Richardson and Shawn Wallace. *Getting started with raspberry PI*. " O'Reilly Media, Inc.", 2012.
- RaspberryPi.com. Homepage - Raspberry Pi, 2023. URL <https://www.raspberrypi.com/>.
- MHM-Modellbau.de. Krick Messingruder 67x45mm Rohr und Ruderhebel, KR-65025, c. URL <https://www.mhm-modellbau.de/part-KR-65025.php>. [Accessed 18-Jul-2023].
- Lloyd's Register. Lloyd's register rules and regulations. Rules, Lloyd's Register, Jan 2023.
- MHM-Modellbau.de. Torcster Torcster Mini Servo NR-85 MG Digital 20G V2, TOR-210674, d. URL <https://www.mhm-modellbau.de/part-TOR-210674.php>. [Accessed 18-Jul-2023].
- Andrew Gong, Rens Macneill, and Dries Verstraete. Performance testing and modeling of a brushless dc motor, electronic speed controller and propeller for a small uav application. In *2018 Joint Propulsion Conference*, 07 2018. doi: 10.2514/6.2018-4584.
- Padmaraja Yedamale. Brushless dc (bldc) motor fundamentals. *Microchip Technology Inc*, 20(1):3–15, 2003.
- P Millet. Brushless vs brushed dc motors: When and why to choose one over the other. *MPS*, 2022.
- Faulhaber.com. Faulhaber.com. URL <https://www.faulhaber.com/en/drive-calculator/fdc/showDetail/324490/593/>. [Accessed 18-Jul-2023].
- MHM-Modellbau.de. Krick MAX Marine P359 350KV, KR-42433, e. URL <https://www.mhm-modellbau.de/part-KR-42433.php>. [Accessed 18-Jul-2023].
- William C. Follmer. Electronic speed control. In *1974 Automotive Engineering Congress and Exposition*. SAE International, feb 1974. doi: <https://doi.org/10.4271/740022>. URL <https://doi.org/10.4271/740022>.
- Andrew Gong and Dries Verstraete. Experimental testing of electronic speed controllers for uavs. In *53rd AIAA/SAE/ASEE Joint Propulsion Conference*, 07 2017. doi: 10.2514/6.2017-4955.
- Faulhaber.com. Series SC 5008 S. URL <https://www.faulhaber.com/en/products/series/sc-5008-s/>. [Accessed 18-Jul-2023].
- MHM-Modellbau.de. HobbyWing EZRuN MAX10 G2, 140A, Brushless-Regler Sensorless, 2-4S LIPO, BCE 5A, HW30102603, f. URL <https://www.mhm-modellbau.de/part-HW30102603.php>. [Accessed 18-Jul-2023].
- Ninad Mehendale. Investigating the battery life issues in unmanned aerial vehicles: An analysis of challenges and proposed solutions. 2021.
- MHM-Modellbau.de. SLS X-Cube 5000mAH 4S1P 14,8V 30C/60C, SLSCUX50004130, g. URL <https://www.mhm-modellbau.de/part-SLSCUX50004130.php>. [Accessed 18-Jul-2023].
- Joseph LaDou. Printed circuit board industry. *International journal of hygiene and environmental health*, 209(3):211–219, 2006.

- Mark I Montrose et al. *Printed circuit board design techniques for EMC compliance*, volume 1. IEEE press Piscataway, NJ, 1996.
- Futek.com. Non-Contact Hex-Drive Rotary Torque Sensor with Encoder TRH605 : FSH02037, a. URL <https://www.futek.com/store/torque-sensors/hex-drive-torque-sensors/non-contact-hex-drive-rotary-encoder-TRH605/FSH02037>. [Accessed 18-Jul-2023].
- Conrad.de. Joy-it SEN-Pressure02 Sensor, a. URL <https://tinyurl.com/3t8cctv9>. [Accessed 18-Jul-2023].
- Amazon.de. Generator, permanent magnetic generator, electric 3-phase ac generator, avan-300 w industrial supply generator (with rectifier 12 v). URL <https://tinyurl.com/b9d9zapd>. [Accessed 18-Jul-2023].
- MHM-Modellbau.de. O.S. Engines O.S. Max-12TG-X 12E Pull-Start*, OS11383002, h. URL <https://www.mhm-modellbau.de/part-OS11383002.php>. [Accessed 18-Jul-2023].
- OMC-Stepperonline.com. NEMA 17 Stepper Motor L=39mm Gear Ratio 10:1 High Precision Planetary Gearbox - 17HS15-1684S-HG10|STEPPERONLINE. URL <https://tinyurl.com/52xb6jbb>. [Accessed 18-Jul-2023].
- NitroRCS.com. Electric Starter for 1/10th and 1/8th Exceed-RC Nitro RC cars. URL <https://www.nitrorcx.com/electric-starter-for-nitro-engines-rc-car.html>.
- ErcMarket.com. Cnc electric fuel pump for nitro or gas fuel rc planes cars boats. URL <https://www.ercmarket.com/cnc-electric-fuel-pump-for-nitro-or-gas-fuel-rc-planes-cars-boats/>. [Accessed 18-Jul-2023].
- Conrad.de. aerobatic tank 500 ml, b. URL <https://www.conrad.de/de/p/reely-1463931-kunstflugtank-500-ml-1463931.html>. [Accessed 18-Jul-2023].
- Conrad.de. Jeti MFlow2-T800, c. URL <https://www.conrad.de/de/p/jeti-mflow2-t800-turbine-durchfluss-telemetriesensor-1546919.html>. [Accessed 18-Jul-2023].
- Digikey.de. SLI-1000 LIQUID FLOW METER. URL <https://www.digikey.de/de/products/detail/sensirion-ag/SLI-1000-LIQUID-FLOW-METER/11568841>. [Accessed 18-Jul-2023].
- HobbyQueenItalia.com. FrSky FGS-01 Telemetry Fuel Gauge Sensor. URL <http://www.hobbyqueenitalia.com/prodotti/frsky-fgs-01-telemetry-fuel-gauge-sensor-144803.aspx>. [Accessed 18-Jul-2023].
- Futek.com. Non-Contact Hex-Drive Rotary Torque Sensor with Encoder TRH605 : FSH02038, b. URL <https://www.futek.com/store/torque-sensors/hex-drive-torque-sensors/non-contact-hex-drive-rotary-encoder-TRH605/FSH02038>. [Accessed 18-Jul-2023].
- Hoang Phuong Nguyen, Anh Tuan Hoang, Sandro Nizetic, Xuan Phuong Nguyen, Anh Tuan Le, Cong Nho Luong, Van Dat Chu, and Van Viet Pham. The electric propulsion system as a green solution for management strategy of co2 emission in ocean shipping: A comprehensive review. *International Transactions on Electrical Energy Systems*, 31(11), 2021. doi: 10.1002/2050-7038.12580. URL <https://www.scopus.com/inward/record.uri?eid=2-s2.0-85090008868&doi=10.1002%2f2050-7038.12580&partnerID=40&md5=c2cbefcbbecdc446725132613c5b1632>. All Open Access, Bronze Open Access.
- Truong MN Bui, Truong Q Dinh, James Marco, and Chris Watts. An energy management strategy for dc hybrid electric propulsion system of marine vessels. In *2018 5th International Conference on Control, Decision and Information Technologies (CoDIT)*, pages 80–85.

- IEEE, 2018.
- Wisam Jabary, Florian Sprenger, Lutz Kleinsorge, Hauke Baumfalk, Simon Mewes, Jens Neugebauer, Changqing Jiang, and Ould el Moctar. Development of a unified data model to improve ship operational performance analyses. 06 2022.
- Byeong Soo Kim and Tag Gon Kim. Cooperation between data modeling and simulation modeling for performance analysis of hadoop. *2017 International Symposium on Performance Evaluation of Computer and Telecommunication Systems (SPECTS)*, pages 1–7, 2017.
- Peter Pin-Shan Chen. The entity-relationship model—toward a unified view of data. *ACM transactions on database systems (TODS)*, 1(1):9–36, 1976.
- DMA. Digital Twins for Blue Denmark, 2018.
- Wisam Jabary, Chien Liu, Florian Sprenger, Lutz Kleinsorge, Hauke Baumfalk, Maximilian Kaster, Simon Mewes, Jens Neugebauer, and Ould el Moctar. Development of machine learning approaches to enhance ship operational performance evaluation based on an integrated data model. 06 2023b.
- Iso 19030-1:2016. <https://www.iso.org/standard/63774.html>, sep 11 2017.
- R. Bellman and R. Kalaba. On adaptive control processes. *IRE Transactions on Automatic Control*, 4(2):1–9, 1959. doi: 10.1109/TAC.1959.1104847.
- C. Myers, L. Rabiner, and A. Rosenberg. Performance tradeoffs in dynamic time warping algorithms for isolated word recognition. *IEEE Transactions on Acoustics, Speech, and Signal Processing*, 28(6):623–635, 1980. doi: 10.1109/TASSP.1980.1163491.
- C.C. Tappert, C.Y. Suen, and T. Wakahara. The state of the art in online handwriting recognition. *IEEE Transactions on Pattern Analysis and Machine Intelligence*, 12(8):787–808, 1990. doi: 10.1109/34.57669.
- Meinard Müller. Dynamic time warping. *Information retrieval for music and motion*, pages 69–84, 2007.
- Pavel Senin. Dynamic time warping algorithm review. *Information and Computer Science Department University of Hawaii at Manoa Honolulu, USA*, 855(1-23):40, 2008a.
- Paul Bourke. Cross correlation. *Cross Correlation”, Auto Correlation—2D Pattern Identification*, 1996.
- Ícaro Aragão Fonseca and Henrique Murilo Gaspar. Challenges when creating a cohesive digital twin ship: a data modelling perspective. *Ship Technology Research*, 68(2):70–83, 2021. doi: 10.1080/09377255.2020.1815140. URL <https://doi.org/10.1080/09377255.2020.1815140>.
- Cátia Salgado, Carlos Azevedo, Hugo Manuel Proença, and Susana Vieira. *Noise Versus Outliers*, pages 163–183. 09 2016. ISBN 978-3-319-43740-8. doi: 10.1007/978-3-319-43742-2_14.
- Yuehua Liu, Tharam Dillon, Wenjin Yu, Wenny Rahayu, and Fahed Mostafa. Noise removal in the presence of significant anomalies for industrial iot sensor data in manufacturing. *IEEE Internet of Things Journal*, 7(8):7084–7096, 2020. doi: 10.1109/JIOT.2020.2981476.
- Gregory F Welch. Kalman filter. *Computer Vision: A Reference Guide*, pages 1–3, 2020.
- Zhongke Jiao, Bo Liu, Enhai Liu, and Yongjian Yue. Low-pass parabolic fft filter for airborne and satellite lidar signal processing. *Sensors*, 15(10):26085–26095, 2015.
- Victoria Hodge and Jim Austin. A survey of outlier detection methodologies. *Artificial intelligence review*, 22:85–126, 2004.
- Evan Abdulmajeed Hasan. A method for detection of outliers in time series data. *International Journal of Chemistry, Mathematics and Physics*, 2019.

- Anuroop Gaddam, Tim Wilkin, Maia Angelova, and Jyotheesh Gaddam. Detecting sensor faults, anomalies and outliers in the internet of things: A survey on the challenges and solutions. *Electronics*, 2020.
- Senthamarai Kaliyaperumal and Manoj Kuppusamy. Outlier detection in multivariate data. *Applied Mathematical Sciences*, 9:2317–2324, 01 2015. doi: 10.12988/ams.2015.53213.
- D Williamson, RA Parker, and Juliette Kendrick. The box plot: A simple visual method to interpret data. *Annals of internal medicine*, 110:916–21, 07 1989. doi: 10.1059/0003-4819-110-11-916.
- Christopher I. Lang, Fan-Keng Sun, Bruce Lawler, Jack Dillon, Ash Al Dujaili, John Ruth, Peter Cardillo, Perry Alfred, Alan Bowers, Adrian McKiernan, and Duane S. Boning. One class process anomaly detection using kernel density estimation methods. *IEEE Transactions on Semiconductor Manufacturing*, 35:457–469, 2022.
- Lily Lin and Paul D Sherman. Cleaning data the chauvenet way. *The Proceedings of the SouthEast SAS Users Group, SESUG Proceedings, Paper SA11*, pages 1–11, 2007.
- Abdulmalik Shehu Yaro, Filip Maly, and Pavel Prazák. Outlier detection in time-series receive signal strength observation using z-score method with sn scale estimator for indoor localization. *Applied Sciences*, 2023. URL <https://api.semanticscholar.org/CorpusID:257649414>.
- Outlier cleaning and sensor data aggregation using modified z-score technique. 2014. URL <https://api.semanticscholar.org/CorpusID:7701827>.
- Boris Iglewicz and David C Hoaglin. *Volume 16: how to detect and handle outliers*. Quality Press, 1993.
- Ane Blázquez-García, Angel Conde, Usue Mori, and Jose Lozano. A review on outlier/anomaly detection in time series data. *ACM Computing Surveys*, 54:1–33, 04 2021. doi: 10.1145/3444690.
- Shivam Agarwal. Data mining: Data mining concepts and techniques. In *2013 international conference on machine intelligence and research advancement*, pages 203–207. IEEE, 2013.
- Anil Jadhav, Dhanya Pramod, and Krishnan Ramanathan. Comparison of performance of data imputation methods for numeric dataset. *Applied Artificial Intelligence*, 33(10): 913–933, 2019. doi: 10.1080/08839514.2019.1637138. URL <https://doi.org/10.1080/08839514.2019.1637138>.
- Quinten A. W. Raaijmakers. Effectiveness of different missing data treatments in surveys with likert-type data: Introducing the relative mean substitution approach. *Educational and Psychological Measurement*, 59(5):725–748, 1999. doi: 10.1177/0013164499595001. URL <https://doi.org/10.1177/0013164499595001>.
- Sveinn Steinarrsson. Downsampling time series for visual representation. 2013. URL <https://api.semanticscholar.org/CorpusID:118276398>.
- Jeroen Donckt, Jonas Donckt, and Sofie Hoecke. tsdownsample: high-performance time series downsampling for scalable visualization. 07 2023.
- Philip Sedgwick. Pearson’s correlation coefficient. *Bmj*, 345, 2012.
- Philip Sedgwick. Spearman’s rank correlation coefficient. *Bmj*, 349, 2014.
- Richard A Davis, Muneya Matsui, Thomas Mikosch, and Phyllis Wan. Applications of distance correlation to time series. 2018.
- Mudambi Ananthasayanam. *A Reference Recursive Recipe for Tuning the Statistics of the Kalman Filter*. 02 2018. ISBN 978-953-51-3827-3. doi: 10.5772/intechopen.71961.
- Seng Hansun. A new approach of moving average method in time series analysis. In *2013 conference on new media studies (CoNMedia)*, pages 1–4. IEEE, 2013.

- Belyaev Alexander, Tutov Ivan, and Butuzov Denis. Analysis of noisy signal restoration quality with exponential moving average filter. pages 1–4, 05 2016. doi: 10.1109/SIBCON.2016.7491750.
- Michael Grieves. Digital twin: Manufacturing excellence through virtual factory replication. 03 2015.
- Michael Grieves. Origins of the digital twin concept. 08 2016. doi: 10.13140/RG.2.2.26367.61609.
- Dmytro Adamenko, Steffen Kunnen, and Arun Nagarajah. *Digital Twin and Product Lifecycle Management: What Is the Difference?*, pages 150–162. 11 2020. ISBN 978-3-030-62806-2. doi: 10.1007/978-3-030-62807-9_13.
- Stefan Boschert and R. Rosen. *Digital Twin—The Simulation Aspect*, pages 59–74. 06 2016. ISBN 978-3-319-32154-7. doi: 10.1007/978-3-319-32156-1_5.
- Mike Shafto, Mike Conroy, Rich Doyle, Ed Glaessgen, Chris Kemp, Jacqueline LeMoigne, and Lui Wang. Modeling, simulation, information technology & processing roadmap. *National Aeronautics and Space Administration*, 32(2012):1–38, 2012.
- Michael Grieves. Digital twin: manufacturing excellence through virtual factory replication. *White paper*, 1(2014):1–7, 2014.
- TH Stachowski and H Kjeilen. Holistic ship design—how to utilise a digital twin in concept design through basic and detailed design. In *Proceedings of the International Conference on Computer Applications in Shipbuilding*, 2017.
- Recommended procedure for inclining test. International maritime organization, 2023.
- C.B. Barrass and D.R. Derrett. Chapter 39 - inclining experiment (stability test) plus fluctuations in a ship’s lightweight. In C.B. Barrass and D.R. Derrett, editors, *Ship Stability for Masters and Mates (Seventh Edition)*, pages 337–343. Butterworth-Heinemann, Oxford, seventh edition edition, 2012. ISBN 978-0-08-097093-6. doi: <https://doi.org/10.1016/B978-0-08-097093-6.00039-6>. URL <https://www.sciencedirect.com/science/article/pii/B9780080970936000396>.
- Kristin Potter, Hans Hagen, Andreas Kerren, and Peter Dannenmann. Methods for presenting statistical information: The box plot. In *VLUDS*, pages 97–106, 2006.
- Pavel Senin. Dynamic time warping algorithm review. *Information and Computer Science Department University of Hawaii at Manoa Honolulu, USA*, 855(1-23):40, 2008b.
- Andrew Rutherford. Applied multiple regression/correlation analysis for the behavioral sciences. *British Journal of Mathematical & Statistical Psychology*, 56:185, 2003.
- Robert Pfannenschmidt Lars Greitsch, Tom Goedicke. Numerical towing tank versus noon data – powering predictions using ranse cfd. In *1st Hull Performance ’&’ Insight Conference(HullPIC’16)*, pages 145–151, 2016.
- Dynamic Time Warping*, pages 69–84. Springer Berlin Heidelberg, Berlin, Heidelberg, 2007. ISBN 978-3-540-74048-3. doi: 10.1007/978-3-540-74048-3_4. URL https://doi.org/10.1007/978-3-540-74048-3_4.
- Georg Steinbuss and Klemens Böhm. Generating artificial outliers in the absence of genuine ones — a survey. *ACM Transactions on Knowledge Discovery from Data*, 15:1–37, 03 2021. doi: 10.1145/3447822.
- O. Sénéchal. Performance indicators nomenclatures for decision making in sustainable conditions based maintenance. *IFAC-PapersOnLine*, 51(11):1137–1142, 2018. ISSN 2405-8963. doi: <https://doi.org/10.1016/j.ifacol.2018.08.438>. URL <https://www.sciencedirect.com/science/article/pii/S2405896318315659>. 16th IFAC Symposium on Information Control Problems in Manufacturing INCOM 2018.
- Anthony F Molland, Stephen R Turnock, and Dominic A Hudson. *Ship resistance and*

- propulsion*. Cambridge university press, 2017.
- ITTC. Ittc – recommended procedures and guidelines. 2017.

This page intentionally left blank.

A

Inclining test procedure

A.1 Theory and mathematical formulation

The purpose of the inclining experiment is to determine the location of the vertical center of gravity (VCG/KG) for a vessel. This is done by applying an external moment to heel the ship. Therefore, the ship hull will naturally produce a moment (righting moment) which equal to the externally applied moment but in the opposite direction. The external moment is applied by moving a known weight transversally with a defined distance Barrass and Derrett (2012). This can be expressed mathematically by Equation (A.1) and illustrated in Figure A.1

$$w \times d = \Delta \times GM \times \tan \theta \quad (\text{A.1})$$

Where :

w is the moved weight, in kg

h is moved distance, in cm

Δ is the ship displacement, in kg

GM is the vertical distance from the CG and metacentric height, in kg

θ is the ship inclined angle, in degrees

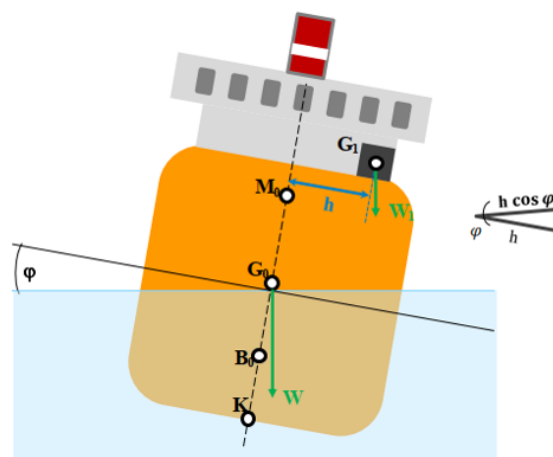


Figure A.1: Ship inclined by weight

In Equation (A.1), the only unknown is the GM value. The ship displacement (Δ) is known

from the ship hydrostatics table, the inclining weights and moved distances are predefined, and the inclination angle is measured experimentally.

Following IMO recommended procedure for inclining test IMO (2023), this experiment is conducted by shifting four weights transversely eight times and finding the final GM by averaging the results.

After obtaining the value of GM, the KG is calculated by Equation (A.2).

$$KG = KB + BM - GM \quad (\text{A.2})$$

where KB and BM are easily obtainable values through the ship hydrostatics table.

In the following sections, the detailed inclining experiment procedures and calculations are described.

A.2 General information

Table A.1: Inclining test General information

Place	DLR Institute of Maritime Energy Systems, Geesthacht
Date	Wednesday, 10 May 2023
Weather	No external effects, indoor condition
Model condition	Bare hull, as manufactured with extra known weights

A.3 Weights layout

before starting the experiment, two additional weights of 10 kg were placed inside the model to increase the model draft since the model bow was out of water under the effect of the bare hull weight only. Also, these weights were placed in a way to achieve zero trim during the experiment. The weights distribution inside the hull is demonstrated in

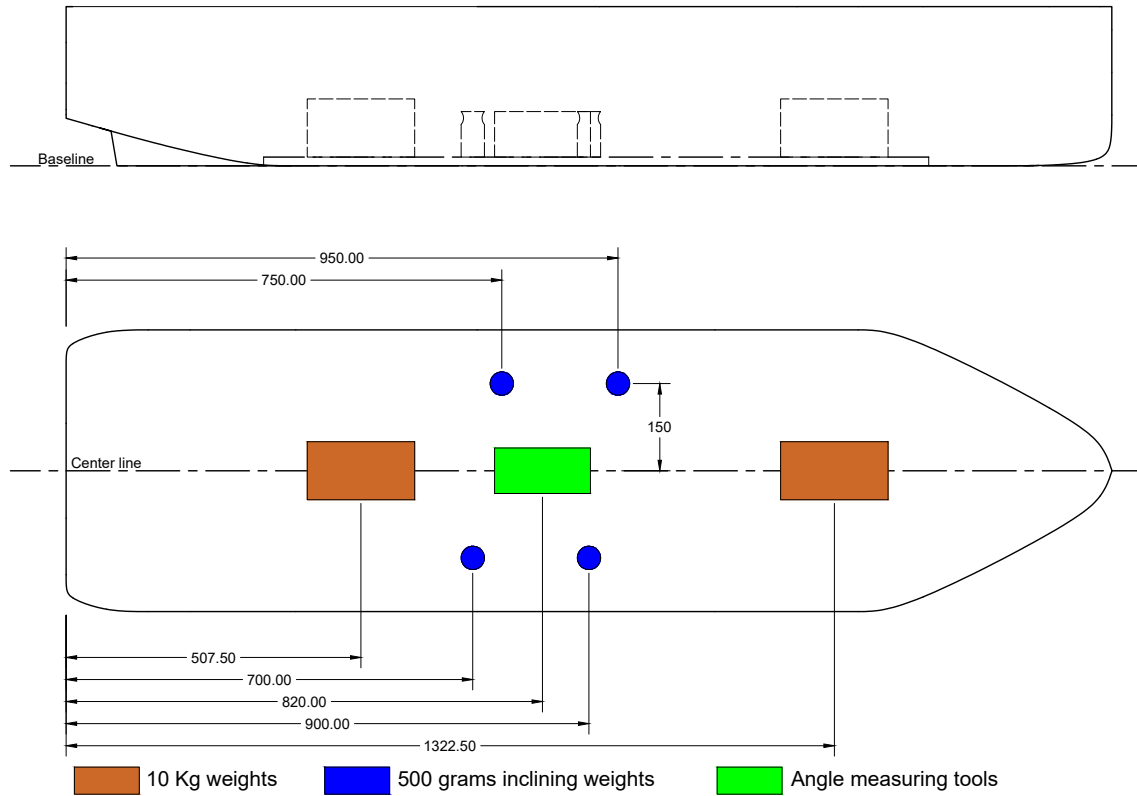


Figure A.2: Solid weights layout during the inclining experiment

The detailed weight items are listed in Table A.2.

Table A.2: Weight breakdown during the inclining experiment

Item	Weight, in kg
Bare hull	10.68
Inclining weight 1	0.5
Inclining weight 2	0.5
Inclining weight 3	0.5
Inclining weight 4	0.5
Measurement tools	0.395
Additional weight 01	10
Additional weight 02	10
Total	33.075

A.4 Weights Shift Procedure

The experiment was conducted using four weights of 500 grams each. The weights were shifted from port to starboard side eight times and the inclining angle was measured for each shift. Figure A.3, Figure A.4, and Figure A.5 are illustrating the weights shifts for each step.

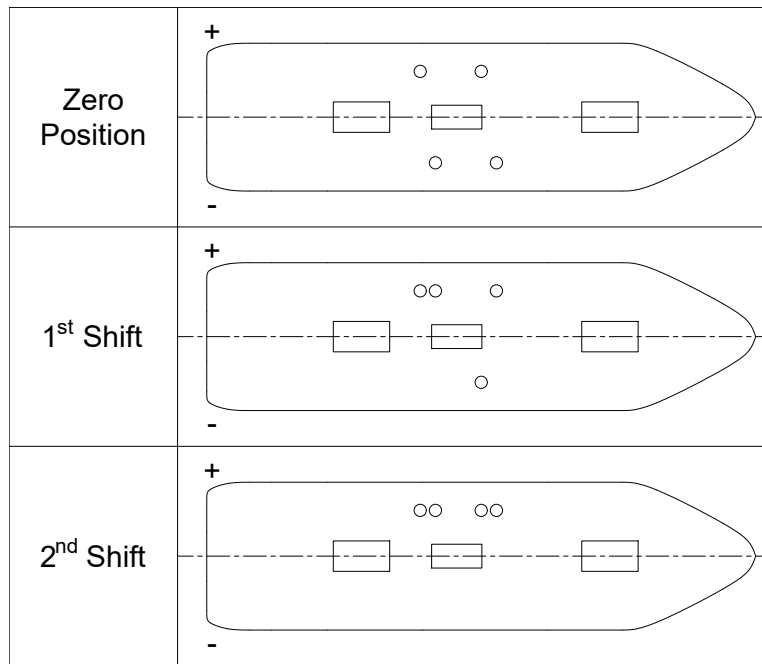


Figure A.3: Weight shift 0 to 2nd

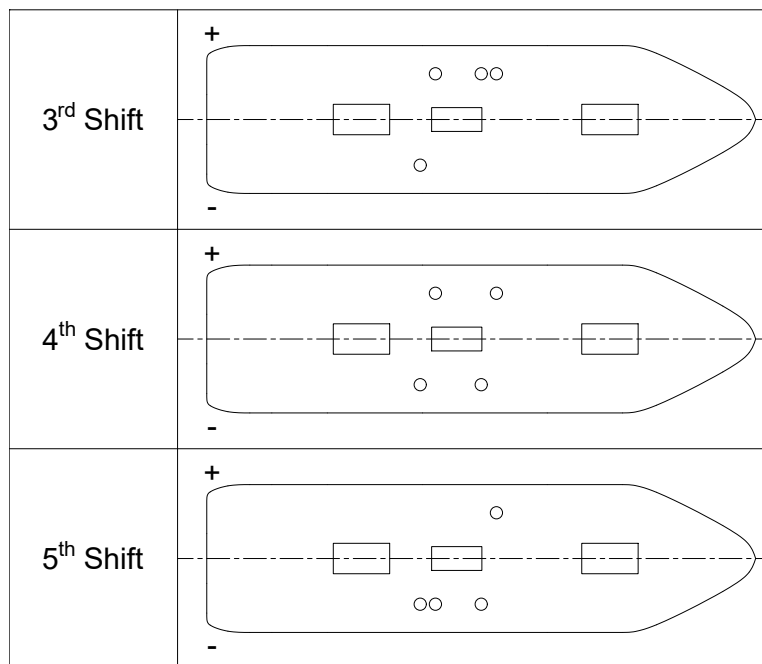


Figure A.4: Weight shift 3rd to 5th

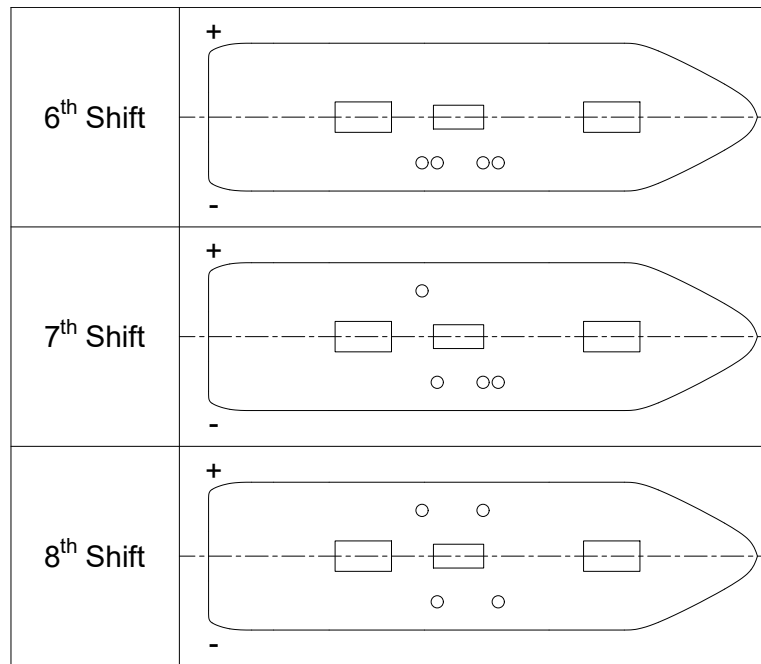


Figure A.5: Weight shift 6th to 8th

A.5 Measured draft

Table A.3 shows the measured drafts of the model during the experiment including all inclining weights, measuring tools, and additional weight.

Table A.3: Measured drafts

	Part	Starboard
Draft aft	6.1	6.1
Draft Fore	6.1	6.1

A.6 Angle measurement

The angle measurement was done by using calibrated a battery-powered flight controller placed inside the model and the measurement values were transmitted via a telemetry model to a computer. This transmission was done via a wireless connection, which allows the model to heel freely with no wires connected.

A.7 Weight shifts and heeling angle reading

Table A.4 showing the angle reading for each weight shift.

Table A.4: Inclining experiment weight shifts and angle reading

Shift No.	From	To	Weight moved (w)	Moved distance (d)	Heeling moment M_H	Inclination angle (θ)	GM
		Unit	kg	cm	kg.cm	degree	cm
Shift 1	SB	P	0.5	30	15	0.93	27.938
Shift 2	SB	P	0.5	30	15	0.99	26.244
Shift 3	P	SB	0.5	-30	-15	-0.99	26.244
Shift 4	P	SB	0.5	-30	-15	-0.93	27.938
Shift 5	P	SB	0.5	-30	-15	-1	25.982
Shift 6	P	SB	0.5	-30	-15	-1	25.982
Shift 7	SB	P	0.5	30	15	1	25.982
Shift 8	SB	P	0.5	30	15	1	25.982
Average GM [cm]							26.536

A.8 Calculating CG location

A.8.1 Vertical center of gravity (VCG)

After calculating GM from the previous step, the value of VCG or KG can be calculated directly from Equation (A.2). The values of BM and KB or KM can be obtained from the model hydrostatics table.

Upon obtaining the hydrostatic properties of the provided 3D model at a draft of 6.1 cm, a deviation was observed between the actual model and the 3D model, as the 33.075 kg displacement corresponded to a draft of 6.21 cm in the 3D model, rather than 6.1 cm. It was also found that the corresponding displacement to a 6.1 cm draft for the 3D model is 32.41 kg which means a 2% reduction from the real model for the same draft. Hydrostatics parameters are shown in Table A.5.

This divergence might occur due to deviation between the actual and digital models during the model fabrication process.

It was convenient for the author to use the hydrostatics values (KB, BM, KM, and LCB) corresponding to the 33.075 kg displacement since the displacement was measured by using digital scales which provide highly accurate reading while the draft measurement was done visually.

Therefore, the KG value of the model is inclined can be calculated as follows

$$KG = KB + BM - GM = 3.34 + 29.91 - 26.536 = 6.714\text{cm}$$

A.8.2 Longitudinal center of gravity (LCG)

By definition, the LCG of a floating body is located directly above the longitudinal center of buoyancy. Therefore the LCG for the model as inclined is 86.8 cm from AFT as shown in Table A.5.

Table A.5: Hydrostatics parameters for actual and 3D model

	MAXSURF		Actual model
	6.1 cm draft	Displacement 33.07 kg	
Displacement kg	32.41	33.07	33.07
Volume (displaced) cm^3	32413.89	33082.07	33073.86
Draft at FP cm	6.1	6.21	6.1
Draft at AP cm	6.1	6.21	6.1
Draft at LCF cm	6.1	6.21	6.1
LCB from AP	86.86	86.8	86.8 ^[1]
KB	3.28	3.34	3.34 ^[1]
BM	30.38	29.91	29.91 ^[1]
KM	33.66	33.25	33.25 ^[1]

[1] Values corresponding to 33.075 kg displacement for the 3D model

A.8.3 Transverse center of gravity (TCG)

the seventh column of Table A.4 shows the slight asymmetric behavior of the model heeling under the effect of shifting weight. In a typical scenario, the heeling angles should be symmetric for both sides. However, in this case, it is obvious that the accumulated heeling angle when all four inclining weights were at the port side is 1.92 degrees and 2 degrees when the weights were on the starboard side.

This behavior reflects that the model's Transverse center of gravity (TCG) is slightly shifted towards the starboard side. Using MAXSURF stability module, it was possible to determine this shift by 0.08 cm which - from the author's point of view - is not a significant number and can be ignored in further calculations. However, there is a high possibility to have an asymmetric layout for internal components which will require manual adjustment of some weights to have an even keel condition.

A.8.4 COG location for the model as inclined

the weight and center of gravity (COG) of the model as inclined is summarized in Table A.6

Table A.6: Model weight and COG as inclined

	Displacement	LCG	TCG	VCG
Unit	kg	cm	cm	cm
	33.075	86.8	-0.08	6.714

A.8.5 COG location for the bare hull

The model during the experiment had some additional weights as shown in Table A.2 which require one more calculation step to find the weight and COG of the bare hull as manufactured. This is done by deducting the added weights and their effect on COG as shown in Table A.7.

Table A.7: Bare hull weight and COG

	Weight [kg]	LCG [cm]	TCG [cm]	VCG [cm]
Model as inclined	33.075	86.8	-0.08	6.71
Weight to be deducted				
Inclining weight 1	0.5	70	-15	4.1
Inclining weight 2	0.5	75	15	4.1
Inclining weight 3	0.5	90	-15	4.1
Inclining weight 4	0.5	95	15	4.1
Measurement tools	0.395	82	0	3.5
Additional weight 01	10	50.75	0	6.5
Additional weight 02	10	132.25	0	6.5
Weight to be deducted summation	22.395	90.5	0	6.2
Bare hull Weight and COG	10.68	79.0	-0.2	7.72

B

Model empirical resistance calculation

The model total resistance then is calculated following the following procedure:

1. Calculate the total resistance for the mother ship (R_{TS}) using Holtrop & Mennen method.
2. Calculate the friction resistance of the mother ship (R_{FS}).
3. Calculate the residual resistance of the mother ship ($R_{WS} = R_{TS} - R_{FS}$).
4. Calculate the model residual resistance $R_{WM} = R_{WS}/\lambda^3$.
5. Calculate the model friction resistance R_{FM} .
6. Calculate the model total resistance ($R_{TM} = R_{WM} + R_{FM}$).

According to Carlton (2007), the above-mentioned calculations can be expressed in Equation (B.1).

$$R_{TS} = [R_{TM} - R_{FM}(1 + k)] \lambda^3 \left(\frac{\rho_S}{\rho_M} \right) + R_{FS}(1 + k) \quad (\text{B.1})$$

, and

$$R_{FM} = \frac{1}{2} \rho V_M^2 A_M C_{fM} \quad (\text{B.2})$$

C_f is calculated according to ITTC-1957 frictional correlation line using Equation (B.3)

$$C_f = \frac{0.075}{(\log(Rn) - 2)^2} \quad (\text{B.3})$$

Where,

$$Rn = \frac{VL}{\nu} \quad (\text{B.4})$$

The above-mentioned calculations are done for each speed until the speed of 13 knots for the mother ship. The results are shown in Figure B.1.

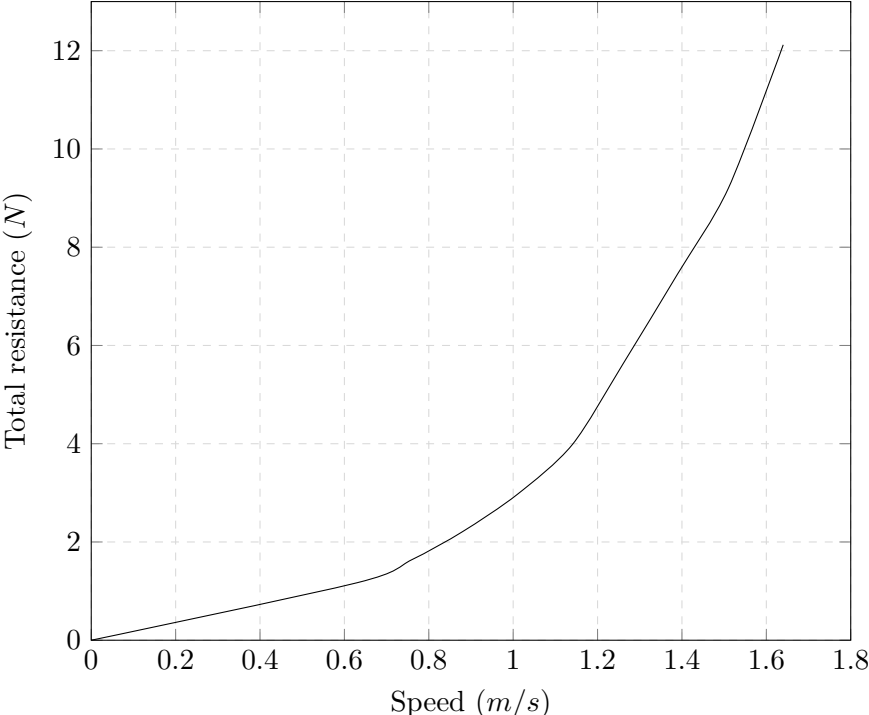


Figure B.1: Ship model speed - total resistance graph according to empirical calculations

Table B.1: Model total resistance calculation

V_S Knot	V_S m/s	V_M m/s	R_{TS} N	R_{ns}	C_{fs}	R_{FS} N	R_{WS} N	R_{WM} N	R_{nM}	C_{fM}	R_{FM} N	R_{TM} N	R_{TM} grams
0.50	0.26	0.06	42.39	5.96E+06	3.29E-03	30.20	12.19	0.00	88063.9	8.65E-03	0.02	0.02	2.14
1.00	0.51	0.13	152.48	1.19E+07	2.91E-03	108.40	44.08	0.01	176127.8	7.12E-03	0.05	0.07	7.05
1.50	0.77	0.19	323.20	1.79E+07	2.72E-03	229.77	93.43	0.02	264191.7	6.41E-03	0.10	0.14	14.30
2.00	1.03	0.25	551.04	2.38E+07	2.59E-03	392.12	158.92	0.03	352255.7	5.96E-03	0.17	0.23	23.67
2.50	1.29	0.32	833.55	2.98E+07	2.50E-03	594.07	239.48	0.05	440319.6	5.65E-03	0.25	0.34	35.05
3.00	1.54	0.38	1168.76	3.58E+07	2.43E-03	834.57	334.19	0.07	528383.5	5.41E-03	0.35	0.47	48.32
3.50	1.80	0.44	1555.05	4.17E+07	2.37E-03	1112.84	442.21	0.10	616447.4	5.22E-03	0.46	0.62	63.42
4.00	2.06	0.50	1993.77	4.77E+07	2.33E-03	1428.23	565.54	0.12	704511.3	5.07E-03	0.58	0.79	80.34
4.50	2.31	0.57	2487.92	5.37E+07	2.28E-03	1780.19	707.73	0.15	792575.2	4.93E-03	0.71	0.97	99.13
5.00	2.57	0.63	3037.07	5.96E+07	2.25E-03	2168.25	868.82	0.19	880639.2	4.82E-03	0.86	1.17	119.75
5.50	2.83	0.69	3647.77	6.56E+07	2.22E-03	2591.99	1055.78	0.23	968703.1	4.72E-03	1.02	1.40	142.32
6.00	3.09	0.76	4333.42	7.15E+07	2.19E-03	3051.06	1282.36	0.28	1056767.0	4.63E-03	1.19	1.64	167.13
6.50	3.34	0.82	5116.72	7.75E+07	2.16E-03	3545.12	1571.60	0.34	1144830.9	4.55E-03	1.37	1.91	194.68
7.00	3.60	0.88	6030.52	8.35E+07	2.14E-03	4073.89	1956.63	0.43	1232894.8	4.48E-03	1.57	2.21	225.66
7.50	3.86	0.95	7124.03	8.94E+07	2.12E-03	4637.09	2486.94	0.54	1320958.7	4.42E-03	1.78	2.56	261.18
8.00	4.12	1.01	8458.69	9.54E+07	2.10E-03	5234.47	3224.22	0.70	1409022.7	4.36E-03	1.99	2.97	302.58
8.50	4.37	1.07	10021.16	1.01E+08	2.08E-03	5865.81	4155.35	0.91	1497086.6	4.30E-03	2.22	3.43	349.55
9.00	4.63	1.14	11967.51	1.07E+08	2.06E-03	6530.89	5436.62	1.19	1585150.5	4.25E-03	2.46	3.98	405.57
9.50	4.89	1.20	14697.13	1.13E+08	2.05E-03	7229.51	7467.62	1.63	1673214.4	4.20E-03	2.71	4.70	479.50
10.00	5.14	1.26	18288.18	1.19E+08	2.03E-03	7961.50	10326.68	2.25	1761278.3	4.16E-03	2.97	5.62	573.07
10.50	5.40	1.33	22087.21	1.25E+08	2.02E-03	8726.68	13360.53	2.92	1849342.2	4.12E-03	3.25	6.59	671.74
11.00	5.66	1.39	25424.86	1.31E+08	2.00E-03	9524.87	15899.99	3.47	1937406.2	4.08E-03	3.53	7.46	760.62
11.50	5.92	1.45	28481.01	1.37E+08	1.99E-03	10355.94	18125.07	3.96	2025470.1	4.04E-03	3.82	8.28	843.70
12.00	6.17	1.51	32025.02	1.43E+08	1.98E-03	11219.73	20805.29	4.54	2113534.0	4.01E-03	4.13	9.20	938.08
12.50	6.43	1.58	36906.26	1.49E+08	1.97E-03	12116.10	24790.16	5.41	2201597.9	3.98E-03	4.44	10.42	1062.66
13.00	6.69	1.64	43947.40	1.55E+08	1.96E-03	13044.92	30902.48	6.74	2289661.8	3.95E-03	4.77	12.12	1235.73

This page intentionally left blank.

C

Towing test

To obtain a more accurate approximation of the hull resistance, a towing test was conducted at the HSVA towing tank.

C.1 Model preparation

The model was loaded with additional solid weights beside the weight of the additional parts needed to conduct the test to reach a draft of 9 cm which corresponds to a 1.5 m draft of the mothership as shown in Figure C.4. The itemized weights of all components included during the experiment are shown in Table C.1.

Table C.1: Towing test model weight breakdown

Item	Weight, in kg
Bare hull	12.16
Additional weight 01	10
Additional weight 02	10
Additional weight 03	5
Additional weight 04	2.5
Cover lid	10.84
Aft holder	1.612
Fore holder	1.616
Total	53.728

The weights were distributed inside the model in such a matter to make the model float in an even keel position with no heel angle.

C.2 Experiment Results

The model was towed with different speeds starting from 0.63 m/s to 1.51 m/s, The first, middle, and last speeds (0.63, 0.88, and 1.51 m/s) were conducted 3 times to spot any potential reading error within the obtained data from drag force sensors. To have a better insight into how the resistance is correlated with the speed, one more additional speed (1.64 m/s) was tested which corresponds to the 13 knots speed of the mother ship.

The model is attached to the cartage in a way that the model is free to trim and to rise/sink vertically during a run is measured.

The procedure of the experiment for each run was as follows:

1. The model is connected to the cartage by a clamp.

2. The cartage start moving with the model dragged into the water.
3. When the cartage reaches a consent speed, the model clap is released leaving the model to sail freely in the water with that speed.
4. The drag force facing the model is recoded by a sensor that is attached to the model bow.
5. Near the end of the run, the model is been clamped again to the cartage.
6. The sensor reading is then displayed on a monitor where it can be reviewed and then the recorded data are saved in .SCV file.

An Example of the obtained graphs for the recorded data during each run is shown in Figure C.2. the three shown graphs are described as follows:

1. The first graph is representing the model drag force/ total resistance.
2. The second graph is showing how much stern force is applied to the model, it is important for this value to converge near zero by the end of the run.
3. The third graph is representing whether the clamp is on or of, in the example shown the clamp was off between a time span of 42 to 88 seconds.

The region where the real model total resistance can be accurately measured is 5 seconds before the clamp closures near the end of the run. In this region, the model is running freely at a constant speed which provides the most accurate resistance reading.

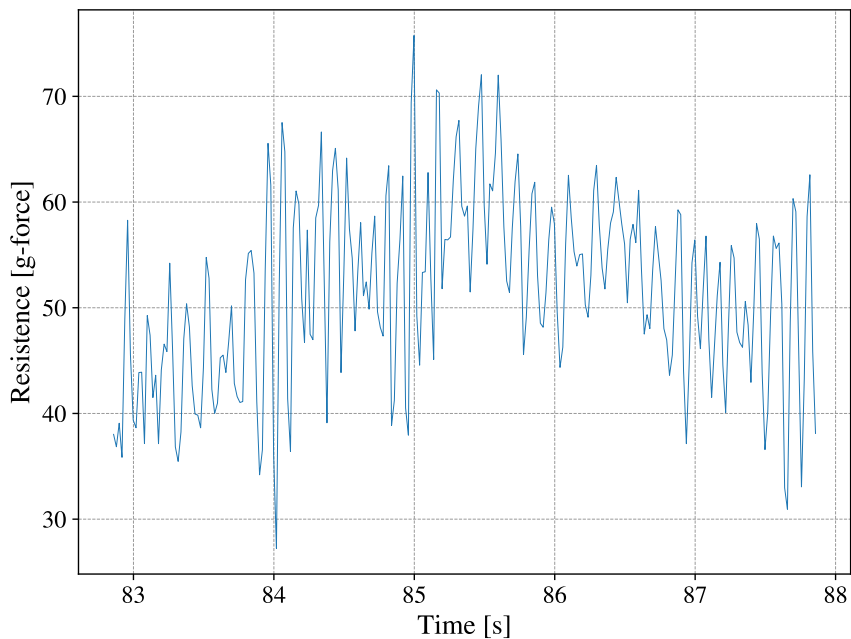


Figure C.1: Measured resistance 5 seconds before clamp closure

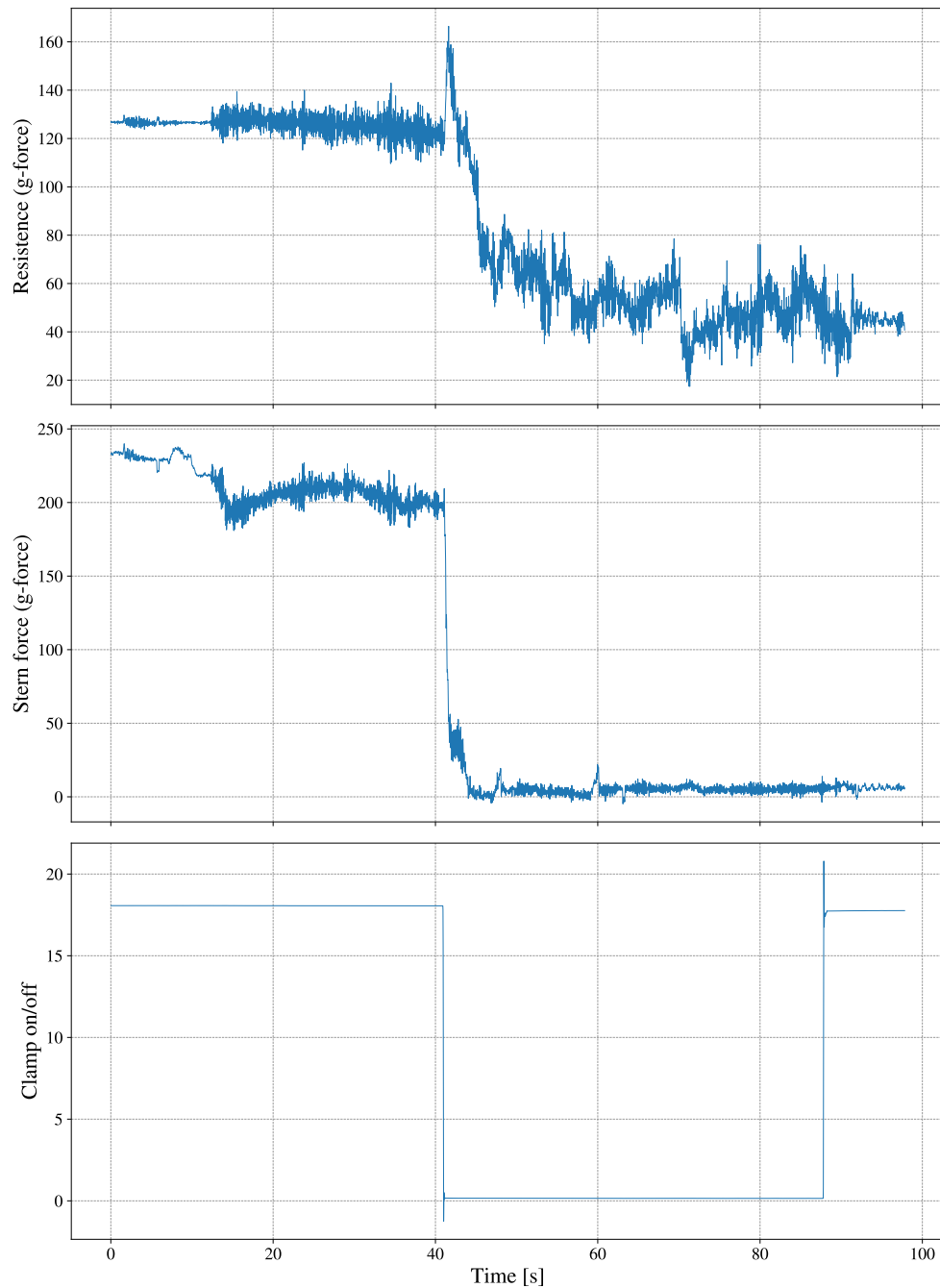


Figure C.2: Recorded data at speed 0.63ms

Figure C.1 shows the resistance measured 5 seconds before the clamp closure, the resistance at 0.63 m/s speed is then obtained by averaging the captured data in that region.

For the sake of accuracy and productivity, a Python code was developed to automatically capture the recorded resistance 5 seconds before the clamp closure and average them.

The mentioned procedure was followed for each speed and The recorded results are shown in Table C.2 and illustrated in Figure C.3.

Table C.2: The recorded model total resistance

V_m , in m/s	R_{TM} , in grams			
	1st run	2nd run	3rd run	Average
0.63	101.56	99.92	99.69	100.39
0.76	160.77			160.77
0.88	225.35	244.02		234.69
1.01	334.72			334.72
1.14	466.50	465.25	474.19	468.65
1.26	627.65			627.65
1.39	847.79			847.79
1.51	1036.90	1079.60	1029.56	1048.68
1.64	1538.23			1538.23

A constant of 50 grams was added to all measured resistance values which represents a pre-applied force on the sensor to keep the connecting wire in tension.

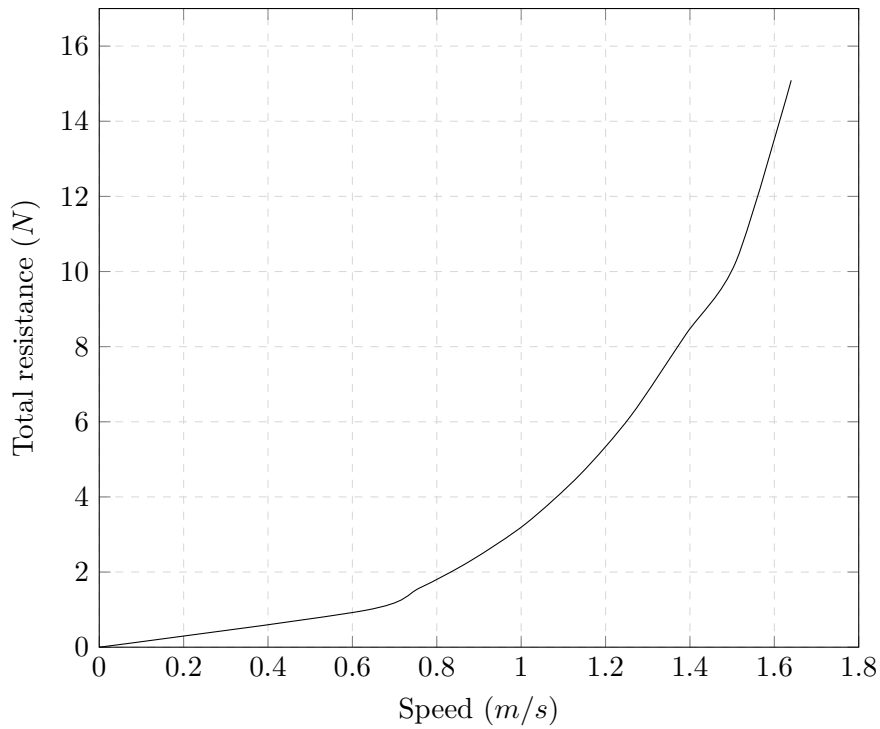
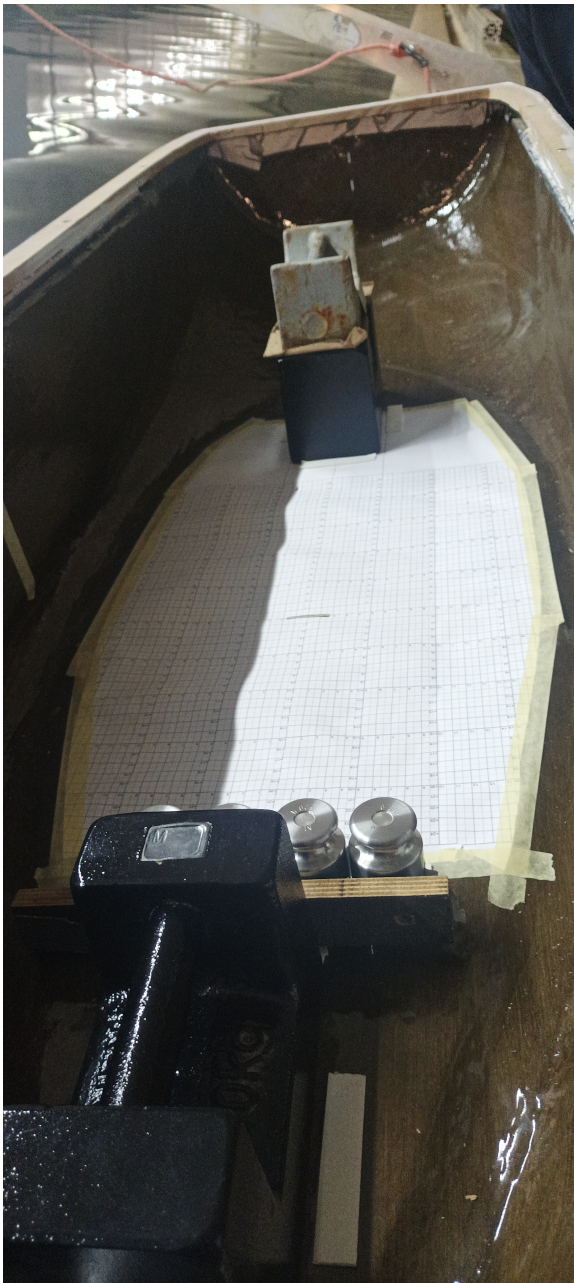


Figure C.3: Ship model speed - total resistance graph according to towing test



(a) Fore to Aft

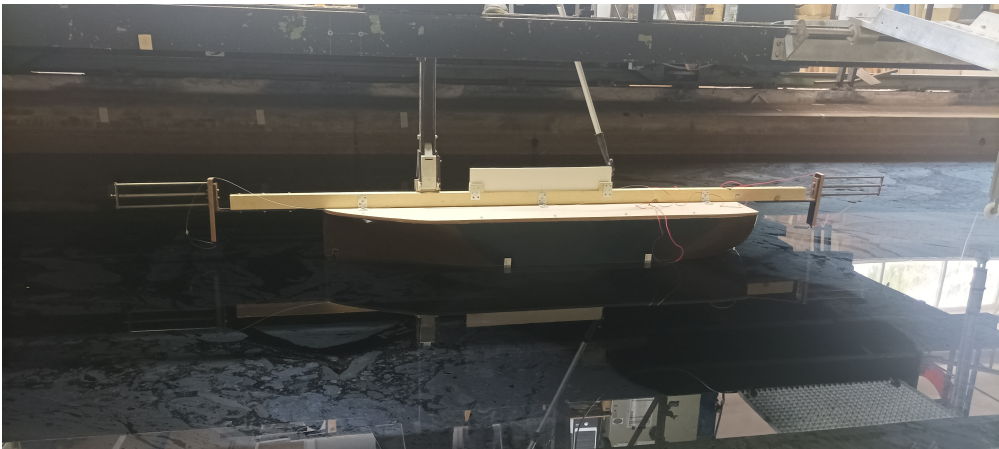


(b) Aft to fore

Figure C.4: Weights arrangement in the model



(a) Prepared Model



(b) The model attached to the towing cartage

Figure C.5: Prepared Model

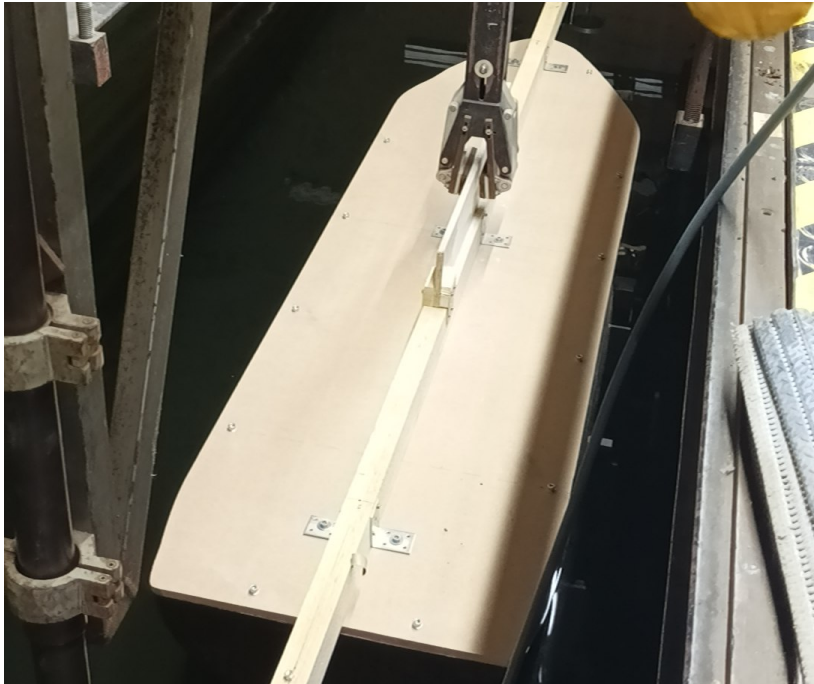


Figure C.6: The model attached to the towing cartage

D

Propulsion Motor Calculations

Referring to the results shown in Table C.2, the effective power was calculated. First calculating the effective power for one propeller corresponding to the model speed of 1.51 m/s. 2% was added to total resistance to compensate for the presence of appendages (Molland et al., 2017).

$$P_E = 0.5 \times R_T \times V_m \quad (D.1)$$

Hence, calculating the required delivered power P_D assuming propeller quasi propulsive efficiency $\eta_D = 0.61$ (Molland et al., 2017).

$$P_D = \frac{P_E}{\eta_D} \quad (D.2)$$

Calculation of the motor brake power P_B assuming that transmission efficiency η_T is about 0.95 (Molland et al., 2017).

$$P_B = \frac{P_D}{\eta_T} \quad (D.3)$$

Calculating the required revolution per second (RPS) is done by assuming that the propeller will operate with a range of coefficient of advance (J) between 0.6 and 1 where high efficiency is expected. Then the RPS is calculated using where (w) was assumed to be 0.15 (Molland et al., 2017).

$$n = \frac{V \times (1 - w)}{J \times D} \quad (D.4)$$

After knowing the required motor power and RPS, the required torque for an electric motor can be calculated based on

$$Torque = \frac{Power}{2 \times \pi \times \frac{RPM}{60}} \quad (D.5)$$

The detailed values are shown in Table D.1

Table D.1: Powering calculation parameters

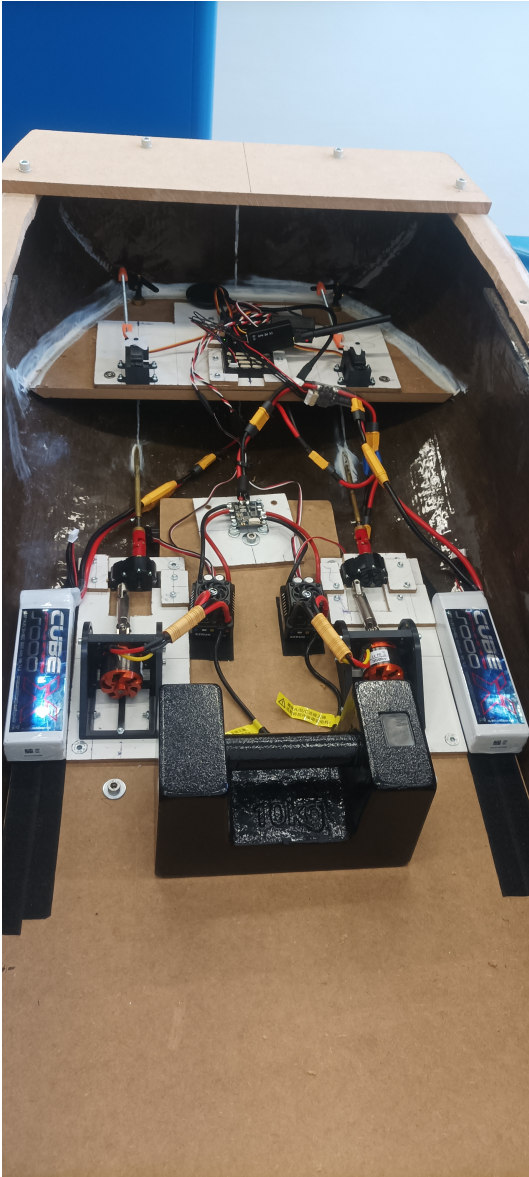
Parameter	Symbol	Value	Unit
Model total resistance	R_{TM}	10.5	N
Model Speed	V_m	1.51	m/s
Effective power per motor	P_E	7.92	Watt
Quasi Propulsive Efficiency	η_D	0.61	
Delivered Power per motor	P_D	12.99	Watt
Transmission Efficiency	η_t	0.90	
Motor output power	P_{out}	14.43	
Motor Efficiency	η	0.85	
Motor input power	P_{in}	16.98	
Advance Coefficient	J	0.6-1	
Wake fraction	w	0.15	
Speed of advance	V_a	1.284	m/s
Revolutions per minute	RPM	1975-1185	RPM
Motor torque		0.111-0.137	N.m

E

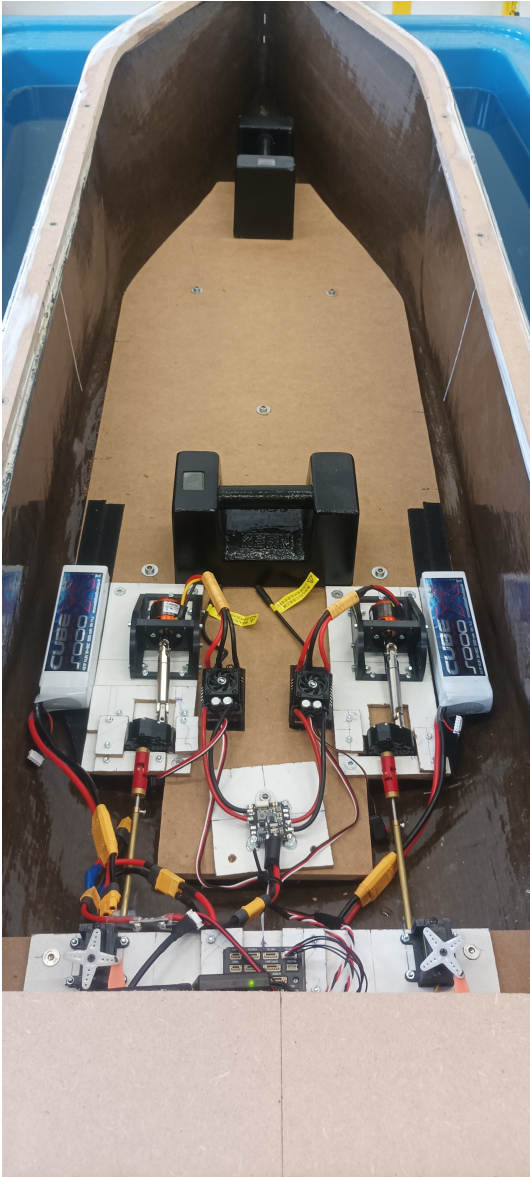
Model Photos



Figure E.1: Model hull



(a) Model internal components 01



(b) Model internal components 02

Figure E.2: Model internal components



(a) Model installed rudder and propeller



(b) Model runs in HSVA

Figure E.3: Prepared Model

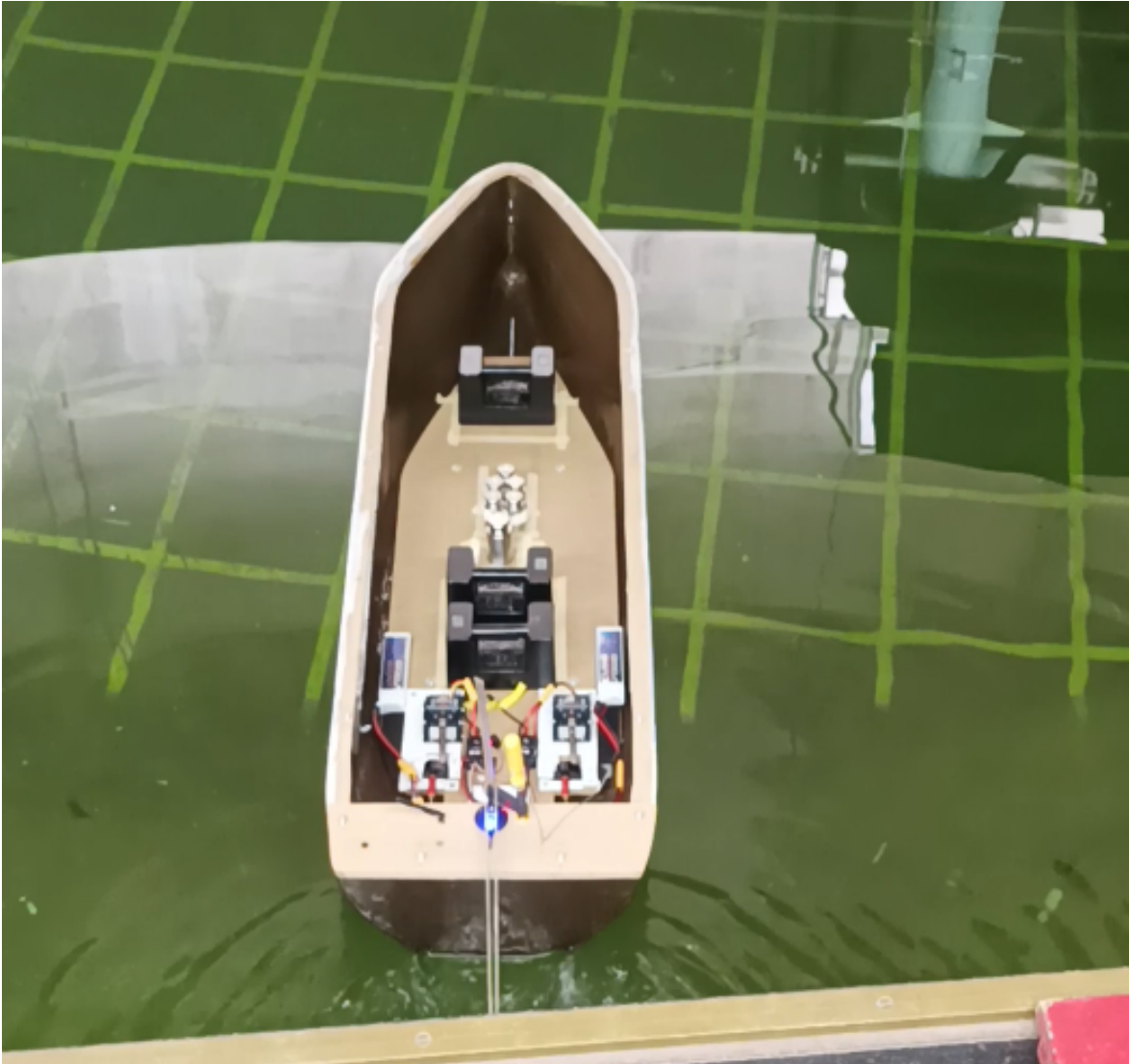


Figure E.4: Model during the bollard pull test

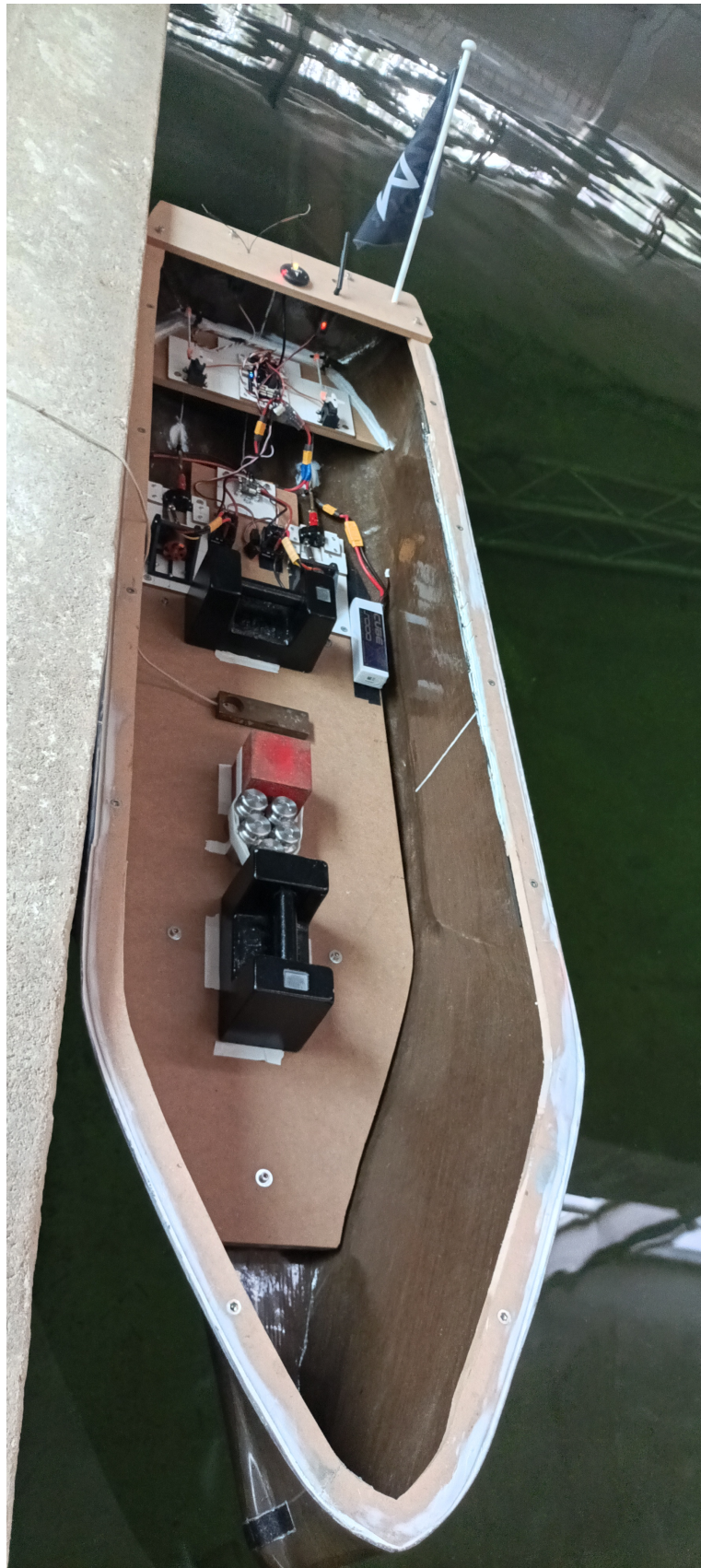


Figure E.5: Prepared model for runs

